EBERHARD KARLS
UNIVERSITÄT
TÜBINGEN

Zentrum für Angewandte Geowissenschaften (ZAG)

TÜBINGER GEOWISSENSCHAFTLICHE ARBEITEN (TGA)

Reihe C: Hydro-, Ingenieur- und Umweltgeologie

Schriftleitung: P. Grathwohl, G. Teutsch

Ralf Brauchler

Characterization of Fractured Porous Media Using Multivariate Statistics and Hydraulic Travel Time Tomography

TGA, C87, 2005

Characterization of Fractured Porous Media Using Multivariate Statistics and Hydraulic Travel Time Tomography

Dissertation

zur Erlangung des Grades eines Doktors der Naturwissenschaften

der Geowissenschaftlichen Fakultät

der Eberhard-Karls-Universität Tübingen

vorgelegt von

Ralf Brauchler

aus Schorndorf

2005

Tag der mündlichen Prüfung: 10.12.2004

Dekan: Prof. Dr. Dr. h.c. Muharrem Satir

1. Berichterstatter: Prof. Dr. Teutsch

2. Berichterstatter: PD Dr. Liedl

Herausgeber: Institut für Geowissenschaften der Universität Tübingen
Sigwartstraße 10, D-72076 Tübingen

Schriftleitung der Reihe C: Zentrum für Angewandte Geowissenschaften (ZAG)
Lehrstuhl für Angewandte Geologie
Prof. Dr. Peter Grathwohl & Prof. Dr. Georg Teutsch

Redaktion: Dipl.-Geol. Björn Sack-Kühner

ISSN 0935-4948 (Print)
ISSN 1610-4706 (Internet)

TGA	Reihe C	Nr. 87	72 S., 52 Abb., 8 Tab., 6 S. Anh.	Tübingen, Februar 2005

Characterization of Fractured Porous Media Using Multivariate Statistics and Hydraulic Travel Time Tomography

by Ralf Brauchler[1]

Abstract: Fractured hard rocks are important in engineering, geotechnical, and hydrogeological practice because they act as hydraulic conductors providing pathways for fluid flow or barriers that prevent flow across them. In this thesis fractured porous media such as sandstones, which show a significant permeability of the matrix, are treated. In comparison to low permeable hard rocks such as granite and gneiss, fractured porous media show significant storage, flow, and transport e.g. of contaminants within the matrix. This has to be taken into account by the evaluation of flow and transport experiments. A fundamental step in understanding and predicting the behavior of fractured porous aquifers involves the identification of the spatial distribution of hydraulically significant features. Therefore, high resolution flow and transport data sets are required. Two different approaches are applied in order to evaluate high resolution flow and transport experiments arranged in a tomographical array.

First, a multivariate statistical approach for the analysis of meso-scale flow and transport experiments is proposed. Within the statistical approach flow and transport measurements are classified into quasi-homogeneous groups in order to determine properties and parameter zonation, which control flow and transport. The methodology was applied to a data set of gas flow and tracer experiments conducted to a gas saturated, fissured sandstone block of $60 \times 60 \times 60$ cm^3 in size. The agreement of the classification results with a geological surface mapping and numerical simulations show that it is possible to characterize and simplify complex systems without losing essential information about the investigated system.

In the second part a travel time based hydraulic tomographic approach is proposed. The approach provides the inversion of travel times of hydraulic or pneumatic tests conducted in a tomographic array. The inversion is based on the relation between the peak time of a recorded transient pressure curve and the diffusivity of the investigated system. The development of a transformation factor enables the inversion of further travel times besides the peak time of a transient curve. As the early travel times of the curve are mainly related to preferential flow features while the inversion based on late travel times reflect an integral behavior, it can be assumed that the different inversion results reflect the properties of the overall system. The method has been applied to data from a set of pneumatic short term tests conducted to a gas saturated fractured sandstone cylinder with a height of 34 cm and a diameter of 31 cm. The three-dimensional reconstructions of the diffusivity distribution are found to be highly reliable and robust. In particular, the mapped fracture of the sandstone cylinder coincides with the reconstructed diffusivity distribution. In order to get a better insight of the hydraulic travel time approach, synthetic data sets are used. The synthetic data sets comprise simulated slug tests conducted in a tomographical array. The main focus of the synthetic study is to appraise the influence of the various travel times on the inversion results in dependence of the permeability distribution of the investigated geological medium. The inversion results are showing a strong dependence on the used travel times. The comparison of the different reconstructions based on different travel times with the forward model allows the verification and appraisal of the quality of the inversion. Hence, it is possible to suggest which travel time is most suited to reconstruct a certain subsurface structure.

---

[1] Dissertation an der Geowissenschaftlichen Fakultät an der Universität Tübingen
Zentrum für Angewandte Geowissenschaften, Angewandte Geologie, Sigwartstr. 10, 72076 Tübingen, Germany

Charakterisierung von geklüftet porösen Medien unter Verwendung von Multivariater Statistik und Hydraulischer Laufzeittomographie

Kurzfassung: Geklüftete Festgesteine sind wichtig im Rahmen der ingenieurtechnischen, geotechnischen und hydrogeologischen Praxis, da sie entweder als hydraulische Leiter agieren und somit bevorzugte Fließpfade für Fluide darstellen oder sie die Eigenschaften von Geringleiter aufweisen und somit hydraulische Barrieren darstellen. In dieser Arbeit werden geklüftet poröse Festgesteine untersucht, die eine signifikante Matrixpermeabilität aufweisen. Im Vergleich zu gering durchlässigen Festgesteinen wie Granit oder Gneis weisen geklüftet poröse Medien bedeutende Speicher-, Strömung- und Transportkapazitäten auf, was sich z.B. auf den Transport von Schadstoffen innerhalb der Matrix auswirkt. Dies muss bei der Auswertung von Strömungs- und Transportexperimenten berücksichtigt werden. Ein grundlegender Schritt zum Verständnis und zur Vorhersage des Verhaltens von geklüftet porösen Aquiferen ist die Identifizierung der räumlichen Verteilung hydraulisch signifikanter Merkmale. Dafür werden hochauflösende Strömungs- und Transportdatensätze benötigt. Zur Auswertung der hochauflösenden Strömungs- und Transportexperimente, die unter Verwendung einer tomographischen Messanordnung aufgezeichnet worden sind, werden zwei unterschiedliche Ansätze verfolgt.

Zuerst wird ein multivariater statistischer Ansatz für die Analyse von Strömungs- und Transportexperimenten vorgestellt. In diesem statistischen Ansatz werden Strömungs- und Transportmessungen in quasi homogene Gruppen eingeteilt, um die Eigenschaften und Parameterzonierung, die Strömung und Transport kontrollieren, zu bestimmen. Mit dieser Methode sind Strömungs- und Transportexperimente ausgewertet worden, die an einem gasgesättigten, geklüfteten Sandsteinblock mit einer Kantenlänge von 60 cm durchgeführt wurden. Die Klassifikationsergebnisse stimmen mit der geologischen Oberflächenkartierung und den numerischen Simulationen überein. Dies zeigt, dass es mit Hilfe des verwendeten Ansatzes möglich ist, komplexe Systeme zu charakterisieren und zu vereinfachen, ohne dass wichtige Systeminformationen verloren gehen.

Im zweiten Teil wird ein auf Laufzeiten basierender Ansatz zur hydraulischen Tomographie vorgestellt. Dieser Ansatz umfasst die Inversion von Laufzeiten hydraulischer oder pneumatischer Tests, die unter Verwendung einer tomographischen Messanordnung aufgezeichnet worden sind. Die Inversion beruht dabei auf dem Zusammenhang zwischen der Laufzeit der maximalen Signaländerung eines aufgezeichneten instationären Signals und der Diffusivität des untersuchten Systems. Die Entwicklung eines Transformationsfaktors ermöglicht die Inversion von weiteren Laufzeiten, neben der Laufzeit der maximalen Änderung eines instationären Signals. Da frühe Laufzeiten einer aufgezeichneten Druckkurve überwiegend bevorzugte Flieswege und spätere Laufzeiten das integrale Verhalten des untersuchten Systems widerspiegeln, kann davon ausgegangen werden, dass die unterschiedlichen Inversionsergebnis das Verhalten des Gesamtsystems repräsentieren. Mit diese Methode wurden Daten von pneumatischen Kurzzeittests ausgewertet. Diese Daten sind an einem gasgesättigten, geklüfteten Sandsteinzylinder mit einer Höhe von 34 cm und einem Durchmesser von 31 cm aufgezeichnet worden. Die Ergebnisse der dreidimensionalen Diffusivitätsrekonstruktionen haben sich als zuverlässig und stabil erwiesen. Insbesondere zeigt die dreidimensionale Rekonstruktion der Diffusivitätsverteilung eine hohe Übereinstimmung mit der Lage der Kluft innerhalb des Zylinders. Um neue Erkenntnisse auf dem Gebiet der hydraulische Laufzeittomographie zu gewinnen, sind synthetische Datensätze verwendet worden. Die synthetischen Datensätze umfassen Slug-Tests, die unter Verwendung einer tomographischen Messanordnung modelliert worden sind. Ziel der synthetischen Fallstudie ist, den Einfluss unterschiedlicher Laufzeiten auf das Inversionsergebnis, in Abhängigkeit von der Permeabilitätsverteilung des untersuchten geologischen Mediums, zu bewerten. Die Inversionsergebnisse zeigen eine deutliche Abhängigkeit von den verwendeten Laufzeiten. Durch einen Vergleich zwischen den Diffusivitätsrekonstruktionen, die auf unterschiedlichen Laufzeiten basieren, und dem verwendeten Vorwärtsmodell ist es möglich, die Qualität der Inversionsergebnisse zu bewerten und zu überprüfen. Somit kann eine Inversionsstrategie vorgeschlagen werden, die für den jeweiligen Untergrund am besten geeignet ist.

Acknowledgements

The investigations presented in this thesis are conducted with the financial support of the German Research Foundation (Deutsche Forschungsgesellschaft) under grant no. Di 833/1 “Hard Rock Aquifer Analogue: Experiment & Modelling”.

I would like to thank my advisors Dr. P. Dietrich, PD Dr. R. Liedl and Prof. Dr. G. Teutsch for their valuable input both in terms of administrative support and academic help. I want to express my profound thanks to them for their guidance, constructive criticisms, suggestions, and for the freedom to work on my own ideas.

I would like to thank my colleagues Dr. S. Birk, D. Chen, Dr. C. Leven, and A. Rein for the fruitful discussions and for reading and commenting the manuscript of this thesis.

For their help in the laboratory I dedicate my thanks to K. Faiß, W. Kürner, M. Licht and F. Sonnenfroh.

Last but not the least, for the organization and academic support, I would like to thank Prof. Dr. M. Everett, Prof. Dr. B. Johnson, and Dr. J.-T. Cheng from the Department of Geology and Geophysics, Texas A&M University, College Station (Texas, USA).

Index

List of Figures

List of Tables

List of Symbols

A_n	[-]	infinite number of functions
a	[-]	component loading
C_j	[-]	conversion factor of the jth travel time
d_{ij}	[L]	distance along trajectory i in voxel j
$D(R;P)$	[-]	distance between the groups R and P
D	[L/T^2]	diffusivity
E	[-]	eigenvalue
$f_{\alpha,d}$	[-]	transformation factor for a Dirac source
$f_{\alpha,h}$	[-]	conversion factor for a Heaviside source
$f\left(\Delta\sqrt{D_j^{-1}}\right)$	[-]	objective function at the derivation of the reconstruction technique
h	[L]	potential in dependence of time and space
h_0	[L]	Aquifer height
H	[L]	potential in dependence of frequency and space
H_0	[L]	Initial head
J	[-]	functional at the derivation of the reconstruction technique
K	[L/T]	hydraulic conductivity
K_a	[L^2]	permeability of aquifer
K_b	[L^2]	permeability of borehole
n_i	[-]	number of rows in matrix X
p	[-]	component
r	[L]	space
r_a	[L]	aquifer radius
r_s	[L]	borehole radius
s	[L]	trajectory
S	[-]	storage
S_s	[1/L]	specific aquifer storage
S_c	[1/L]	specific wellbore storage
$t_j^{reference}$	[T]	jth travel time of the reference model
$t_j^{"true\ storage"}$	[T]	jth travel time of the model influenced by wellbore storage
T	[L/T^2]	transmissivity

T_s	[T]	time step
t_{peak}	[T]	travel time of the peak of a Dirac signal
v	[L/T]	velocity
V	[L^3]	Volume
v_{im}	[-]	row index of the m-th observation in the i-th cluster in matrix X
x_1	[L]	coordinates of the source
x_2	[L]	coordinates of the receiver
X	[-]	$a \times b$ matrix with a observations and b variables
X	[L]	space
$\bar{x}_{i,j}$	[-]	the average of the non-missing observations for variable j in cluster I
z_{kj}	[-]	observed values of each variable j with respect to each experiment k
α	[-]	head ratio
σ	[-]	pseudophase
Δ	[T^2/L]	inverse of diffusivity
φ	[-]	sum of squares within each cluster
ω	[1/T]	frequency
Φ_a	[-]	aquifer porosity

Indices:

$_d$	subscript stands for a Dirac source
$_h$	subscript stands for a Heaviside source
^{m}	with respect to measured travel time
^{e}	with respect to estimated travel time

1 Introduction

1.1 Motivation and Objectives

Hard rocks are covering 75 % of the worlds surface [DIETRICH ET AL., 2005]. Due to this huge spatial distribution fractured hard rocks are important in engineering, geotechnical and hydrogeological practice because they act as hydraulic conductors, providing pathways for fluid flow or barriers that prevent flow across them. For the exploitation of many petroleum, geothermal and water supply reservoirs the pathways for fluid flow are decisive for the economical success. They are also decisive for the stability of engineered structures like tunnels, mines and dams. Additionally, in the last few decades hard rocks have become more and more interesting for storage of high nuclear waste because of their hydraulic properties. In this context it is important to predict potential migration pathways and if they will reenter the surface or near surface environment.

Typically, hard rocks are dominated more by heterogeneity and anisotropy than unconsolidated sediments, thus flow and transport can be expected to be more complex in such aquifer systems. As a consequence, the reliable characterization of hard rocks and the predictions of flow and transport in such rocks are very difficult due to their higher degree of heterogeneity and anisotropy. In particular the high differences in hydraulic conductivity between matrix and fractures are determining the system. This characteristic causes high contrasts in hydraulic conductivity within the system and high spatial parameter variability.

In this thesis, fractured porous media such as sandstones, which show a significant permeability of the matrix, are treated. In comparison to low permeable hard rocks such as granite and gneiss, fractured porous media show significant storage, flow and transport e.g. of contaminants within the matrix. This has to be taken into account by the design and evaluation of flow and transport experiments.

A fundamental step in understanding and predicting the behavior of fractured porous aquifers involves the identification and location of hydraulically significant features. Conventional aquifer test methods such as pumping tests, single-well slug tests and tracer tests are usually not suited to predict the flow and transport in locally restricted fractured porous aquifers dominated by several preferential flow paths. Pumping and tracer tests lead to integral information averaged over large volumes, whereas slug tests lead to more or less local information close to the slugged borehole.

In order to overcome this problem high resolution flow and transport data sets are required, allowing the identification of the spatial distribution of hydraulically significant features. Tomographical measurement techniques are suited to gain such high resolution data sets. The principle of tomography was developed for medical applications, e.g. to determine the spatial distribution of X-ray attenuation over cross sections of the head or body [MERSEREAU & OPPENHEIM, 1974, SCUDDER, 1978]. In Figure

1.1 the principle of tomographic measurements is illustrated. The schematic sketch shows the two dimensional investigation of an area including a rectangular target zone. The position of the target zone is unknown at the beginning of the measurements. The sketch is illustrating that the target can be localized by conducting measurements from different directions.

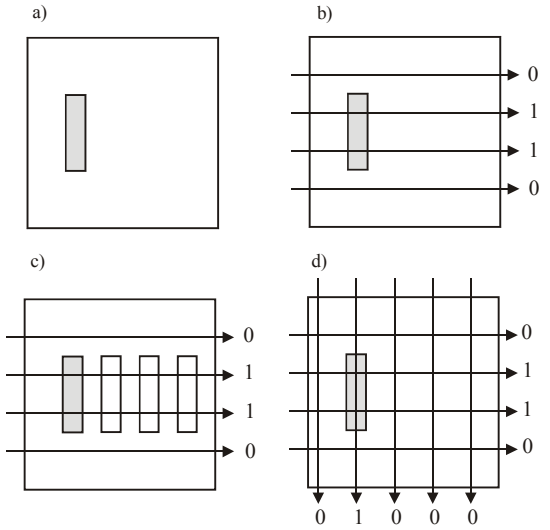

Figure 1.1 Schematic sketch of the tomographic reconstruction. (a) The gray rectangle displays the target zone within a homogenous background. (b) Measurements crossing the target lead to other results (here 1) as measurements crossing the homogenous background (here 0). (c) The conductance of the measurements from left to right enables the determination of the horizontal spatial position of the target. (d) By means of the conductance of a second test series from top to bottom, the exact spatial position of the target can be determined [after FECHNER & MEIER, 1992].

The focus of this thesis is to propose evaluation techniques of high resolution flow and transport experiments arranged in a tomographical array. Thereby two approaches are applied:

1. Multivariate statistical approach:

In the first part a multivariate statistical approach for the analysis of meso-scale flow and transport experiments is proposed. Within this statistical approach, flow and transport measurements are classified into quasi-homogenous groups in order to determine properties and parameter zonation controlling the flow and transport within the investigated system. The methodology was applied to a data set of gas flow and tracer experiments conducted to a gas saturated, fissured sandstone block of 60 $\times$ 60 $\times$ 60 cm^3 in size.

2. Hydraulic travel time tomography

In the second part of the thesis a hydraulic tomographic inversion approach based on travel times of pressure or hydraulic signals is proposed. The aim of this approach is to localize the hydraulically significant features and to determine their hydraulic properties. The approach follows the procedure of seismic ray tomography. As the two techniques are based on the propagation of wave fronts it is possible to use the same inversion technique. The methodology was applied to data conducted in a tomographical array to a gas saturated fractured sandstone cylinder with a height of 34 cm and a diameter of 31 cm.

In order to get a better insight of the hydraulic travel time approach, synthetic data sets are used. The data sets were generated using the Finite Element Heat and Mass Transfer Code (FEHM) from Los Alamos National Laboratory. The data base of the inversion comprises simulated slug tests, in which the position of the sources (injection ports) and the receivers (observation ports) isolated with packers are varied between the tests. The effects of variation of input parameters like wellbore storage and permeability distribution of the investigated system, on the travel time of a pressure pulse and its inversion is investigated. The comparison of the reconstructed tomograms with the forward model allows the verification and appraisal of the quality of the inversion.

1.2 Outline

Chapter 2 comprises the evaluation of a high resolution data set of flow and transport experiments. The experiments are conducted in a tomographical array to a fissured sandstone block of 60 × 60 × 60 cm^3 in size. The evaluation is based on the combination of different multivariate statistical methods, whereby the main purpose is to identify features significant for flow and transport. Results from this work will be published in BRAUCHLER ET AL. [2005].

In chapter 3 the theory of the hydraulic travel time approach is presented. The approach enables the inversion of several travel times independent from the kind of source. The introduced approach has been applied to data from a set of pneumatic short term test conducted to a gas saturated fractured sandstone block. The results and the interpretation are given in chapter 4. Results from the work presented in chapter 3 and 4 are published in BRAUCHLER ET AL. [2003a,b].

In chapter 5, a detailed systematic study of the inversion based on different travel times characterizing the recorded transient pressure pulse is presented. The data base comprises simulated multi level slug tests arranged in a tomographical array.

An overall summary and final conclusions are presented in chapter 6.

In chapter 7, an outlook is given concerning the concept of the diffusivity measurements on field scale. The mathematical derivation is given for calculating the diffusivity as a function of a stimulation impulse at a well, and the arrival time of the maximum pressure change at the observation well.

2 Multivariate Statistical Approach for characterizing a cubic sandstone block

2.1 Introduction

A promising approach for the investigation of fractured porous hard rocks are tomographical experiments. For the investigation presented in the following, the concept of tomographical investigations is applied by conducting flow and transport measurements to a cubical gas saturated fissured sandstone block of 60 cm edge length in order to identify the spatial variability of hydraulically significant features within the block.

The presented flow and transport experiments are conducted using a gas flow and gas tracer technique that enables the generation of various flow field patterns via adjustable boundary conditions [McDERMOTT ET AL., 1999]. An advantage of the use of the gas flow techniques compared to hydraulic test methods is that flow and transport experiments can be conducted much faster. The technique of using gas in characterizing the subsurface became more and more important [BAEHR & HULT, 1991; ILLMAN & NEUMANN, 2001, VESSELINOV ET AL., 2001a,b].

In literature, two different approaches are discussed for the interpretation of flow and transport data and for the investigation, quantification, and predictions of the relevant processes in fissured and fractured hard rocks: i) deterministic approaches [HUANG ET AL., 1999; KARASAKI ET AL., 2000; LONG & BILLAUX, 1987] and ii) statistic approaches [CLIFTON & NEUMAN, 1982; DAGAN, 1982; HARTER & YEH, 1996; YEH & ZHANG, 1996].

Usually, both approaches are based on measured head, flow, and transport data, a priori information, or assumptions on the investigated system. In the case of the deterministic approach the aim is to develop a model representing the complexity of the investigated system to some extent. For model development mostly geological or geophysical a priori information or a combination of both combined with a certain amount of recorded flow and transport data are used. In contrast the stochastical approaches are based on the statistic of rock parameters, which are derived from field and laboratory data. Using a statistic simulation algorithm and varying the input parameters, different realizations can be obtained. In both approaches, the model results are compared to experimental data. Usually, neither of the cited approaches includes an a priori investigation of the measured data sets for a differentiation of significant characteristics that are inherent in the observed flow and transport information. However, such a differentiation can particularly be appropriate for fractured porous media,

- due to the strong anisotropy and significant contrasts in the hydraulic conductivity in hard rocks, and
- since the measured data sets reflect the spatial variation of the distribution of the

hydrogeological parameters (e.g., hydraulic conductivity, dispersivity) as well as the physical and hydrogeological boundary conditions that have an increasing influence on the experiments especially in three dimensional, high-resolution investigations like tomographical approaches.

In this chapter an approach is introduced that is based on methods of multivariate statistics, which

- allows to account for certain characteristics that are inherent in the data of flow and transport experiments,
- enables a rigorous and objective classification of results from flow and transport experiments,
- allows to define an average system response, independent of boundary conditions,
- allows for the identification of parameter zonation in terms of structure identification.

Multivariate statistics are already successfully applied in nearly all fields of geology and geophysics [MALMGREM & BILAL, 1982; DUMAY & FOURNIER, 1988, GILL ET AL., 1993, SCHAD, 1996, FECHNER & DIETRICH, 1997, DIETRICH ET AL., 1998, HAMAH & CURRAN, 1998, MENG & MAYNARD, 2001, WANG ET AL., 2001, BOSCH ET AL., 2002, GÜLER ET AL., 2002, TRONICKE ET AL., 2004]. For the classification of the flow and transport data using multivariate statistics, the investigated object is handled as a black box, thus no information on the investigated system is required, ensuring the objectivity of the approach.

2.2 Data acquisition

A sandstone block of 60 × 60 × 60 cm^3 in size is recovered from a Stubensandstein formation which is carried in the southern part of Germany. This formation is part of a continental alluvial depositional system [HORNUNG & AIGNER 1999] and is mainly composed of arkose sandstone. The sample was situated in a bed load channel dominated facies. Figure 2.1 illustrates the investigated sandstone block prior to the preparation for the experiments.

Figure 2.1 The photograph shows the cubic sandstone block prior to the resin coating. On each side are seventeen ports for injection and extraction of the tracer [from LEVEN ET AL., 2004].

2.2.1 Sample preparation

The block was cut to precise cubic shape, which enables the definition of geometrical boundaries and the performance of experiments with same measuring set-up and therefore directly comparable results. The physical properties of the fissured sandstone block are listed in Table 2.1. For drying purposes the sandstone block was stored several weeks in a heated room. According to MAUCH [1993] the maximum saturation from humid air for this type of sandstone can be 12 %.

In order to allow for a verification of the multivariate statistical approach a detailed mapping of the petrofabric and fissure network was conducted using a polyethylene foil.

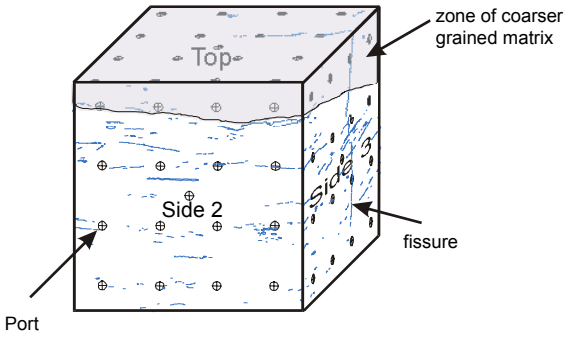

Figure 2.2 Diagram of the fissured block (*60 × 60 × 60 cm³)* illustrating the fissure network and two zones with different matrix composition.

Significant features like fissures, fissure apertures and a zone with coarser grained matrix were drawn onto the foil (Figure 2.2).

To access the block for flow and transport experiments, 17 ports with three centimeters in diameter were attached in a regular grid on each side of the block. The ports are circular metal plugs that allow for access to a controlled area of the block (Figure 2.1). Finally, the block was coated with six different resin layers allowing for tracer tests with pressures up to three bar (Figure 2.3). A detailed description of the block preparation is given in [LEVEN ET AL., 2004].

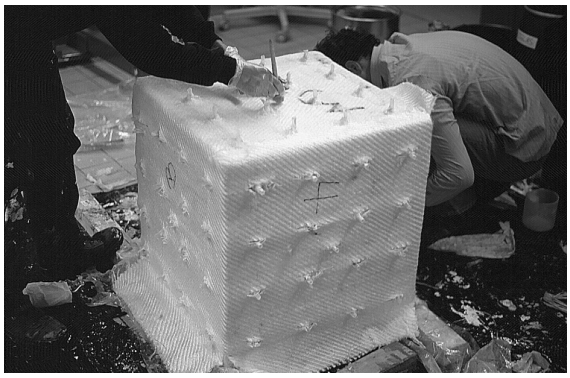

Figure 2.3 Photograph of the resin coating of the sandstone block [from LEVEN ET AL., 2004].

Table 2.1 Physical properties of the cubic sandstone block.

Size	60 × 60 × 60 cm³	
Weight	Approx. 500 kg	
Porosity for the upper Stubensandstein	19,5 %	1
	7 – 23 %	2
	10-25 %	3
Grain Density	2650 kg/m³	1
Range of fracture apertures	< 2 mm	

[1]MAUCH [1993], [2]BENGELSDORF [1997], [3]HELING [1963]

2.2.2 Experimental set-up

In order to characterize the fissured sandstone block in terms of heterogeneity and anisotropy, flow and transport experiments were conducted using a gas flow and gas transport technique developed by MCDERMOTT [1999]. Gas flow parameters can be converted easily to corresponding hydraulic parameters [RASMUSSEN ET AL., 1993, BLOOMFIELD & WILLIAMS, 1995, JARITZ, 1998]. The experimental set-up is shown in Figure 2.4. Compressed air is injected into the sandstone block through one port and the flow rate is measured at the port at the opposite block face using a mass flow meter. After a stationary flow field is established, a gas tracer (helium) is injected via a bypass loop and is detected by a mass spectrometer. The transport experiments are conducted by using one port for injection and the port on the opposite side for extraction of the tracer. The distance between the opposed ports in each experiment is 60 cm. Figure 2.6a summarizes the used port-port connections for one spatial direction. For the other two directions the same relative positions of the ports were chosen. According to JARITZ [1998] the effects of compressibility can be neglected by using experimental conditions as listed in Table 2.2.

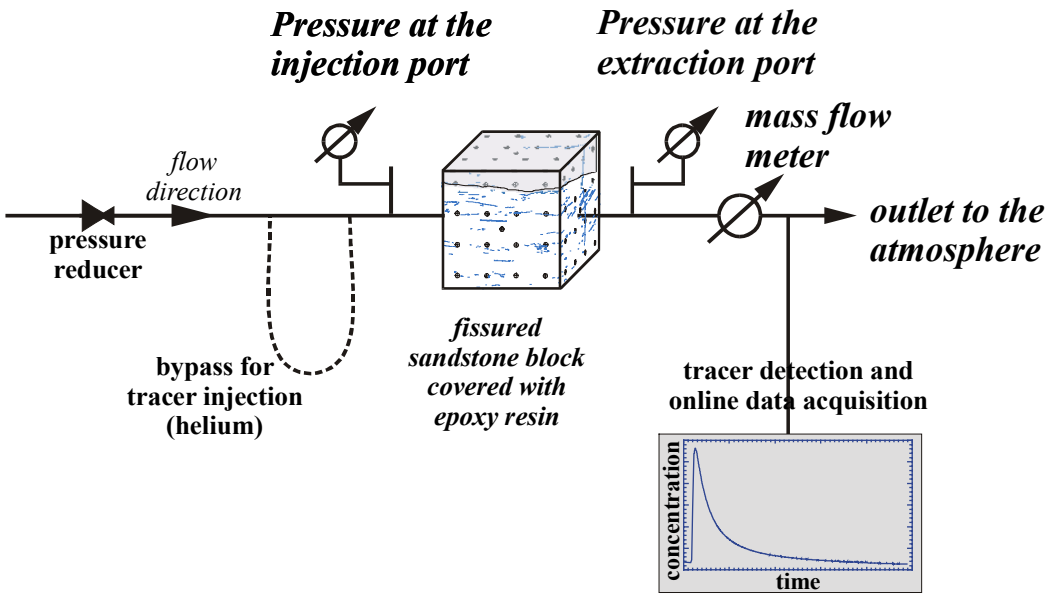

Figure 2.4 Experimental set-up (after MCDERMOTT, 1999).

Table 2.2 Experimental conditions for the measurement.

Pressure difference between injection and extraction port	500 mbar
Used tracer	Helium
Volume of the bypass loop	105 ml
Port - port distance for each experiment	0.6 m

2.3 Methodology

The main goal of the proposed statistical procedure is the identification and characterization of representative data sets, reflecting different zones with quasi homogenous flow and transport properties within the investigated system. The different steps of the statistical procedure can be summarized as follows (Figure 2.5): The initial point of the statistical analysis is a sufficient data base including results of comparable experiments. The next steps are the definition

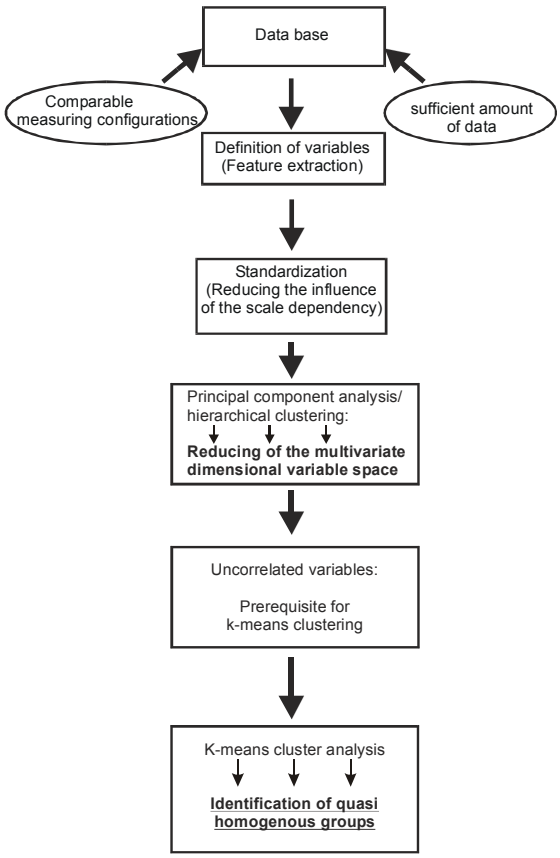

Figure 2.5 Illustration of the different steps of the statistical procedure.

and standardization of variables describing the results of the conducted experiments. The standardization enables the comparison of variables with different units. After

standardization the values of each variable have a mean of 0 and a standard deviation of 1. Note, that standardizing does not change the shape of the distribution. A prerequisite for the classification of the flow and transport experiments by means of k-means cluster analysis are uncorrelated variables. In order to identify the number of appropriate variables and the variables themselves describing the results of the flow and transport experiments a combination of Principal Component Analysis and hierarchical clustering is performed. The final classification of the flow and transport processes are conducted by means of k-means clustering analysis. In order to verify the classification the mapping of the petrofabric and fissure network prior to the resin coating can be used.

2.3.1 Database

Generally, a sufficient amount of data and the comparability of the experimental results are fundamental prerequisites for reliable statistical investigations. The appropriate amount of data can only be determined by means of the statistical results, since there are no definite rules how many objects are necessary to perform a distinct statistical procedure. As shown later, the illustrated database (Figure 2.6) is sufficient as the results of the statistical investigation indicate. The conducted experiments are classified by means of the spatial position of their injection and extraction ports, yielding sets of comparable experimental results with equal distance to the block boundaries. The cubic shape of the block and the regularly arranged ports (Figure 2.1) allow such a separation of the experimental results into three groups with exactly the same measuring configuration. These three groups and the spatial position of their ports are shown in Figure 2.8. The measuring configuration is characterized by the position of the used ports. For example, for the first group (Figure 2.8d) the opposing ports in the corners are used for the measurement (Figure 2.8a). Consequently, four measurements with the same measurement configuration can be conducted for each spatial direction. Taking into account, that the breakthrough curves do not depend on the direction of the applied flow field, 12 measurements with the same geometrical configuration can be carried out for the first group, 24 for the second group and 12 for the third group.

a)

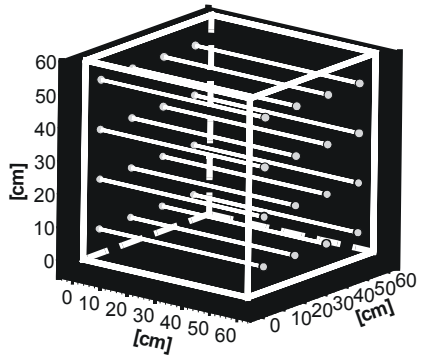

b)

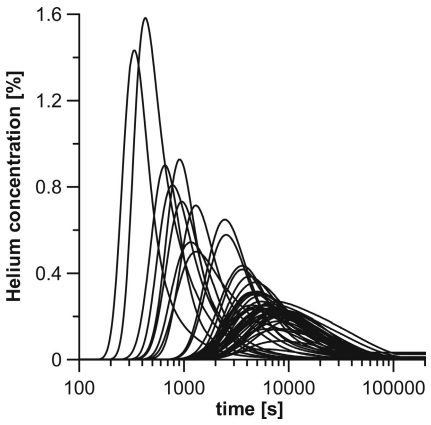

Figure 2.6 (a) Illustration of the 16 used port-port connections for one of three spatial directions. Note, that for each flow and transport experiment, only one of the shown configurations is used. (b) Recorded breakthrough curves of all 48 tracer experiments conducted to the sandstone block.

The influence of the spatial position of the ports for the three groups on the breakthrough of the tracer is shown by means of numerical investigations. Therefore, the numerical model

STRAFE 6 (**S**trömung und **TRA**nsport in **Fe**stgesteinsaquiferen), which was developed at the University of Aachen, is used. Interested readers are referred to BIRKHÖLZER [1994] and JANSEN [1999]. The transport calculations are conducted using a three dimensional homogenous model and the parameters are summarized in Table 2.3.

The modeled breakthrough curves (Figure 2.7) are strongly influenced by the distance of the used port-port configuration to the block boundaries. The closer the two opposite ports are located to the block boundary, the earlier, higher and narrower the peak. From the comparison of Figure 2.8d) - f) the influence of the measuring configuration becomes also evident.

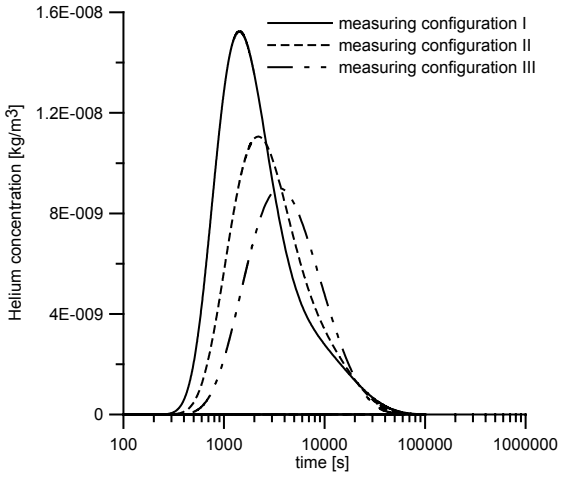

Figure 2.7 Simulated curves for each measuring configuration.

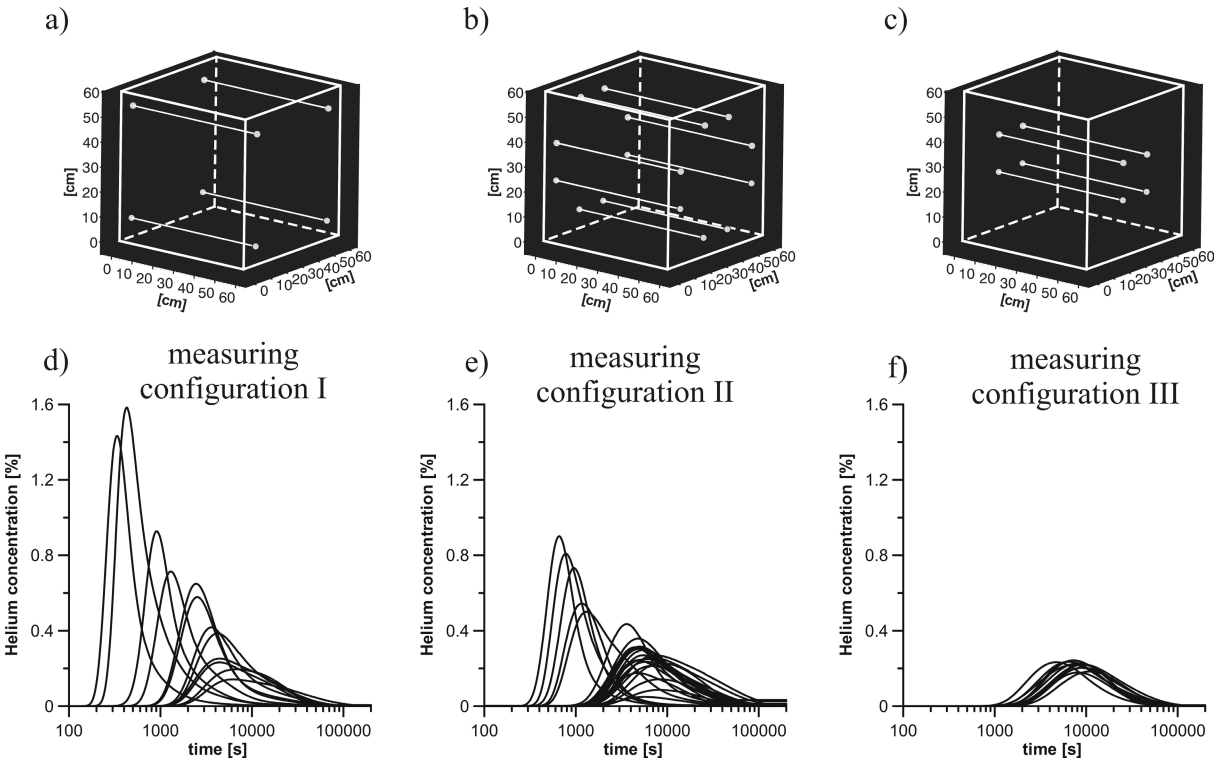

Figure 2.8 Illustration of the separation of breakthrough curves based on their spatial position of the port-port configuration. (a) – (c) indicate the possible spatial positions of the used port-port connections for one of three spatial directions for each group of breakthrough curves. (d) – (f) illustrate the breakthrough curves classified with respect to their spatial position of the port-port configuration.

Table 2.3 Input parameters for the simulated breakthrough curves, illustrated in Figure 2.7.

Permeability	4.00E-14 m^2
Porosity	0.15
Longitudinal dispersion	6.66821e-02 m
Transversal dispersion	1.323610e-02 m
Vertical dispersion	1.323610e-02 m
Diffusion coefficient	7.500000e-06 m^2/s

Without fundamental assumptions about the structure of the block leading to restricted interpretations, it is not possible to remove the influence of the measuring condition on the breakthrough of the tracer. To account for this, the presented statistical methodology is conducted separately for each of the three distinct measuring configurations.

The processing summarized in section 2.3 is presented in detail only for the experiments with measuring configuration I as shown in Figure 2.8a). However, the results and the interpretation are illustrated for the whole database.

2.3.2 Definition of Variables Characterizing Flow and Transport Experiments

To ensure the objectivity of the approach, variables are chosen that can directly be derived from the experimental data, such as definite breakthrough times or measured flow rate. Consequently, the described statistical approach is based on the measured flow rate and the recorded breakthrough curves, i.e. times when 25 %, 50 %, and 75 % of the mass have broken through. The measured flow rates show a lognormal distribution (not shown here), thus the logarithm of the flow rates is used in the following statistical investigation. Furthermore, variables are used describing the run and spread of the curves. In order to describe the run of the curves, the times of the mass-quartiles are chosen.

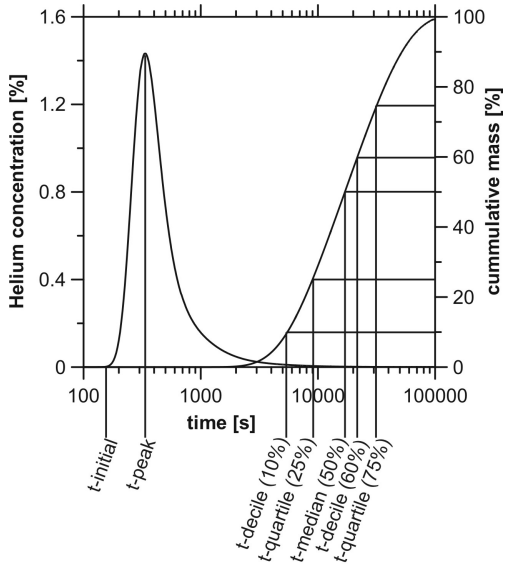

Figure 2.9 Illustration of the variables derived from the recorded breakthrough curves and used in the multivariate statistical analysis: t-initial, t-peak, t-quartile-(25%, 75%), t-decile-(10%, 60%). An unconformity coefficient is calculated as the ratio of the t-decile (60%) and the t-decile (10%).

Table 2.4 The minimum and maximum value of each variable used for the statistical investigations. The unconformity coefficient is the quotient of the t-decile (60%) and the t-decile (10%).

Variable	Range
Log flow rate [ml/min]	1.6 - 2.9
t-initial [s]	146 - 1252
t-peak [s]	335 - 6572
t-quartile 25% [s]	378 - 10909
t-median [s]	593 - 20537
t-quartile 75% [s]	1809 - 35876
Unconformity coefficient	2.7 – 6.3

The spread of the curve is described by the quotient of the times of the 60% and the 10% decile (in the following called unconformity coefficient) with respect to the recovery of the

injected tracer. This quotient is taken in analogy to sieve curve analysis, where it is used to empirically determine hydraulic conductivities of unconsolidated sediments [BEYER, 1964]. Additionally, the time of the initial breakthrough (t-initial) and the peak arrival time (t-peak) are used (Figure 2.9). The variables and their ranges are listed in Table 2.4.

2.3.3 Reducing of the Multidimensional Variable Space

The objective of the first part of the statistical investigation is i) to determine the maximum number of variables that are sufficient to describe the investigated system and ii) to identify uncorrelated variables describing the flow and transport system of the cubic sandstone block. Uncorrelated variables are a prerequisite for many statistical methods such as k-means cluster analysis, which will be described in section 2.3.4.

A suitable tool for the analysis of the correlation between available variables is Principal Component Analysis (PCA). For the verification of the results of the PCA, the application of a hierarchical cluster analysis can be appropriate in some cases in order to identify uncorrelated variables. As shown later, the combination of these two methods allows an objective identification of uncorrelated variables for the classification of the breakthrough curves. For the statistical procedures, the standardized matrix of the defined variables is used as starting point. The statistical investigations were carried out using the software package Systat®9.

Principal Component Analysis

In the Principal Component Analysis (PCA) [JÖRESKOG ET AL., 1976], each observed variable can be expressed as a linear combination of several components as described by

$$z_{kj} = \sum_{q=1}^{Q} a_{jq} \cdot p_{kq} ,$$

Eq. 2.1

where z_{kj} is the observed value of variable j with respect to experiment k (i.e., breakthrough curve), p_{kq} is the value of component q in experiment k, a_{jq} is the component loading with regard to variable j and Q is the number of components. In order to allow a better interpretation, the factors are rotated. In our approach the so called "varimax method" according to KAISER [1958] is used. In this method the number of variables, that have high loadings on each component, is minimized by an orthogonal rotation of the coordinate system.

Hierarchical Cluster Analysis

In hierarchical clustering [ANDERBERG, 1973; HARTIGAN, 1975] the most similar observations are taken to define a cluster. Successively, the next most similar observations are connected to the initially defined clusters. By combining two objects (clusters) P and Q, the distance D(R,P+Q) can be expressed between the new group (P+Q) and any other group R as follows:

$$D(R,P+Q) = A \cdot D(R,P) + B \cdot D(R,Q) + E \cdot D(P,Q) + G \cdot \left| D(R,P) - D(R,Q) \right|$$

Eq. 2.2

D(R,P): Distance between the groups R and P

D(R,Q): Distance between the groups R and Q

D(P,Q): Distance between the groups P and Q

The constants A, B, E and G vary with respect to the used algorithm (Table 2.5). Further information can be found in

BACKHAUS, [2003]. Unfortunately, no answer exists in the literature about the most appropriate method for hierarchical clustering. For the presented study, the complete linkage method is chosen, since it yields the most satisfactory results. The complete linkage algorithm uses the most distant pair of objects in two clusters to compute their distances. This method tends to compact globular clusters.

Table 2.5 Values for the constants used for the complete linkage method.

A	B	E	G
0.5	0.5	0.5	0.5

2.3.4 Processing of Data

In order to objectively determine an appropriate number of independent components and variables, respectively, the "scree" test method is used. This test uses the components' eigenvalues E_j that are arranged in a coordinate system. The eigenvalues are calculated as the sum of the squares of the component loadings a_{jq} of one component q over all variables and can be expressed as follows:

$$E_j = \sum_j a_{jq}^2$$

Eq. 2.3

The smallest points converging to the x-axis asymptotically are connected. The last point (elbow) on the straight line determines the number of components (Figure 2.10). In this case three components have to be chosen. The eigenvalues and the cumulative variance describing the complete system in dependence of the number of components are listed in Table 2.6. Note, the first three components have much higher eigenvalues than the rest of the list, and they account for 99.44 % of the total variance. The next step is to determine the variables representing the three independent components. The procedure is illustrated in detail for measuring configuration I (Figure 2.11). Therefore, the results of the PCA and hierarchical cluster analysis are used. The dendrogram (Figure 2.11d) resulting from the hierarchical clustering is separated in three equidistant parts (0.62) based on the complete distance (1.86). In part I the cluster contains five variables with a distance < 0.62. In part II the "unconformity coefficient" joins the cluster at a distance of 1.15 and in part III the "log flow rate" joins at a distance of 1.86. Based on the equidistant separation, the variables "unconformity coefficient" and "log flow rate" are chosen representing part II and III, respectively.

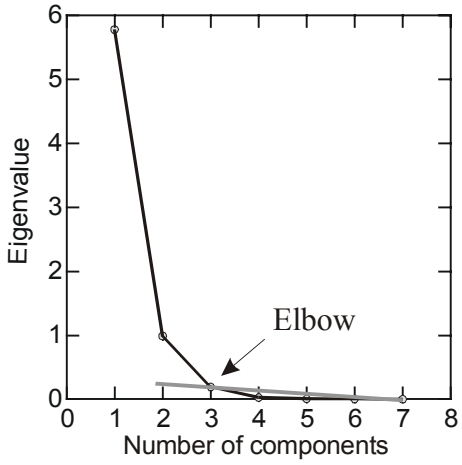

Figure 2.10 The Screeplot illustrates the eigenvalues of the components. The elbow point indicates the number of appropriate components required for the further analysis of the data set.

Table 2.6 Eigenvalues and cumulative variance of the components. No. states the number of components.

No.	Eigenvalue	Cumulative Variance
1	5.778	82.537
2	0.99	96.678
3	0.194	99.444
4	0.027	99.828
5	0.007	99.926
6	0.005	99.991
7	0.001	100

a)

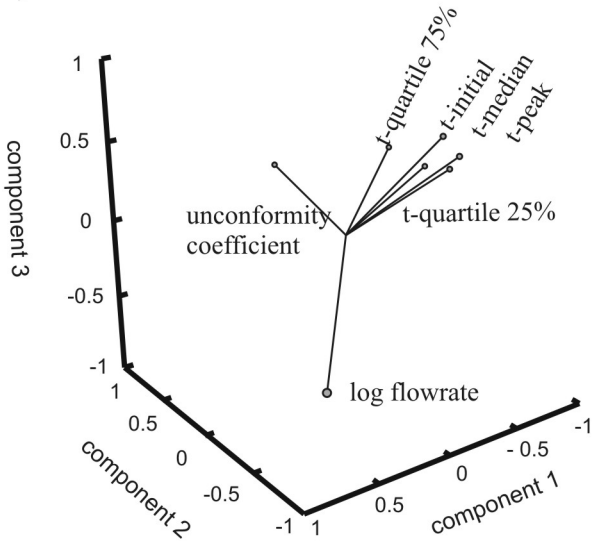

b)

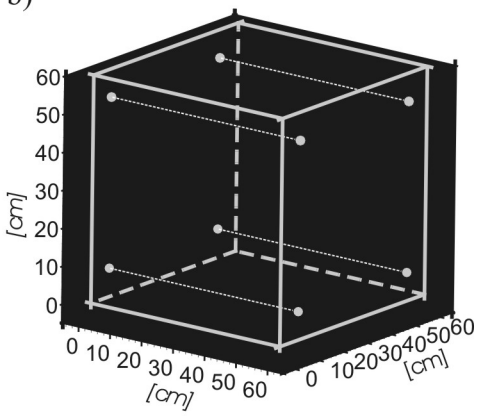

c)

variables	component 1	component 2	component 3
log flowrate	-0.545	-0.571	-0.613
t-initial	0.901	0.208	0.373
t-peak	0.956	0.109	0.358
t-median	0.912	0.39	0.122
t-quartile 25%	0.966	0.209	0.142
t-quartile 75%	0.769	0.585	0.225
unconformity coefficient	0.143	0.979	0.123

d)

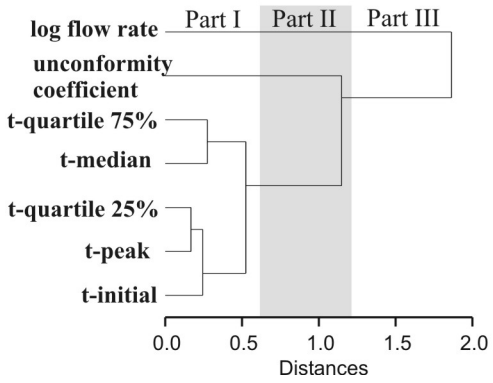

Figure 2.11 (a) Plot of the results from the Principal Component Analysis of measuring configuration I. (b) Spatial position of the used port-port connections for one of three spatial directions of measuring configuration I. (c) Factor loadings of the rotated loading matrix of measuring configuration I. (d) Dendrogram of the hierarchical clustering of measuring configuration.

Table 2.7 Summary of the selected variables which are used for the k-means cluster analysis.

Measuring configuration	Selected variables			
I	Log flow rate	Unconformity coefficient	t-quartile 25%	
II	Log flow rate	Unconformity coefficient	t-peak	
III	Log flow rate	Unconformity coefficient	t-quartile 25%	t-initial

The choice of the third variable is much more difficult, thus the results of the PCA and the hierarchical clustering analysis are combined. The calculated component loadings are given in Figure 2.11c) and are visualized in Figure 2.11a). The rotated loading matrix describes the correlation between the variables and the components. A correlation coefficient of 0 indicates that the variable can not be predicted from the component by using a linear equation whereas a correlation coefficient of 1 indicates that a variable can be predicted perfectly by a

linear function of the component with a positive slope. And a value of –1 indicates the same except that the function has a negative sign for the slope. The rotated loading matrix of the PCA (Figure 2.11c) shows that component 2 is highly correlated with the variable "unconformity coefficient" and that the variable "log flow rate" is more or less correlated with all three components. Because of this, the third variable should be highly correlated with component 1 and poorly correlated with components 2 and 3. Based on these requirements the variable t-quartile 25% is chosen. Table 2.7 lists the selected variables of all three measuring configuration which are used for the classification of the breakthrough curves illustrated in section 2.4.

2.3.5 Classification of the Flow and Transport Data Using k-means Cluster Analysis

The objective of the following statistical analysis is the splitting of the breakthrough curves into quasi-homogeneous groups by the determined variables that characterize the different groups. This allows for the identification and characterization of representative data sets, reflecting different zones with quasi-homogeneous flow and transport properties within the investigated system. In the presented approach the k-means clustering [*McQueen*, 1969] is used for the splitting, since k-means cluster analysis is a powerful tool to objectively identify natural groupings. Due to the tomographical array of the injection and extraction ports it is possible to identify the spatial distribution of the different flow and transport characteristics.

For the k-means clustering each breakthrough curve is handled as "case", characterized by the defined uncorrelated variables. The procedure begins by picking "seed cases", one for each cluster, which are separated from the center of all other cases as much as possible. Note, the number of clusters has to be predetermined. Then the cases are allocated to their nearest "seed". Successively, the cases are iteratively rearranged by reducing the total sum of squares within each cluster

$$\varphi = \sum_{i=1}^{K} \sum_{j=1}^{p} \sum_{m=1}^{n_i} (x_{v_{im},j} - \bar{x}_{i,j})^2$$

Eq. 2.4

where v_{im} denotes the row index of the m-th observation (breakthrough curve) in the i-th cluster in matrix X (X is an $a \times b$ matrix with a observations and b variables), $\bar{x}_{i,j}$ is the average of the non-missing observations for variable j in cluster i, n_i is the number of rows in X assigned to cluster i, p is the number of variables, and K denotes the number of clusters to be obtained. This processing continues for a given number of clusters, until the sum of squares can be no longer reduced.

2.4 Results and Interpretation

The classification starts by splitting up the breakthrough curves into two clusters by using the least correlated variables. Next, the number of clusters is increased and the same procedure is performed with three or more clusters. To determine the number of clusters useful to describe the system with a reasonable certainty a stop criteria is defined. The classification results illustrated in Figure 2.12-14 are proposed and discussed separately, beginning with measuring configuration I.

Measuring configuration I:

The comparison of the classifications (a) and (b) in Figure 2.12 shows that the clusters a/1 and b/1 are identical. The stability of the two clusters indicates that each of these two clusters represents a quasi homogenous group of breakthrough curves. Thus, it can be assumed that the clusters represent different

parts of the sandstone block with a homogenous parameter distribution. The splitting of cluster a/2 leads to a more detailed classification, thus three clusters can be used for characterizing flow and transport. The use of four clusters leads to a mixing of breakthrough curves of two different clusters; cluster c/4 includes breakthrough curves of cluster b/1 and b/3. The mixing would indicate that the previous classification based on only three clusters does not represent homogenous groups. For this reason the mixing of breakthrough curves is defined as stop criterion. The described classification reveals that three different groups with a homogeneous distribution of flow and transport parameters within each group can be distinguished, which are represented by the breakthrough curves of clusters b/1, b/2, b/3.

In order to interpret the classification, the spatial position of the used port-port connections and the mapping of the petrofabric and fissured network prior to the resin coating is used. The splitting into cluster a/1 and a/2 fits with the deterministic separation with respect to the texture of the matrix and the bedding. Cluster a/1 contains all breakthrough curves recorded from direct connections to the upper part of the cubic block which consists of a coarser grained matrix (Figure 2.12). The fifth breakthrough curve of cluster a/1 (dashed line) was measured for a port-port connection in the lower fine grained part of the block. A more detailed mapping of the petrofabric based on photographs of the block prior to the resin coating shows that also in the vicinity of the ports of this connection the matrix is coarser. The breakthrough curves of cluster a/2 are recorded from the lower part of the block which consists of a finer grained matrix or the breakthrough curves are recorded orthogonal to the bedding (recorded from bottom to top). The shape of the curves within a distinct cluster corresponds also well with the petrofabric derived from the mapping of the block. E.g., the breakthrough curves of cluster a/1 are characterized by an initial and dominant breakthrough occurring at significantly earlier times with a sharp concentration increase up to the peak, while the breakthrough curves of cluster a/2 are characterized by a broad and flat shape. This indicates that the upper part is dominated by better interconnected pores with a higher permeability than the lower part.

The classification of the breakthrough curves using three clusters allows to distinguish the breakthrough curves of cluster a/2 recorded orthogonal to the bedding (cluster b/2) from the breakthrough curves recorded parallel to the bedding with direct connections to the finer matrix (cluster b/3). The experiments conducted orthogonal to the bedding (from bottom to top) are dominated by lower flow rates. This agrees with the shape of the breakthrough curves of cluster b/2, because the first initial breakthrough occurs at earlier times than the breakthroughs of cluster b/3.

The classification shows that the matrix properties and the bedding dominate the system while the fissure network has no evident influence on the flow and transport experiments. It is refrained from describing the breakthrough curves from the clusters c/1 to c/4, as the classification leads to an unreliable result, because cluster c/4 includes breakthrough curves of cluster b/1 and b/3.

Measuring configuration II:

The breakthrough curves of measuring configuration II can be separated into four clusters (Figure 2.13) without breaching the defined stop criteria. The splitting into two clusters allows to differentiate the breakthrough curves recorded from direct connections to the upper part of the sandstone

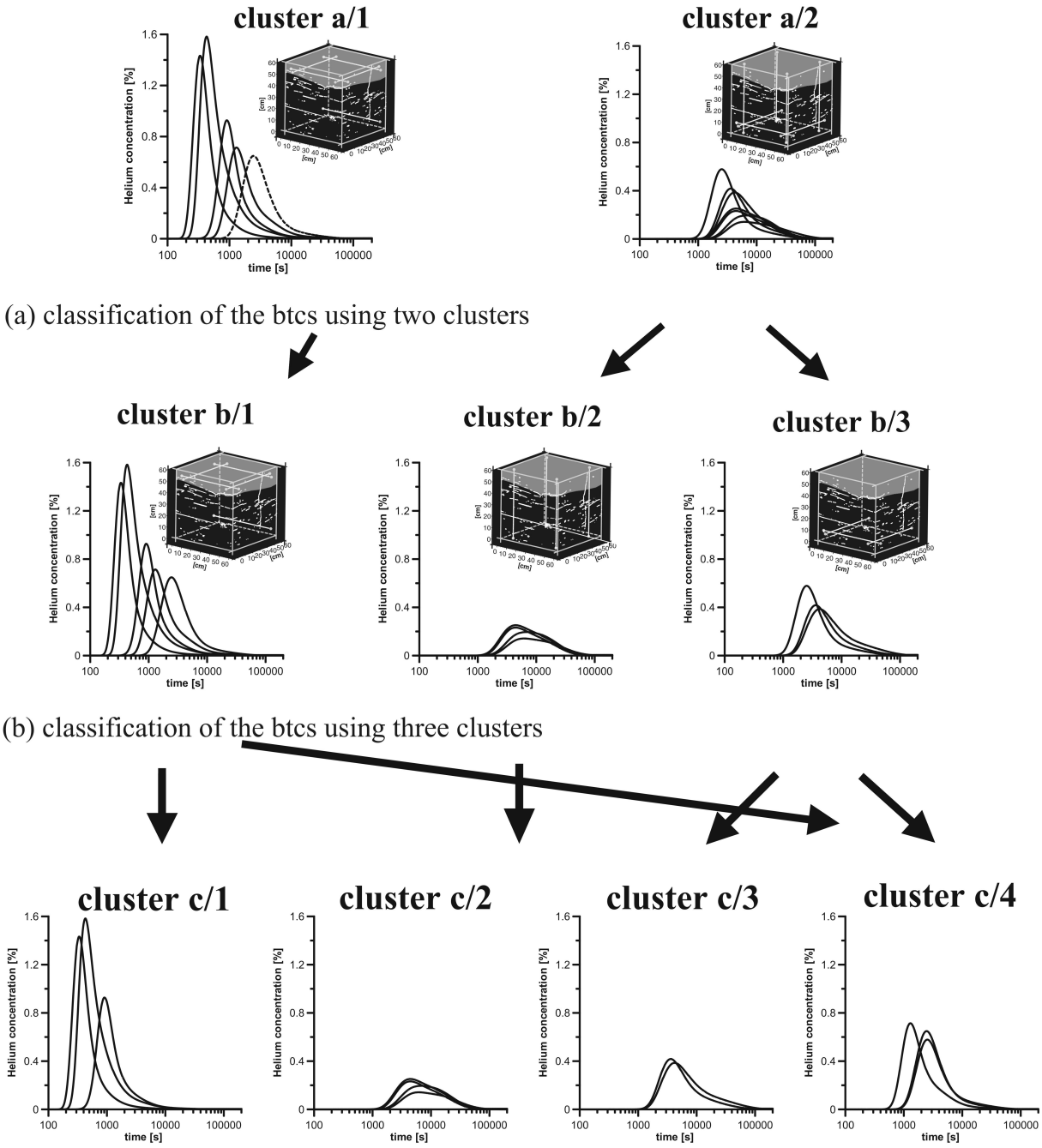

Figure 2.12 Classification results of measuring configuration I using k-means cluster analysis. The white lines in the images of the sandstone block indicate the used port-port-configurations.

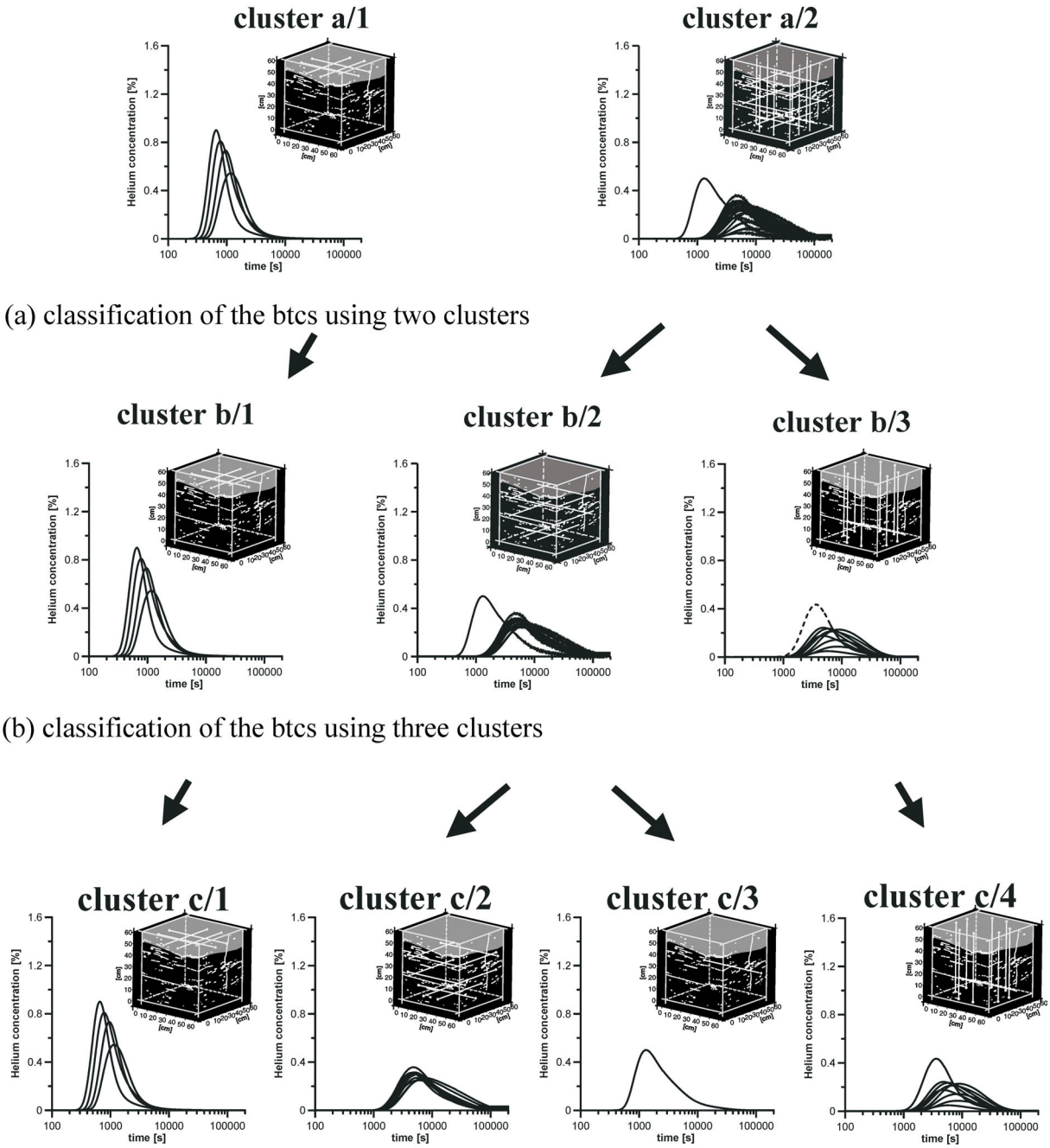

Figure 2.13 Classification results of measuring configuration II using k-means cluster analysis. The white lines in the images of the sandstone block indicate the used port-port-configurations.

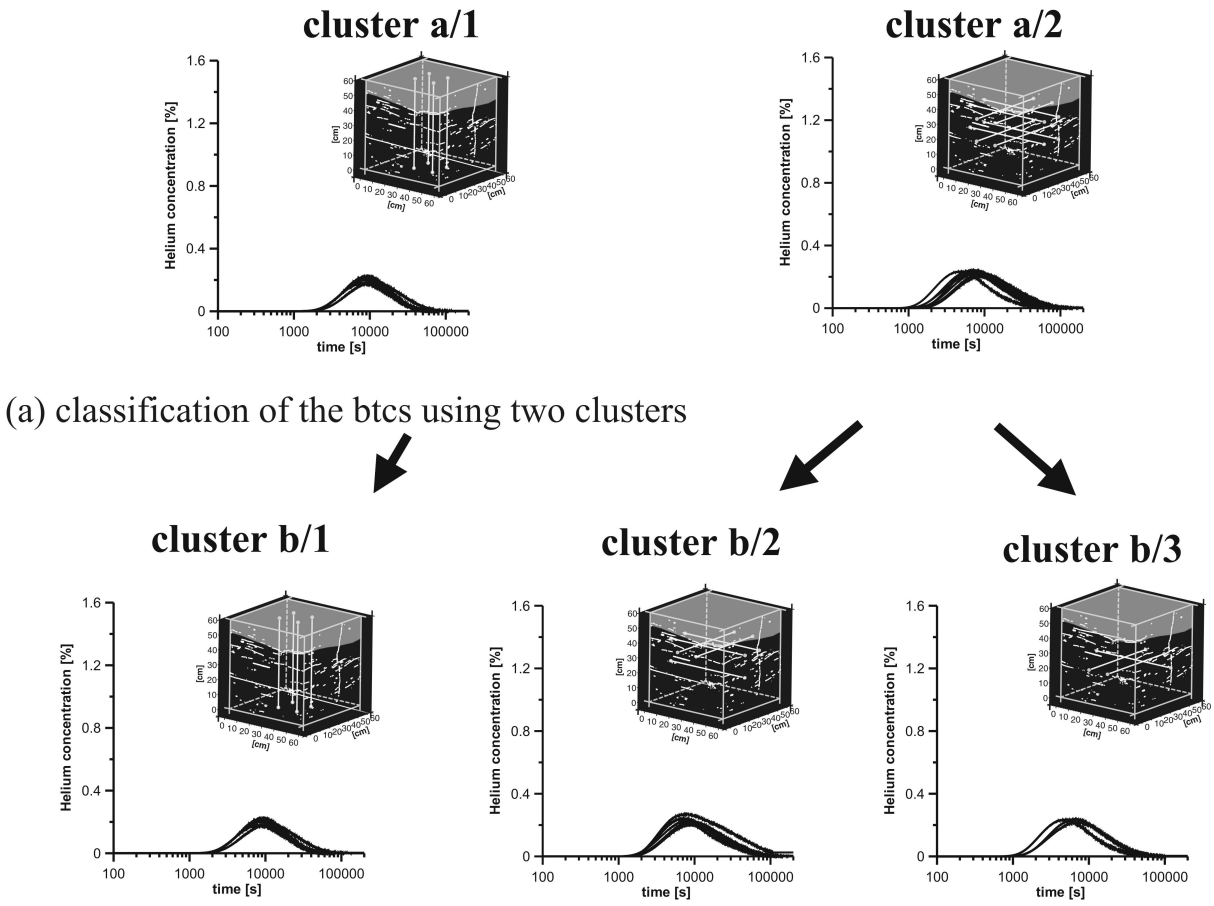

Figure 2.14 Classification results of measuring configuration III using k-means cluster analysis. The white lines in the images of the sandstone block indicate the used port-port-configurations.

.

block which consists of a coarser grained matrix (cluster a/1) from the remaining breakthrough curves (cluster a/2). The shape and run of the breakthrough curves in the respective clusters match with the petrofabric derived from the surface mapping of the block. The breakthrough curves of cluster a/1 are characterized by an early initial breakthrough and a steep rise up to the peak. This coincides with the results of measuring configuration I and confirms that the upper part of the block is more permeable than the lower part.

By using three clusters, cluster a/2 is separated into two further groups of breakthrough curves, which are recorded parallel (cluster b/2) or orthogonal (cluster b/3) to the bedding. Cluster b/3 includes one breakthrough curve (dashed line) which is recorded parallel to the bedding. The mapping of the petrofabric of the sandstone block gives no structural information for explaining this behavior. Cluster b/1 and a/1 are identical.

The classification of the breakthrough curves using four clusters leads to a splitting of cluster b/2 comprising breakthrough curves recorded parallel to the bedding. Due to the geological mapping it is not possible to explain the further splitting but the run and spread of the breakthrough curve imaged in cluster c/3, indicate flow and transport properties which

are completely different from the breakthrough curves of cluster c/2. This points out that the before mentioned proceedure may lead to more reliable and objective classification results than the regular use of geological a priori information. Note, that usually under field conditions such detailed structural information about the investigated area is not available.

Measuring configuration III:

The data base of measuring configuration III comprises no breakthrough curves recorded in the upper part of the block consisting of a coarser grained matrix. It is remarkable that all breakthrough curves show more or less the same elongated shape, which does not seem to reflect impacts of one or two dominating features. For this reason it is not surprising that four variables are needed to describe the flow and transport system, whereas for measuring configurations I and II three variables are sufficient (Table 2.7).

The splitting into two clusters (Figure 2.14) allows to perfectly distinguish the breakthrough curves recorded orthogonal (cluster a/1) and parallel (cluster a/2) to the bedding. By using three clusters the breakthrough curves recorded parallel to the bedding are separated into two further groups (clusters b/2 and b/3). Both the mapping as well as the shape of the curves give no satisfying explanation for this separation. One reason for this splitting might be the composition of the petrofabric of the upper part of the sandstone block. That means, the length scale of the heterogeneities dominating flow and transport in the block is smaller than the scale of detection (observation) method and measurement density, respectively. Hence, the classification results based on three clusters are not considered for the development of a numerical model mentioned in section 2.5. By using more than three clusters the defined stop criterion is breached.

2.5 Summary and Conclusions

In this chapter a multivariate statistical approach is presented and applied to flow and transport experiments which were conducted to a gas saturated fissured sandstone block on laboratory scale. The approach enables a rigorous, objective classification of results from flow and transport experiments into characteristic, quasi homogenous groups. These quasi homogenous groups can be interpreted to reflect the different flow and transport properties of the investigated system. Due to the tomographical array of the injection and extraction points of the tracer it is possible to determine the spatial distribution of the flow and transport properties.

The approach is illustrated by analyzing 48 flow and transport experiments, which are conducted to a fissured cubic sandstone block with an edge length of 60 cm. The cubic shape of the block and the regular array of the injection and extraction ports enables a clear definition of three different measurement configurations. The influence of the distance between block boundaries and injection and extraction ports, respectively, on the shape of the breakthrough curves prohibits to simultaneously apply the procedure to all conducted experiments. The separation of the experiments according to the measurement configurations ensures the comparability of the data.

For the multivariate statistics, variables are chosen describing the run and spread of the recorded breakthrough curves. Additionally, the measured flow rate of each recorded breakthrough curve is used. The classification of the flow and transport experiments is conducted by k-means cluster analysis. A prerequisite for the application of k-means cluster analysis are uncorrelated variables. In order to identify objectively uncorrelated

variables a methodology has been developed which combines the results of Principal Component Analysis and Hierarchical Cluster Analysis.

From the results of the statistical approach it is concluded that the system is determined mainly by two quasi homogenous layers of different permeability and that there is no significant influence of high permeable fissures. A detailed geological surface mapping of the investigated sandstone block agrees with the determined spatial position of the two layers and the derived properties. The conformity between the statistical and the geological classification demonstrates that the presented multivariate statistical approach is a powerful tool for detecting natural groupings, i.e., zones with a homogeneous distribution of flow and transport parameters within each zone. In some cases the mentioned proceeding leads even to more reliable and objective classification results than the regular use of geological a priori information.

The investigations point out that it is useful to conduct measurements under comparable conditions both in the field and in the laboratory allowing to compare the experiments and to conduct a reliable classification. Thus, it is possible to characterize and simplify complex systems without losing essential information. The proposed approach can be transferred to the field without any restrictions as the sandstone block is handled as a black box, i.e., no a priori information is used for the identification of zones within the block.

By setting up a numerical model, based on the proposed classification results and comparing the simulated results with the measurements a research group at the University of Stuttgart has verified the assumed layered structure distribution of the fissured sandstone block. Additionally, strong and realistic indications of minor heterogeneities, in shape of thin low permeable horizontal layers within the upper layer and also in the upper part of the lower layer could be found. Readers interested in the numerical model set-up and the determination of the input parameters are referred to SÜß [2004]. The agreement between the measured and modeled breakthrough curves shows that the proposed approach can be used to set up a reliable numerical model.

3 The Approach of Hydraulic Travel Time Tomography

3.1 Introduction

Conventional aquifer investigation methods such as pumping tests provide integral estimates of hydraulic parameters averaged over a large volume. This kind of information is insufficient to develop groundwater models requiring detailed information about the spatial distribution of the subsurface. To circumvent this problem tomographical methods are applied. The principle of tomography was developed for medical applications, e.g. to determine the spatial distribution of X-ray attenuation over cross sections of the head or body [MERSEREAU & OPPENHEIM, 1974; SCUDDER, 1978]. The applications of geophysical methods in a tomographic array to create a three-dimensional image of the subsurface have been established since several years. It has to be noted, however, that geophysical methods such as radar tomography [DAVIS & ANNAN, 1989; HUBBARD ET AL., 1997], seismic tomography [BOIS ET AL., 1972; GELBKE, 1988] or electrical tomography [YORKEY ET AL., 1978; KOHN & VOGELIUS, 1984] yield a geophysical parameter distribution which does not have to be in accordance with hydraulic properties of the subsurface. Consequently, it is necessary to perform a complicated and ambiguous parameter transformation [DIETRICH ET AL., 1995, 1998, 1999].

As opposed to geophysical methods, hydraulic tomography allows to directly determine hydraulic subsurface properties. The procedure of hydraulic tomography consists of a series of short-term tests conducted in a tomographical array. Up to date, several researchers have evaluated hydraulic tests by using drawdown as a function of time [BOHLING, 1993; GOTTLIEB & DIETRICH, 1995; BUTLER ET AL., 1999; YEH & LIU, 2000; VESSELINOV ET AL. 2001a,b]. Another approach is based upon the inversion of travel times of pressure changes. This approach follows the procedure of seismic ray tomography. In seismic ray tomography the influence of the velocity field on the travel time between a source and a receiver are described as a line integral relating the travel time to the velocity field. According to that, VASCO ET AL. [2000] derived a line integral relating the square root of the drawdown peak arrival time of a transient pressure curve obtained for a Dirac source at the origin directly to the square root of the reciprocal value of diffusivity. The derivation of the line integral is based on an asymptotic approach described in detail by DATTA-GUPTA ET AL. [2001], VASCO ET AL. [1999], VASCO & DATTA-GUPTA [1999], DATTA-GUPTA & KING [1995], and VIRIEUX ET AL. [1994]. Diffusivity is the quotient of hydraulic conductivity to storage and is a quantitative measure for the response of a formation on hydraulic stimulation.

In this chapter, a further development of the travel time line integral is proposed. This advanced approach relates any recorded travel time corresponding to the arrival of a certain percentage of the maximum signal (e.g., 1 %, 10 %, 20 % of the maximum amplitude) to the peak time of a signal associated with a Dirac source. This relationship is derived for a Dirac source as well as for a Heaviside source. The advantage of simultaneously inverting several travel times is to exploit their different information content. As the signal propagation in a hydraulic tomographic experiment follows Fermat's principle, early arrivals characterizing the initial part of a signal, follow the fastest pathways between source and receiver. The fastest pathways are usually identical to preferential flow paths and thus, early travel times are dominated by preferential flow (if available). In contrast, late travel times, characterizing the final part of a signal, reflect integral behavior more or less, since the pressure difference between source and receiver stretches out over the complete system. Hence, it can be assumed that the different inversion results provide improved knowledge about the properties of the overall system. Additionally, the comparison of the inversion results allows the identification of potential artifacts. For the inversion a least squares based inverse procedure which has been established for several years in seismic tomography is applied.

3.2 State of the Art

The starting point of the approach is the following line integral [KULKARNI ET AL., 2000; VASCO ET AL., 2000], relates the travel time t_{peak} of the output signal to the diffusivity,

$$\sqrt{t_{peak}(x_2)} = \frac{1}{\sqrt{6}} \int_{x_1}^{x_2} \frac{ds}{\sqrt{D(s)}}$$

Eq. 3.1

where t_{peak} is the travel time of the peak of a Dirac signal from the point x_1 (source) to the observation point x_2 (receiver) and D is the diffusivity (see Figure 3.1a for a Dirac signal). In the following is given a short summary of the derivation of the proposed line integral:

The diffusion equation in a heterogenous medium in the frequency domain describes the evolution of head H in dependence of frequency ω and space x

$$\nabla^2 H(x,\omega) + \Lambda(x) \cdot \nabla H(x,\omega) - i\omega(x) H(x,\omega) = 0 \quad ,$$

Eq. 3.2

by defining

$$\Lambda(x) = \frac{\nabla k(x)}{k(x)}$$

Eq. 3.3

$$D^{-1}(x) = \Delta(x) = \frac{S(x)}{k(x)}$$

Eq. 3.4

where $S(x)$ and $k(x)$ denote the storage coefficient and the hydraulic conductivity, respectively, and $\Delta(x)$ is the inverse of the diffusivity. An asymptotic solution of Equation 3.2 is given by FATEMI ET AL., [1995],

$$H(x,\omega) = \exp\left[-\sqrt{i\omega\sigma(x)}\right] \sum_{n=0}^{\infty} \frac{A_n(x)}{\left(\sqrt{-i\omega}\right)^n} .$$

Eq. 3.5

The motivation for using an expansion in inverse powers of ω is that the initial terms of the series represent rapidly varying (high frequency, large ω) components of the solution and successive terms are associated with lower frequency behavior [VASCO and DATTA-GUPTA, 1999]. The asymptotic solution (Eq. 3.5) is the sum of an infinite number of functions A_n(x). However, only the first few terms in the series which can be related to important physical quantities are considered. In order to obtain expressions for these quantities

the sum (Eq. 3.5) is substituted into (Eq. 3.2). In this case the terms $\sqrt{-i\omega}$ and $\left(\sqrt{-i\omega}\right)^2$ are considered, leading to the following equation

$$i\omega\nabla\sigma(x)\cdot\nabla\sigma(x)A_0(x)-i\omega\Delta(x)A_0(x)=0\,.$$

Eq. 3.6

Assuming that $A_0(x)$ and ω are unequal to zero (Eq. 3.6) can be expressed as follows

$$\nabla\sigma(x)\cdot\nabla\sigma(x)-\Delta(x)=0\,.$$

Eq. 3.7

Equation 3.7 is known as the eikonal equation, describing several propagation processes e.g. wave propagation. In this case it relates the function $\sigma(x)$ to the flow properties as contained in $\Delta(x)$. A physical interpretation of $\sigma(x)$ is obtained if the zeroth-order term in expansion of Equation 3.5 is considered

$$H(x,\omega)=A_0(x)\exp\left[-\sqrt{i\omega\,\sigma\,(x)}\right].$$

Eq. 3.8

VIRIEUX ET AL., [1994] has transformed Equation 3.8 in the time domain under the assumption of a Dirac source at the origin

$$h(x,t)=A_0(x)\frac{\sigma(x)}{2\sqrt{\pi t^3}}\exp\left[-\sigma^2(x)/4t\right].$$

Eq. 3.9

The first derivative of Equation 3.9 with respect to time vanishes when $6t=\sigma^2$. Hence, the travel time of the peak arrival of a Dirac impulse is $\sigma^2(x)/6$. Therefore, $\sigma(x)$ is referred to as the pseudophase, a type of travel time. Note, that $\sigma(x)$ is associated with the propagating front of peak drawdown and does not necessarily represent a surface of equal drawdown. Equation 3.7 shows that the travel time is a function of $\Delta(x)$, the inverse of the diffusivity of the medium. The spatially varying quantity $A_0(x)$ will generally ensure that the amplitude of the peak drawdown observed at various positions will differ.

Now, it is possible to derive a line integral by defining a trajectory $s(t)$ between a source (x_1) starting at t = 0 and a receiver (x_2) using a curvilinear coordinate system. In these coordinates $\sigma(x)$ only varies with (s) and $\nabla\sigma$ is tangent to the s coordinate curve. Thus $\nabla\sigma = d\sigma/ds$ and from Eqation 3.7 it is possible to define the following

$$\frac{d\sigma}{ds}=\sqrt{\Delta(s)}$$

Eq. 3.10

Substitute $\sigma\,(x)$ with $\sqrt{t}=\dfrac{\sigma}{\sqrt{6}}$

$$\sqrt{t_{peak}(x_2)}=\frac{1}{\sqrt{6}}\int_{x_1}^{x_2}\frac{ds}{\sqrt{\Delta(s)}}\,.$$

Eq. 3.11

Equation 3.11 is a result of a high frequency assumption. It is assumed that the permeability and porosity vary smoothly with respect to the spatial wavelength of the propagation [VASCO ET AL., 2000]. The limits and possibilities of the asymptotic approach are discussed in detail in chapter 5.

3.3 Methodology

Equation 3.1 or 3.11, respectively, relates the travel time t_{peak} of the output signal to the diffusivity. For a Dirac source a transformation factor relating each travel time corresponding to a certain percentage of the peak height to t_{peak} (Figure 3.1b) is developed. The arrows in Figure 3.1b indicate that the transformation factor has to be larger than 1 if the travel time is less than t_{peak} (part I) and if the travel times are larger than t_{peak} the transformation factor has to be less than 1 (part II).

With regard to practicability, experiments are designed for a Heaviside source (Figure 3.2a). In order to avoid the differentiation of each

recorded signal a conversion factor providing a direct relationship between the travel times associated with a Dirac and a Heaviside source (Figure 3.2b) is derived (section 3.3.2).

3.3.1 Derivation of the Transformation Factor for a Dirac Source

The diffusion equation in a homogeneous medium describes the evolution of head h in dependence of time t and space r

$$S\frac{\partial h}{\partial t} = \frac{k}{r^2}\frac{\partial}{\partial r}\left(r^2\frac{\partial h}{\partial r}\right)$$

Eq. 3.12

where S denotes the storage coefficient and k the hydraulic conductivity. Spherical coordinates are used here because each injection port or slugged interval, respectively, represents a point source and the signal can be assumed to spread radially due to the opened measuring ports (see section 4.2). After HÄFNER ET AL., [1992], the solution of the diffusion equation in an infinite domain for a Dirac source is

$$h_d(r,t) = \frac{V}{\sqrt{(4\pi kt)^3/S}}\exp\left[-\frac{Sr^2}{4kt}\right]$$

Eq. 3.13

where V is the product of the flow rate Q and the input time and $h_d(r,t)$ is the hydraulic head depending on space and time. The subscript $_d$ stands for a Dirac source. The peak time of a pressure pulse can be determined by means of the first derivative of Equation 3.13

$$\frac{\partial h_d}{\partial t} = \left[-1.5\frac{V}{\sqrt{(4\pi k)^3 t^5/S}} + \frac{V}{\sqrt{(4\pi kt)^3/S}}\right] \cdot \frac{Sr^2}{4kt^2}\exp\left[-\frac{Sr^2}{4kt}\right].$$

Eq. 3.14

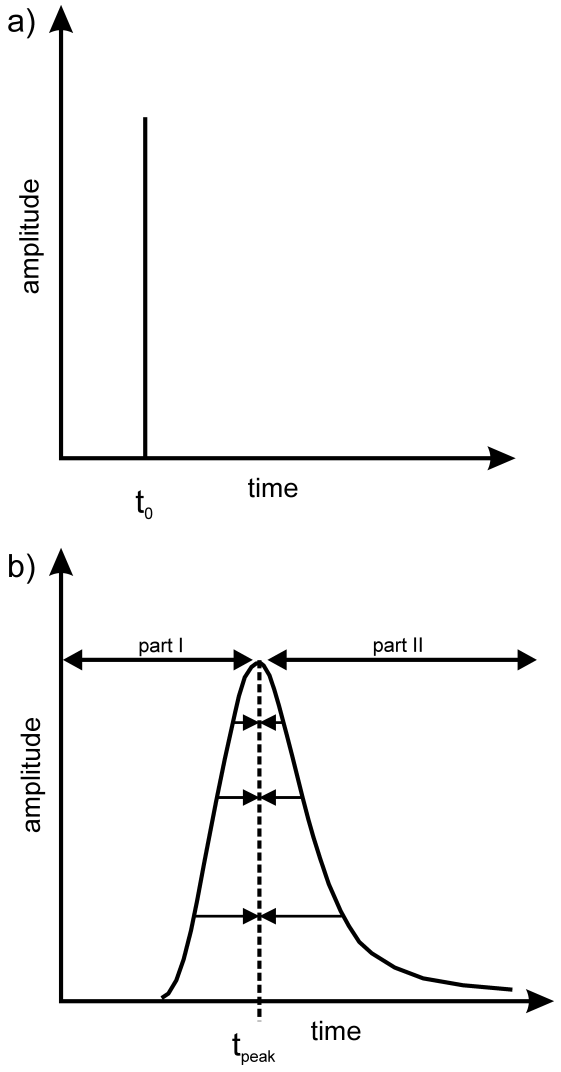

Figure 3.1 (a) Illustration of a Dirac impulse (input signal) and (b) a recorded output signal. The arrows in Figure 3.1b indicate that the transformation factor has to be larger than 1 if the travel time is less than t_{peak} (part I) and if the travel times are larger than t_{peak} the transformation factor has to be less than 1 (part II) [*BRAUCHLER ET AL., 2003a*].

The first derivative becomes zero when $t = t_{peak} = \frac{Sr^2}{6k}$. Consequently, the peak time t_{peak} can be expressed in dependence of the hydraulic properties S and k and the distance r. The amplitude of the signal can be determined by inserting t_{peak} into Equation 3.13

$$h_{peak} = h_d(r, t_{peak}) = \frac{V}{\sqrt{\left(\frac{2\pi}{3}\right)^3 Sr^3}}\exp\left[-\frac{3}{2}\right].$$

Eq. 3.15

In order to calculate the above mentioned transformation factor a head ratio α_d is introduced via

$$h_d\left(r,t_{\alpha,d}\right)=\alpha_d\ h_{peak};\qquad 0<\alpha_d\le 1. \qquad \textit{Eq. 3.16}$$

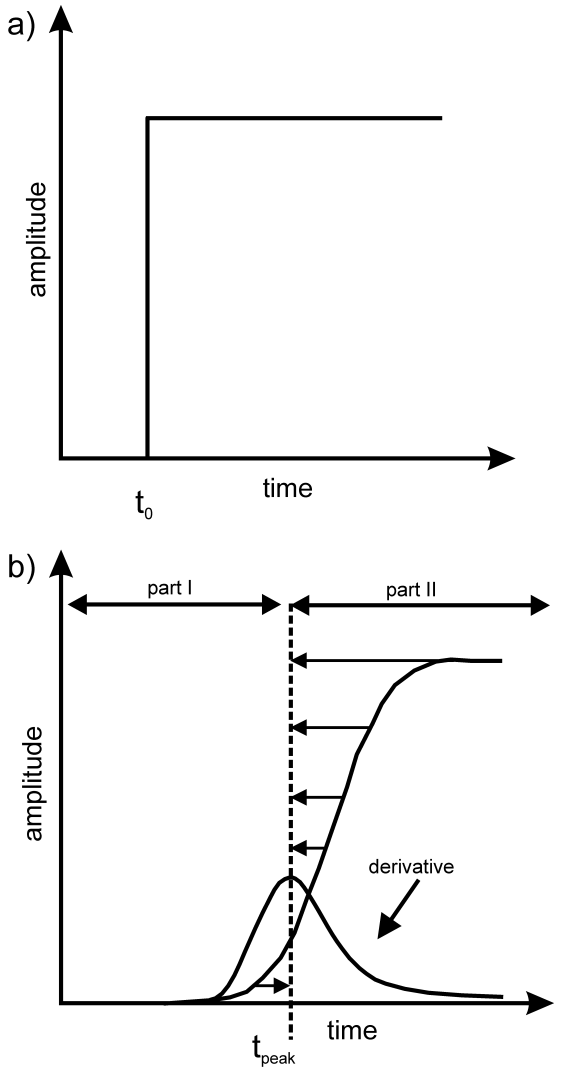

Figure 3.2 (a) Illustration of a Heaviside source (input signal) and (b) a recorded output signal. The arrows in Figure 3.2b indicate that the conversion factor has to be larger than 1 if the travel time is less than t_{peak} (part I) and less than 1 otherwise (part II). The derivative of the output signal corresponds to the output signal of a Dirac impulse [BRAUCHLER ET AL., 2003a].

The head ratio α_d enables the comparison of the peak time with the travel times when the hydraulic signal exceeds or falls below some specified percentage of the maximum amplitude h_{peak} encountered at the receiver (Figure 3.3a). Using Equations 3.13 and 3.15, the transformation factor $f_{\alpha,d}=\dfrac{t_{peak}}{t_{\alpha,d}}$ for the corresponding travel time $t_{\alpha,d}$ is given by

$$\alpha_d=\left(\frac{t_{peak}}{t_{\alpha,d}}\right)^{1.5}\exp\left[-\frac{3}{2}\left(1-\frac{t_{peak}}{t_{\alpha,d}}\right)\right]$$
$$=f_{\alpha,d}^{1.5}\exp\left[-\frac{3}{2}\left(1-f_{\alpha,d}\right)\right] \qquad \textit{Eq. 3.17}$$

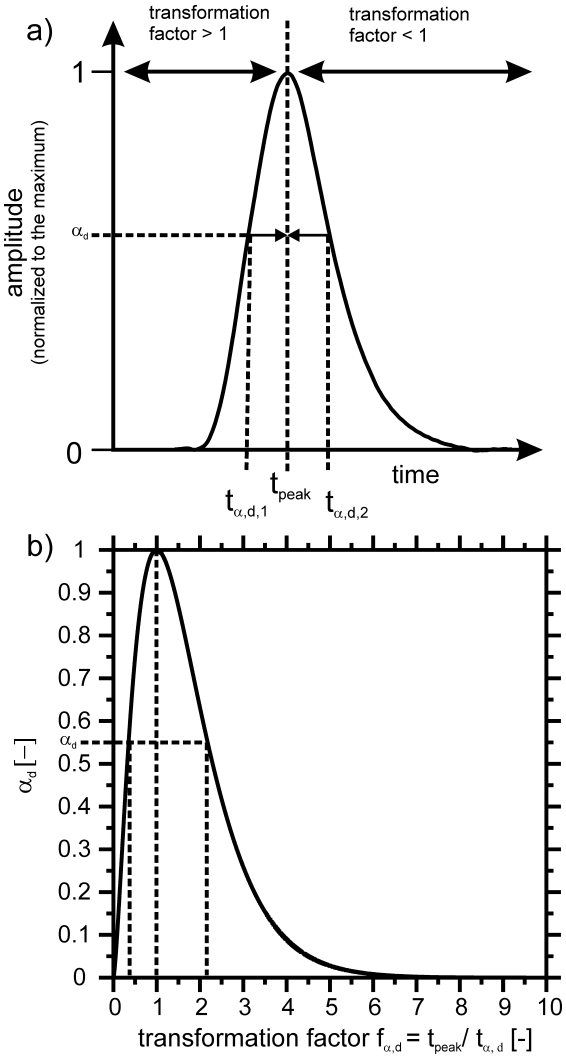

Figure 3.3 (a) Illustration of the derivation of the transformation factor for a Dirac source, relating any recorded travel time to the peak time. (b) Transformation factor for a Dirac source as function of head ratio amplitude. For the peak the transformation factor is 1 [BRAUCHLER ET AL., 2003a].

Equation 3.17 can be solved numerically for $f_{\alpha,d}$ and is plotted in Figure 3.3b. The plot shows the quotient of $\frac{t_{peak}}{t_{\alpha,d}}$, which corresponds to the transformation factor $f_{\alpha,d}$ in dependence of the head ratio α_d. Two cases must be distinguished because each head ratio amplitude is associated with two travel times $t_{\alpha,d,1}$ and $t_{\alpha,d,2}$ (Figure 3.3a). As the travel time $t_{\alpha,d,1}$ is less than the peak travel time t_{peak}, the transformation factor has to be greater than 1 and for $t_{\alpha,d,2}$ the transformation factor has to be less than 1 (Figure 3.3b). The general form of the line integral for a Dirac source can be written for $t_{\alpha,d}$ as follows

$$\sqrt{t_{\alpha,d}} = \frac{1}{\sqrt{6 f_{\alpha,d}}} \int_{x_1}^{x_2} \frac{ds}{\sqrt{D(s)}} \quad .$$

Eq. 3.18

Equation 3.18 demonstrates that it is possible to relate any recorded travel time $t_{\alpha,d}$ with the diffusivity D by using the corresponding transformation factor $f_{\alpha,d}$.

3.3.2 Derivation of the Conversion Factor for a Heaviside Source

For technical reasons a Heaviside source is easier to be put in practice, especially for the realization of an adequate signal strength needed for long distances. In order to avoid the numerical differentiation of each recorded curve a conversion factor relating Heaviside and Dirac sources is developed. The solution of the homogeneous flow equation using a Heaviside source for an infinite domain is [HÄFNER ET AL., 1992]

$$h_h(r,t) = \frac{Q}{4\pi r k} \operatorname{erfc} \frac{r}{\sqrt{4kt/S}} \,,$$

Eq. 3.19

where $\frac{Q}{4\pi r k}$ is equivalent to the maximum height h_{max} of the recorded signal. The subscript $_h$ stands for a Heaviside source. In accordance to the derivation of the transformation factor for a Dirac source a head ratio α_h is introduced in order to convert the recorded travel times of a signal from a Heaviside source at the origin into the peak time of a signal from a Dirac source (Figure 3.4a):

$$h_h\left(r, t_{\alpha,h}\right) = \alpha_h h_{\max}; \qquad 0 < \alpha_h < 1 .$$

Eq. 3.20

In accordance with section 3.3.1 $t_{peak} = \frac{Sr^2}{6k}$ is inserted in Equation 3.19. Combination with Equation 3.20 yields

$$\alpha_h = \operatorname{erfc} \sqrt{\frac{3}{2} \frac{t_{peak}}{t_{\alpha,h}}} = \operatorname{erfc} \sqrt{\frac{3}{2} f_{\alpha,h}}$$

Eq. 3.21

with the conversion factor $f_{\alpha,h} = \frac{t_{peak}}{t_{\alpha,h}}$.

Equation 3.21 is plotted in Figure 3.4b. By means of this graph the conversion factor $f_{\alpha,h}$ is determined for each travel time of a recorded signal with a Heaviside source at the origin. The conversion factor $f_{\alpha,h}$ becomes 1 when the height of the signal is approximately 8.2 % of h_{max}. This time is equivalent to the peak arrival time of a signal from a Dirac source. As expected, Figure 3.4b shows that all travel times being less than the peak time have to be multiplied by a conversion factor larger than 1. For larger travel times the conversion factor is less than 1. Therefore, it is possible to convert all travel times of a hydraulic signal from a Heaviside source to the peak time of a Dirac signal. Furthermore, this conversion does not require differentiation or integration of the recorded signal, thus it is not necessary to smooth or fit disturbed data. The line integral for a Heaviside source can be written in

accordance with Equation 3.18 by using the deduced conversion factor $f_{\alpha,h}$ as follows

$$\sqrt{t_{\alpha,d}} = \frac{1}{\sqrt{6 f_{\alpha,h}}} \int_{x_1}^{x_2} \frac{ds}{\sqrt{D(s)}} \quad .$$

Eq. 3.22

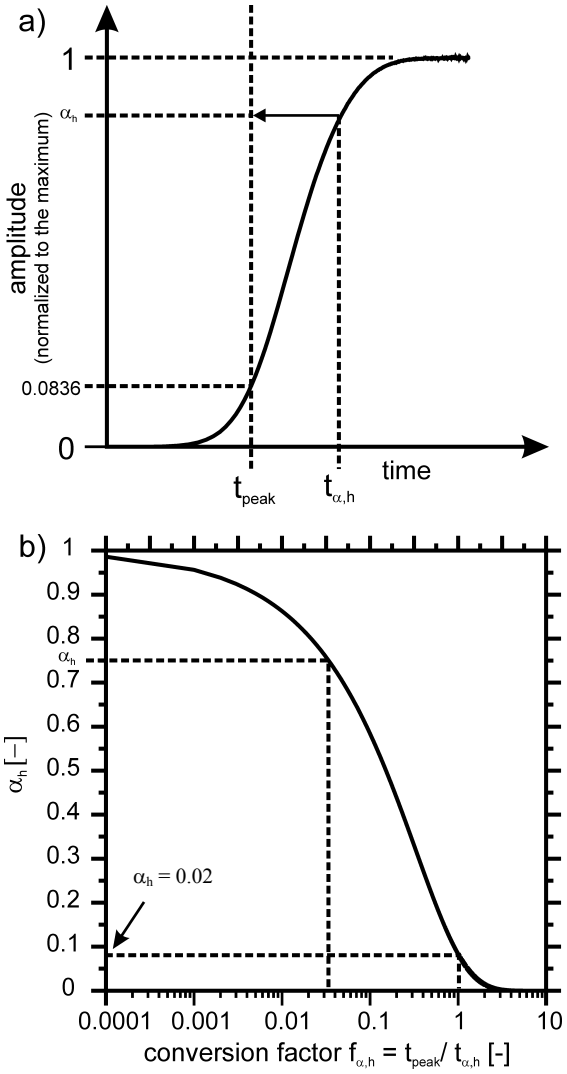

Figure 3.4 (a) Illustration of the conversion factor for a Heaviside source, relating any recorded travel time to the peak time of a Dirac source signal. (b) Conversion factor for a Heaviside source as function of head ratio amplitude. The conversion factor equals 1 when the relative amplitude of the signal is around 8.2 % of h_{max} [BRAUCHLER ET AL., 2003a].

3.4 Inversion Technique

The propagation of a seismic signal is described, similarly to the propagation of a pressure pulse, by a line integral relating the travel time t, recorded between a source and a receiver, with the spatial velocity distribution v of an investigated area:

$$t = \int_{x_1}^{x_2} \frac{ds}{v(s)}$$

Eq. 3.23

In the described approach the similarity between the Equations 3.18, 3.22, and 3.23 is utilized, enablin to use the same application software. The inversion is conducted with the commercial software package GeoTom 3D, which is based on the last Bureau of Mines tomography program 3DTOM [JACKSON & TWEETON, 1996]. The inversion program is chosen because it is developed to handle large 3-dimensional data sets on common personal computers and it allows ray tracing with either straight or curved raypaths. It uses a least square solution of a linear inverse problem. The integrals defined in Eqs. 3.18 and 3.22 can be converted to a discrete inverse problem by approximating the integral as a summation as follows

$$\sqrt{6 f_x t_i} = \sum_{j=1}^{n} \sqrt{\frac{1}{D_j}}\, d_{ij}$$

Eq. 3.24

where d_{ij} is the distance along trajectory i in voxel j and D_j is the average diffusivity within voxel j. The goal of the inversion is to choose a diffusivity distribution which minimizes the least squares between the predicted and the measured travel times. According to this, two equations can be defined

$$J = \left[\sqrt{6 f_x t_i^m} - \sqrt{6 f_x t_i^e}\right] = \sum_{j=1}^{n} (\Delta t_i)^2$$

Eq. 3.25

with t_m^i as the measured travel time, t_i^e as the estimated travel time, Δt_i as the difference of the square roots of the travel times, n as the number of measurements, f_x as the conversion and transformation factor, respectively and J describes the functional. Additionally, a minimum criterion can be defined, which allows the determination of a unique solution.

$$f\left(\Delta\sqrt{D_j^{-1}}\right) = \sum_{j=1}^{N}\left(\Delta\sqrt{D_j^{-1}}\right)^2 \rightarrow \min$$

Eq. 3.26

After DINES & LYTLE, [1979] Equation 3.26 corresponds to a minimum energy correction. Minimizing Equation 3.25 subject to Equation 3.26 leads for each trajectory to an expression for the improvement of the square root of reciprocal diffusivity $\Delta\sqrt{D_j^{-1}}$:

$$\Delta\sqrt{D_j^{-1}} = \frac{\sqrt{\Delta t_i}\, 6 f_x d_{ij}}{\sum_{j=1}^{N} d_{ij}^2}.$$

Eq. 3.27

As the incremental correction $\Delta\sqrt{D_j^{-1}}$ is accumulated for all trajectories before being applied to the voxels, the used algorithm is called SIRT, **S**imultaneous **I**terative **R**econstruction **T**echnique [GILBERT, 1972]. The propagation of a pressure pulse and seismic waves follow the same paths. Therefore, seismic ray tracing techniques can be used.

Ray tracing methods are applied in order to determine the raypaths or trajectories, respectively. Rays are defined as the normals to the wavefronts. A ray is determined if the source point, observation point (receiver) and the incident angle are fixed. Fermat's principle governs the geometry of the raypaths. This principle states (in its simplest form) that waves of a given frequency traverse the path between two points which takes the least time. Since the diffusivity distribution of geological media may vary over several orders of magnitude and consequently the travel times of a hydraulic signal also, it has to be assumed that the raypaths or trajectories are curved. For this reason the inversion presented in chapter 4 and 5 are conducted with curved ray tracing.

The inversion program GeoTom3D [JACKSON AND TWEETON, 1996] originally developed to invert seismic or radar signals, performs curved ray tracing with ray bending derived from the method of UM AND THURBER [1987], which was modified to give more reliable results for large velocity contrasts. The program tries different degrees of ray bending to find the one yielding the shortest travel time. The ray bending approach is based on repeated subdivision of an initially straight raypath into an increasing number of straight segments. Each step in the process consists of a division and an adjustment phase.

For the initial subdivision step, a straight raypath is constructed from source to receiver and the midpoint is calculated, dividing the original path into two segments. The velocity gradient is computed at the midpoint and the mipoint is displaced along the local gradient. The gradient at the new midpoint is then calculated, and the midpoint location is again adjusted. This adjustment is repeated one or more times before proceeding to the next subdivision step. In the second step, the same process is applied to each of the segments produced in the first step. At each step, the travel time along the path is calculated, and subdividing stops when a stable minimum time is attained.

Of course there are other methods of ray tracing, but a detailed discussion would go beyond the scope of this thesis and interested readers are referred to the studies by KOEHLER

AND TANER, [1985], GERSZTENKORN ET AL., [1986], WANG AND TREITEL, [1973], ANDNEKUT [1994].

3.5 Further Consideration and Discussion

The main advantage of using the hydraulic travel time approach is the possibility to invert large data sets in several minutes on a common PC. Classical inverse methodologies are known to have many difficulties, in particularly the insurmountable computational burden, when they are applied to estimate detailed hydraulic properties in three dimensional geological formation [KITANIDIS, 1997]. E.g. VESSELINOV ET AL. [2001a,b] have proposed a methodology for numerical inversion of pneumatic cross-hole tests. Thereby, they used the FEHM code (Finite Element Heat and Mass Transfer Code) from Los Alamos National Laboratory to conduct the forward model and an automatic parameter estimator (PEST, DOHERTY ET AL., [1994]). The numerical inversion required several hours to days on a supercomputer with 32 parallel processors.

However, there are several points, partly already mentioned in the previous sections, which have to be investigated in detail by applying the proposed approach:

- The derivation of the line integral is based on a high frequency assumption [VASCO ET AL., 2000]. Hence, a smooth parameter distribution of the investigated area with respect to the spatial wave length of the sourcesignal is assumed. VASCO ET AL. [2000] have mentioned that the approach is working for permeability contrasts of 1-2 orders of magnitude. In chapter 5 the effects of abrupt contrasts in permeability are discussed.
- Next the validity and the advantages of the derived transformation and conversion factor have to be investigated. Thereby, the influence of the different travel times on the results of the inversion is of particular importance.
- The last point is to evaluate the suitability of the inversion technique itself. It has to be mentioned, that the employed inversion software, was originally developed for seismic and radar data. Usually, in seismic or radar tomography the velocity contrasts are approximately 30% in comparison to several orders of magnitude differences in hydraulic tomography.

4 Application of the Hydraulic Travel Time Approach to Laboratory Experiments

4.1 Introduction

The procedure introduced in chapter 3 is applied to data from a set of pneumatic short term tests conducted to a gas saturated fractured sandstone cylinder. For the purpose of reducing the duration of the experiments pneumatic instead of hydraulic short term tests were performed. The experimental set-up is designed to produce a trajectory pattern (section 3.4) covering the complete cylinder, whereby the source can be considered as a point source. The produced trajectory patterns can be compared to the ray patterns of geophysical cross-hole tomography experiments. These recorded data make it possible to reconstruct a three-dimensional image of the diffusivity distribution of the cylinder and to verify the results by geological surface mapping. In this chapter the terminology hydraulic instead of pneumatic tomography is used because the practical application of this method is the high resolution characterization of aquifers.

Additionally, the method of staggered grids is applied in order to improve the nominal resolution. The inversion results depend on the spatial position of the grid because the hydraulic properties are averaged over one voxel. On account of this, it could be that little inhomogeneities may not be resolved because of the average effect within one voxel. Practically it is not possible to refine the grid so far that the averaging effects can be neglected because, one model parameter has to be determined for each voxel. Thus, the number of performed short-term tests is the upper limit for the model parameters we can safely invert [MENKE, 1984]. To circumvent this problem without using any a priori information the method of staggered grids is used, which VESNAVER & BÖHM [2000] proposed for the inversion of seismic tomographic data. Especially, for hydraulic travel time tomography the method of staggered grids is of great interest, because the time exposure for the data acquisition is much higher in comparison to geophysical methods. By the method of staggered grids, the initial grid is displaced in several ways by a known distance. For each grid a slightly different image of the parameter distribution is received because inside each voxel a different averaged value is determined. Finally, the arithmetic mean of the parameter distribution of all grids is calculated by staggering them. This leads to a refining of the grid and to a better resolved image without conducting additional measurements or using a priori information.

4.2 Data Acquisition

The presented methodology is applied to data from a set of crosswell pneumatic tests conducted in a gas saturated sandstone cylinder

with a height of 34 cm and a diameter of 31 cm. For the recovery of the cylinder a Stubensandstein formation was chosen which is quarried in the southern part of Germany. This formation is part of a continental alluvial depositional system [HORNUNG & AIGNER, 1999] and is mainly composed of arkose sandstone. The sample was situated in a bed load channel dominated facies. The sandstone cylinder was chosen out of a series of similar samples because of its simple structural composition exhibiting a single fracture embedded in a more or less homogeneous matrix.

a)

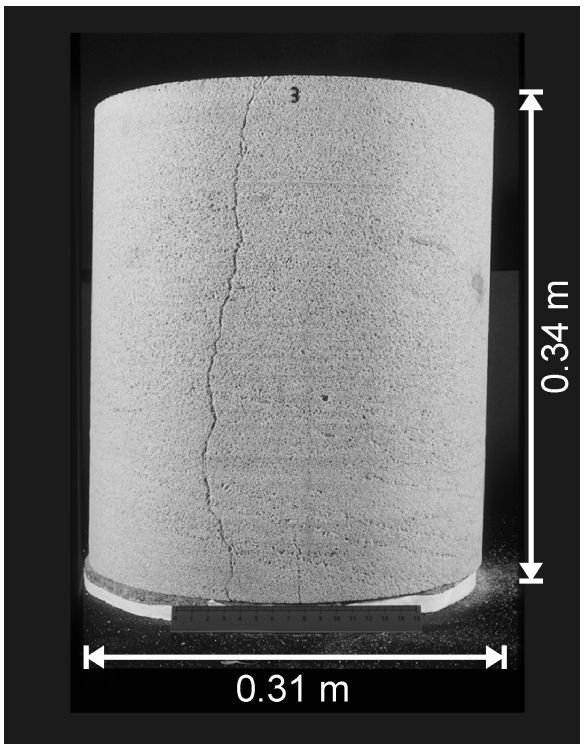

b)

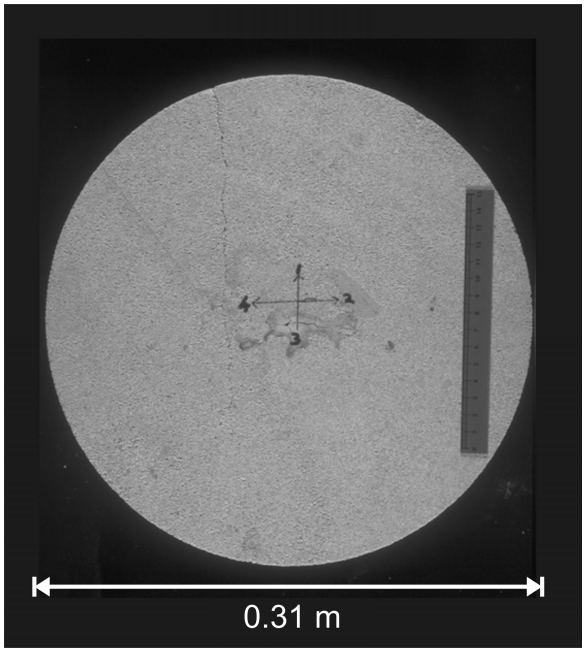

Figure 4.1 Photographs of the investigated gas saturated fractured sandstone cylinder prior to the preparation for the experiments. (a) Side view [BRAUCHLER ET AL., 2003a]. (b) Top view.

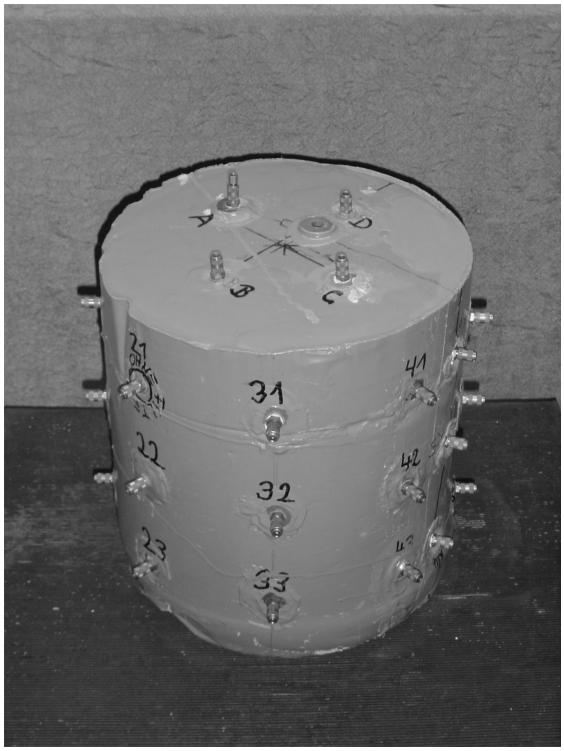

Figure 4.2 Photograph of the investigated gas saturated fractured sandstone cylinder after the preparation for the experiments.

Figures 4.1 and 4.2 show the investigated gas saturated fractured sandstone cylinder prior to and after the preparation for the experiments. The potential position of the fracture was mapped and is illustrated in Figure 4.3. The porosity is approximately 8 % and the fracture aperture ranges from 0.1 mm to 0.3 mm. The preparation of the sandstone cylinder is conducted similarly to the preparation of the cubic sandstone block, described in section

2.2.1. Altogether 32 injection (source) and measuring (receiver) ports, respectively, attached in a regular grid onto the cylinder. In order to obtain a huge amount of experiments in a short time pneumatic instead of hydraulic tests are conducted. For the pneumatic experiments a fully automated multi-purpose-measuring device with online data acquisition was developed [LEVEN, 2002].

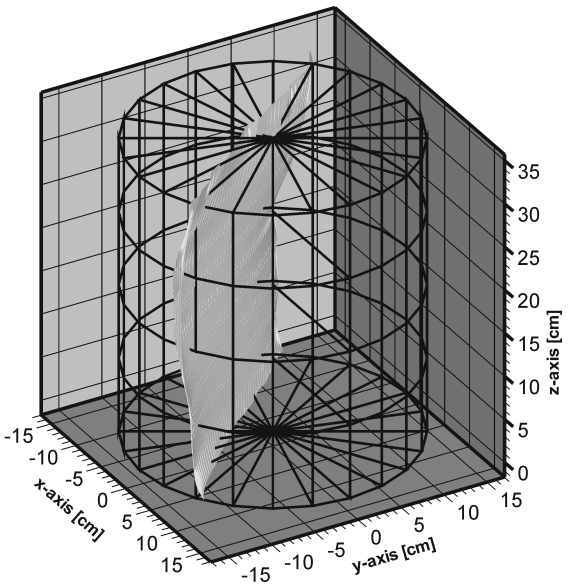

Figure 4.3 Potential position of the mapped fracture [BRAUCHLER ET AL., 2003a].

The experimental set-up is shown in Figure 4.4. At the injection port, which can be described as a point source, a Heaviside signal is applied. Thereby, compressed air is injected into the gas saturated sandstone block and the flow rate is recorded at the measuring port. All other ports are opened allowing the release of the injected air. The flow rate is recorded until a stationary flow field is established between the injection and the measuring port. It takes about 20 seconds to reach steady-state conditions. The pressure difference between the injection port and the measuring port is kept constant during the experiment by applying 0.5 bar at the injection port. In Figure 4.5 all 487 measured port-port-connections are indicated by white lines. Due to the experimental set-up (infinitesimal distance between inside and outside of the cylinder) the pressure gradient is proportional to the absolute value of pressure. Consequently, not only the gradient of the pressure but also the pressure itself is proportional to the flow rate. For this reason it is possible to use the travel times of a pressure curve as well as the travel times of a flow rate curve for the inversion.

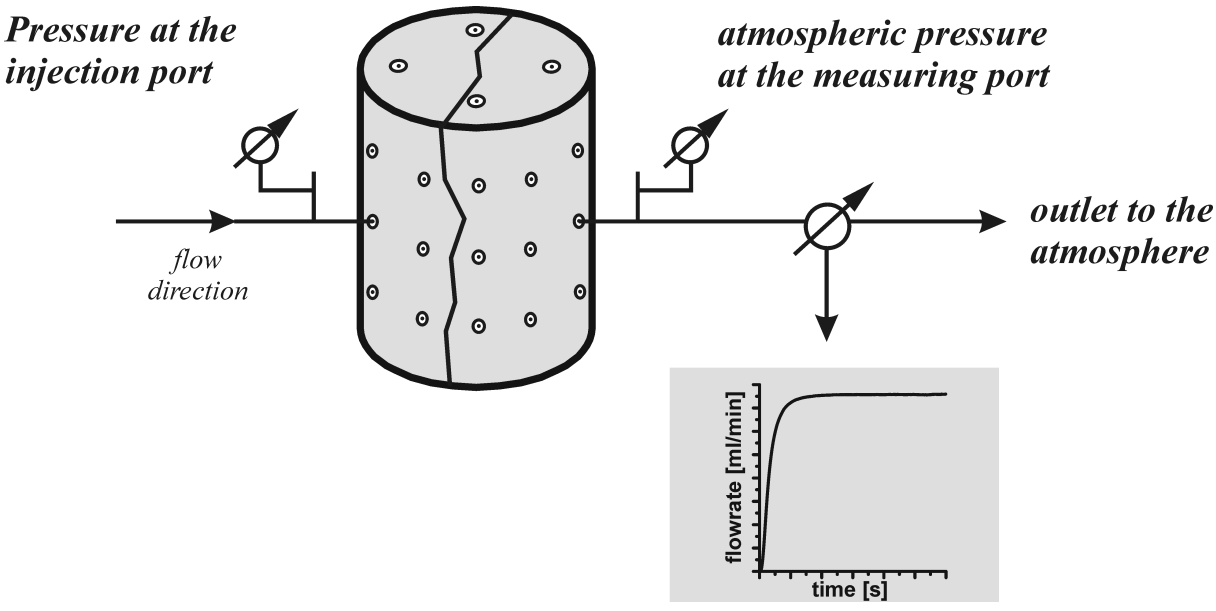

Figure 4.4 Experimental set-up after LEVEN [2002]; [BRAUCHLER ET AL., 2003a].

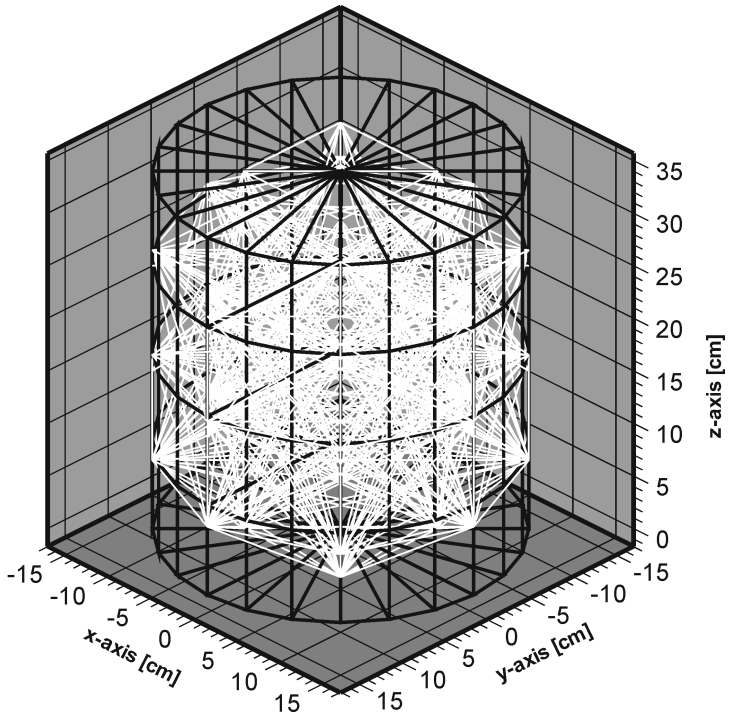

Figure 4.5 Port-port connections (white lines) [BRAUCHLER ET AL., 2003a].

With regard to practical applications the impact of two effects on travel times was investigated. First, it was found that compressibility can be neglected in our approach due to the modest pressure difference of 0.5 bar which is applied in the proposed setup. Transferring results from JARITZ [1998] compressibility effects will alter travel times by less than 10 % for the applied pressure difference. In addition, compressibility plays an even less important role in practical applications when experiments are conducted with water instead of gas.

The second effect to be investigated is the relationship between pressure difference and hydraulic conductivity. As the latter often varies over several orders of magnitudes in natural systems, it is useful to adjust the pressure difference in order to generate a signal with adequate strength. The influence of the outflow signal strength was estimated by conducting several measurements with 0.3 and 0.5 bar pressure differences. The recorded curves were normalized to the maximum value of the flow rate (Figure 4.6a, b). The comparison of the normalized curves shows no evident differences among each other. For a better comparison of the curves the travel times are plotted when 1 %, 2 %, 5 %, 10 %, 20 %, 30 % and 40 % of the maximum is reached (Figure 4.6c). The plotted travel times can be fitted perfectly with a 45° line through the origin. This result shows the travel time to be independent of the signal strength. With decreasing pressure difference the part of the recorded curves reflecting the steady-state condition becomes more diffuse (Figure 4.6a). This effect is due to the sensitivity of the measurement device, as the absolute value of the flow rate decreases with the pressure difference. For this reason the measurements

have been conducted with a pressure difference of 0.5 bar.

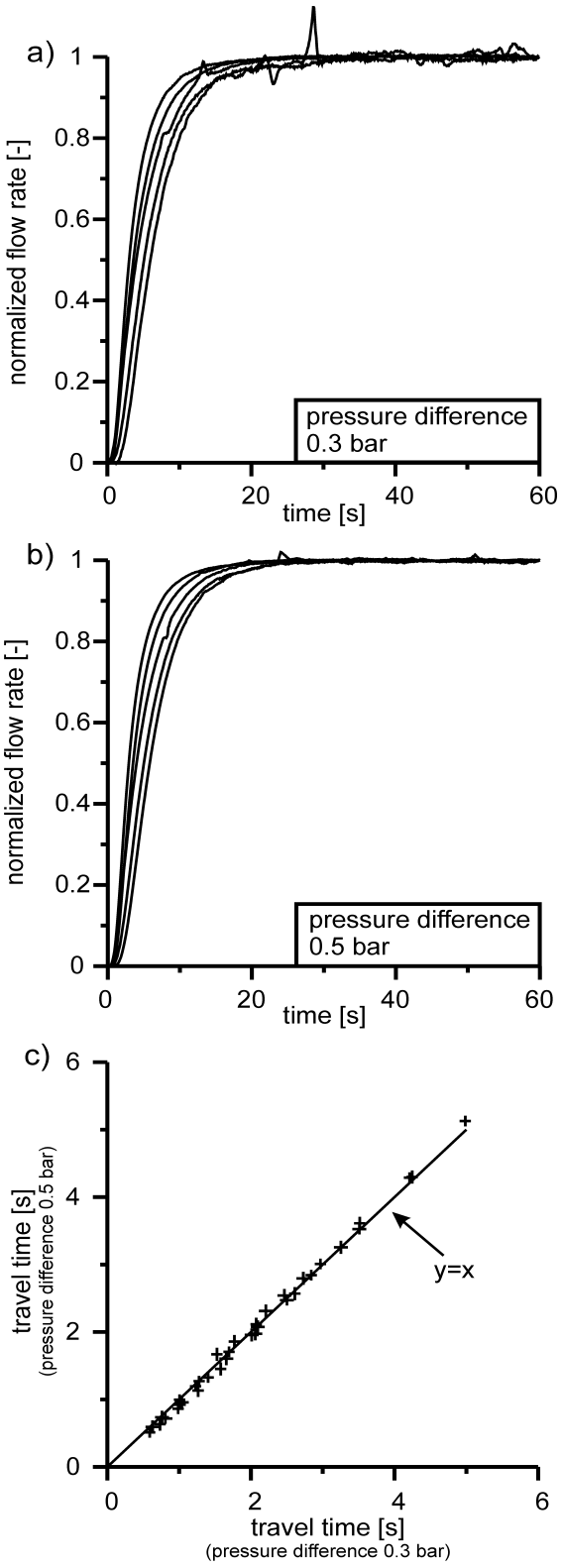

Figure 4.6 Comparison of selected experiments conducted with different pressure differences. The recorded curves are normalized to the maximum value of the flow rate. In Figure 4.6c the travel times are plotted when 1%, 2%, 5%, 10%, 20%, 30%, and 40% of the maximum flow rate is reached [BRAUCHLER ET AL., 2003a].

4.3 Discretization and Inversion

The simplest linear inverse problem is an "Even-Determined Problem". In even-determined problems there is just sufficient information to uniquely determine the model parameters. This unique solution has zero prediction error [MENKE, 1989]. Thus, the goal of the discretization is to adapt the number of cells or voxels to the number of measurements. In practice this can not be achieved because the trajectory density depends on the spatial distribution of the sources and receivers and the parameter distribution itself. Consequently, the trajectory density is varied from voxel to voxel. Thus, a "Mixed-Determined Problem" where the imperfect angular coverage of the trajectories might lead to a mathematically non-unique solution has to be solved [MENKE, 1984; JACKSON & TWEETON, 1994]. Resulting reconstructed parameter distributions might be characterized by smearing and ambiguity. In order to minimize these effects of the space dependent trajectory density the investigation area is confined to the central part of the cylindrical sample shown in Figure 4.7 and Figure 4.9 (z_{min} = 6 cm, z_{max} = 27 cm) because the angular aperture covering the top and bottom is limited. The variations in trajectory density are least in the central part. The central part is discretized by 500 voxels, 10 in *x*-direction, 10 in *y*-direction and 5 in *z*-direction (Figure 4.7). A higher number of voxels in *x*- and *y*-direction is chosen expecting larger lateral changes than vertical changes because of the position of the fracture being assumed to be nearly parallel to the axis of the cylinder.

Furthermore, the results of the tomographic investigation depends on the spatial position of the grid. The geological properties are averaged over one voxel. Thus, it is possible that important properties are positioned on the border between voxels and so the anomaly is separated into two or more voxels. This can lead to an apparent dilution of the anomaly.

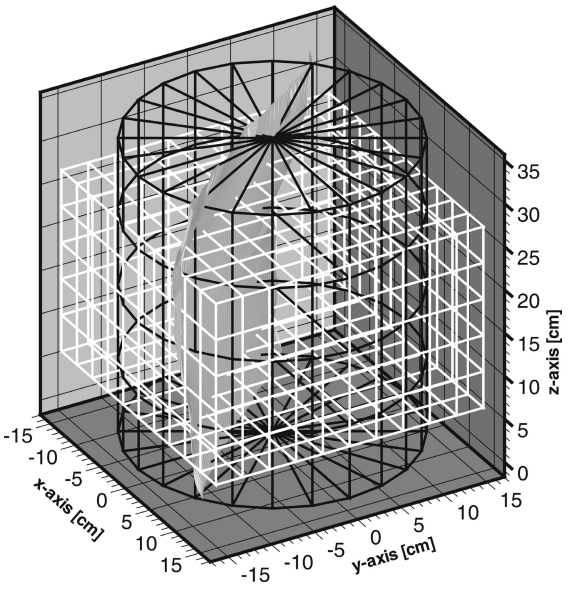

Figure 4.7 Initial discretization of the cylinder.

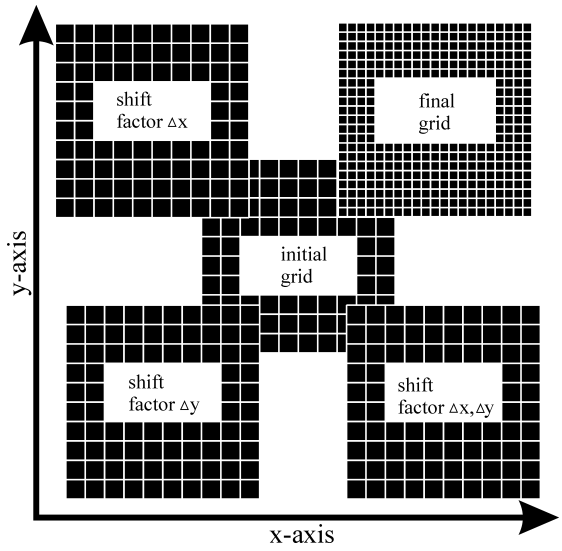

Figure 4.8 Two-dimensional sketch of the displacement of the initial grid. The shifts Δx and Δy are the half of the voxel length in x and y direction, respectively [BRAUCHLER ET AL., 2003a].

In order to avoid such dilution effects by an unlucky choice of the grid position the method of staggered grids VESNAVER & BÖHM, [2000] is applied for seismic tomography. This method is based on different viewpoints realized by shifting the grid. Such a displacement of the initial grid is performed three times in two directions (Figure 4.8). The displacements Δx and Δy are half of the voxel length in *x*- and *y*-direction, respectively. For each grid position a slightly different image of the cylinder is received because inside each voxel, over a different volume, is averaged. Each travel time is inverted four times and afterwards the arithmetic average of all grids is determined by staggering them. As a result, the final grid is composed of 2000 voxels, 20 in *x*-direction, 20 in *y*-direction and 5 in *z*-direction (Figure 4.9). This leads to a more complex image with a higher nominal resolution [VESNAVER & BÖHM, 2000]. Another possibility to overcome the problem of averaging and dilution effects would have been to directly invert a more refined model, but in this case a larger number of measurements would have been required, because the number of voxels, for which inversion can be done reliably, is limited by the number of measurements.

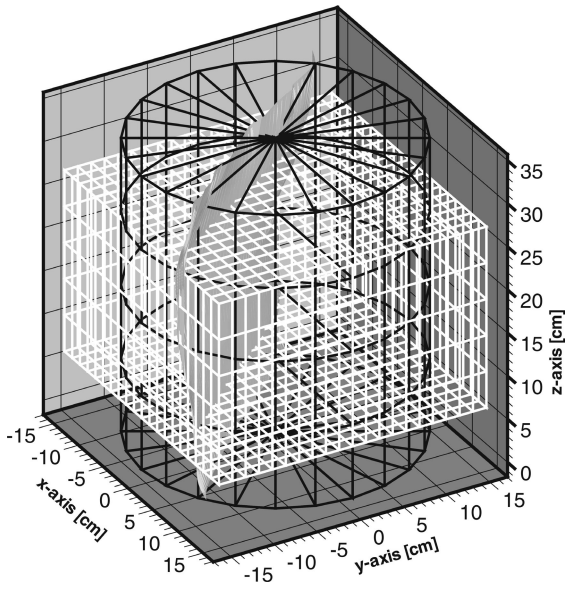

Figure 4.9 Final discretization of the cylinder after applying the methods of staggered grids.

The inversion is conducted with the commercial software package GeoTom3D [JACKSON AND TWEETON, 1996]. A detailed explanation of this software and the inversion technique itself is given in section 3.4. In

Figure 4.10 the overall residual $\sqrt{\sum\left(\sqrt{t_i^m 6 f_x} - \sqrt{t_i^e 6 f_x}\right)^2}$ is shown for 10 iteration steps of the image discussed in section 4.4 (Figure 4.12). The residual decreases in a quasi exponential manner as iterations proceed and the values are nearly constant after 10 iteration steps, whereby the initial fit to the measured data is based on a uniform preliminary model. In this example the value of $\sum\sqrt{t_i^m}$ is 1396.26 $s^{0.5}$. The comparison between $\sum\sqrt{t_i^m}$ and residual of the tenth iteration step (0.82 $s^{0.5}$) indicates that ten iteration steps reduce the discrepancy to a very small value. A larger number of iteration steps lead to small fluctuations. On this account the inversion results proposed in section 4.4 are conducted with ten iteration steps. The inversion takes around 110 seconds on a 1 GHz Pentium CPU.

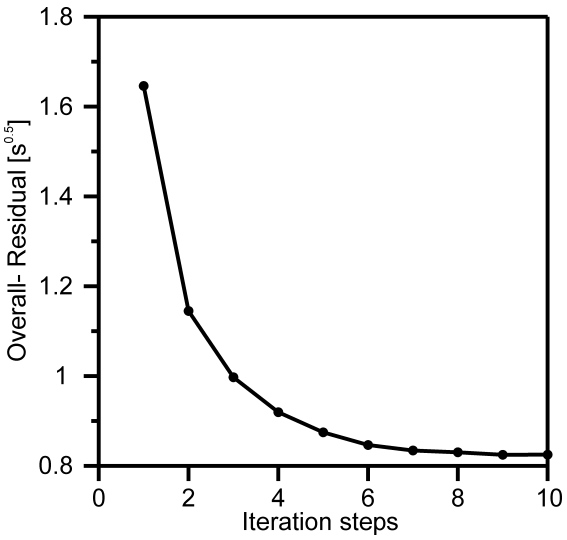

Figure 4.10 Overall Residual for 10 Iteration steps of the imaged discussed in section 4.4.2 (Figure 4.12) [BRAUCHLER ET AL., 2003a].

4.4 Results

In this section the inversion results are presented showing the three-dimensional reconstruction of the diffusivity field of the investigated sandstone cylinder. The cylinder is characterized by a fracture ranging from top to bottom. The fracture is embedded in a more or less homogeneous matrix and it can be assumed that in this setting pronounced preferential flow may be observed. First, the results obtained by using the method of staggered grids are discussed. Next, the inversion results based on different travel times are interpreted by comparing them among each other.

4.4.1 Staggered Grids

Figure 4.11 compares the inversion results for a staggered and four conventional horizontal grids at a selected slice (z = 11.3 cm). For staggering, the initial grid was displaced three times in x- and y-direction by half of the voxel length. The inversion was conducted using the travel times when 8.2 percent of the maximum flow rate was recorded at the receiver port. This travel time was chosen because it is equivalent to the peak time of a Dirac source (section 3.3.2). All inversion results show that significant variations in diffusivity are present whereby the largest diffusivity values coincide perfectly with the potential position of the fracture marked by a black line. The diffusivity distribution agrees with the well known fact that fractures usually have larger diffusivity values due to their higher conductivity and lower ability of storage. The comparison of the different slices in Figure 4.11 indicates that the method of staggered grids may lead to an improvement in resolution.

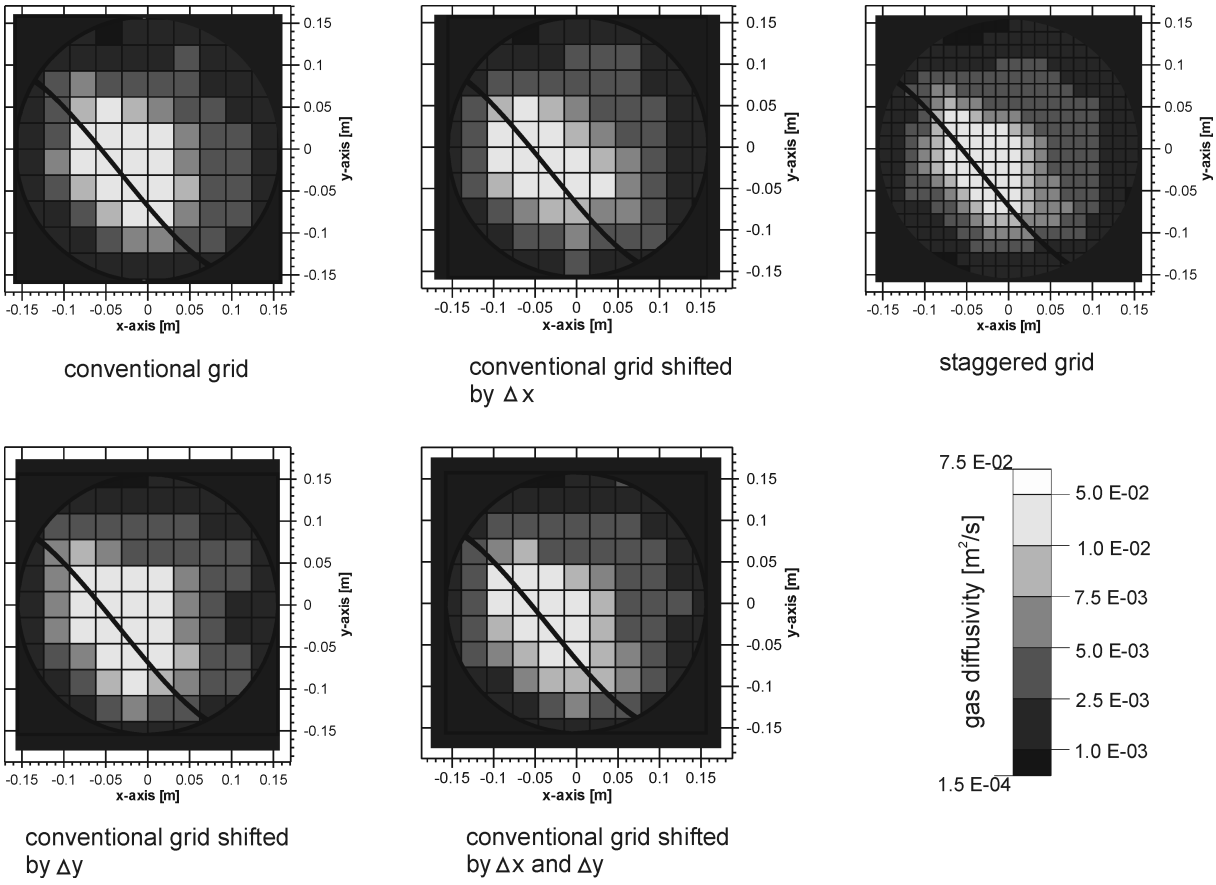

Figure 4.11 Inversion results for the travel time associated with 8.2 % of the maximum flow rate. Comparison of the inversion results of a horizontal slice at z = 11.3 cm by using a staggered and four conventional grids [BRAUCHLER ET AL., 2003a]. See color version of this figure in the Appendix (Fig. A-1).

The diffusivity pattern of the staggered grid is arranged systematically around the potential position of the fracture, while the diffusivity patterns of the conventional grids appear to be more random. The more systematic array of the staggered grid leads to a more precise, reliable and undisturbed image with reduced smearing effects. The random distribution of the yellow and red voxels of the conventional grids hamper the geological interpretation and reliability of the diffusivity distribution.

4.4.2 Inversion Results Based on Different Travel Times

The advantage of inverting more than one value of the recorded signals is the possibility to verify and evaluate the reliability of the reconstructed parameter field by comparing them among each other. Thus, it is possible to detect potential artifacts and to estimate the reliability of the anomalies. In order to illustrate the processing three inversion results are imaged (Figures 4.12, 4.13 and 4.14) based on travel times when 8.2 %, 1 %, and 40 % of the maximum flow rate was recorded. The travel times, when 1 % and 40 % of the maximum were recorded, are chosen to demonstrate the different information content of early and late travel times. The 1 % mark equals the initial increase of the recorded signal which just can be determined reliably. Hence, it can be ensured that the inversion based on the first arrivals are mainly dominated by preferential flow paths. It has to

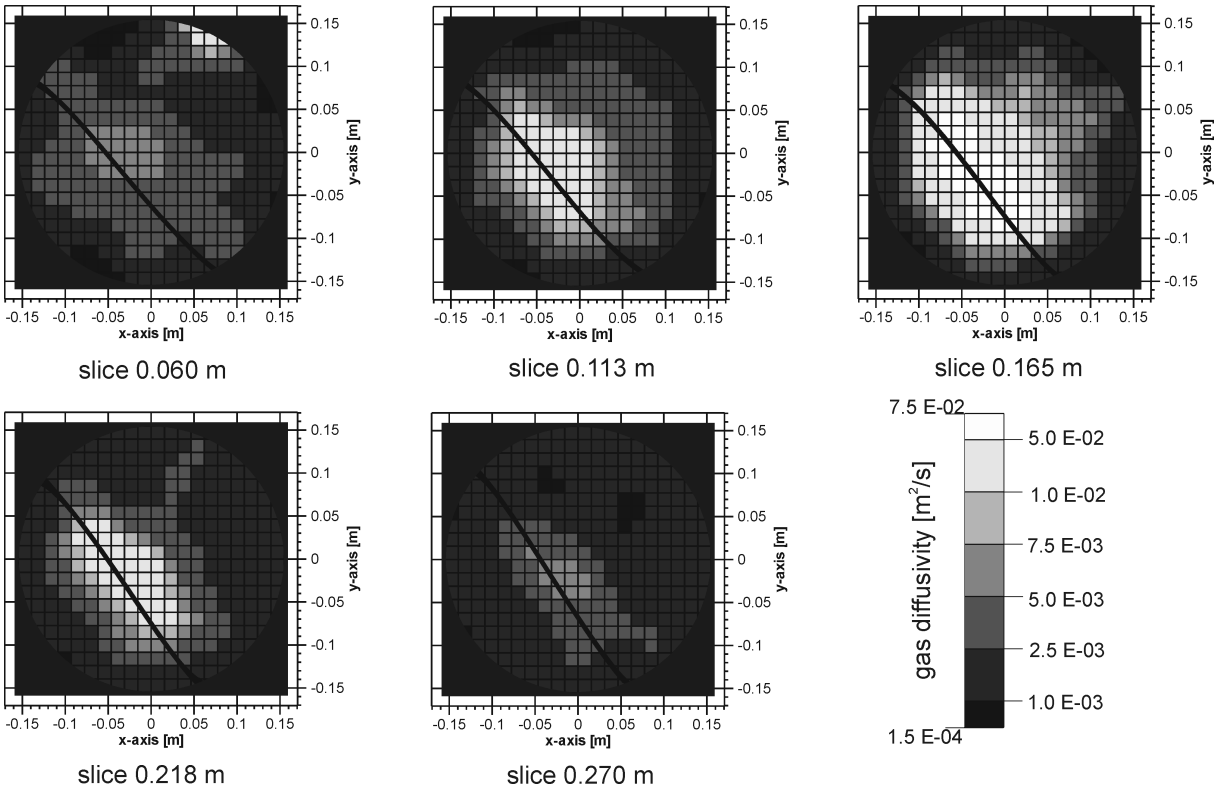

Figure 4.12 Inversion results for the travel time associated with 8.2 % of the maximum flow rate, using the method of staggered grids [BRAUCHLER ET AL., 2003,a]. See color version of this figure in the Appendix (Fig A-2).

be noted, that usually under field conditions later travel times have to be chosen since the recorded signals are more influenced by noise.

It is possible to image the different inversion results with the same scale although the travel times differ by more than one order of magnitude. This result points out the reliability of the developed method. All inversion results exhibit a high diffusivity feature crossing the complete sandstone cylinder. The spatial position and the shape of this zone agree with the location of the mapped fracture. In the slice taken at z = 0.218 m of Figure 4.12 an anomaly is imaged which could be interpreted as a small fracture connected with the main fracture under an angle of 45 degrees. This anomaly, however, cannot be recognized in Figure 4.13. Hence, it is assumed that the described anomaly is an artifact or at least has to be interpreted carefully. In this way, the reliability of each anomaly can be verified.

As the inversion results depend on the chosen travel time it can be assumed that each travel time is dominated by different components (matrix, fracture) of the investigated system. By the comparison of several inversion results the interpretation and verification becomes more comprehensive as the tomograms reflect the same investigated system but different details of it. The inversion using the travel time when 1 % of the maximum flow rate is reached shows the best agreement between the high diffusivity zone and the mapped fracture of all inversions. This result agrees with the expectations that the first arrivals of a signal are dominated by preferential flow paths. In Figure 4.13 the influence of the matrix is much stronger in comparison to the other two

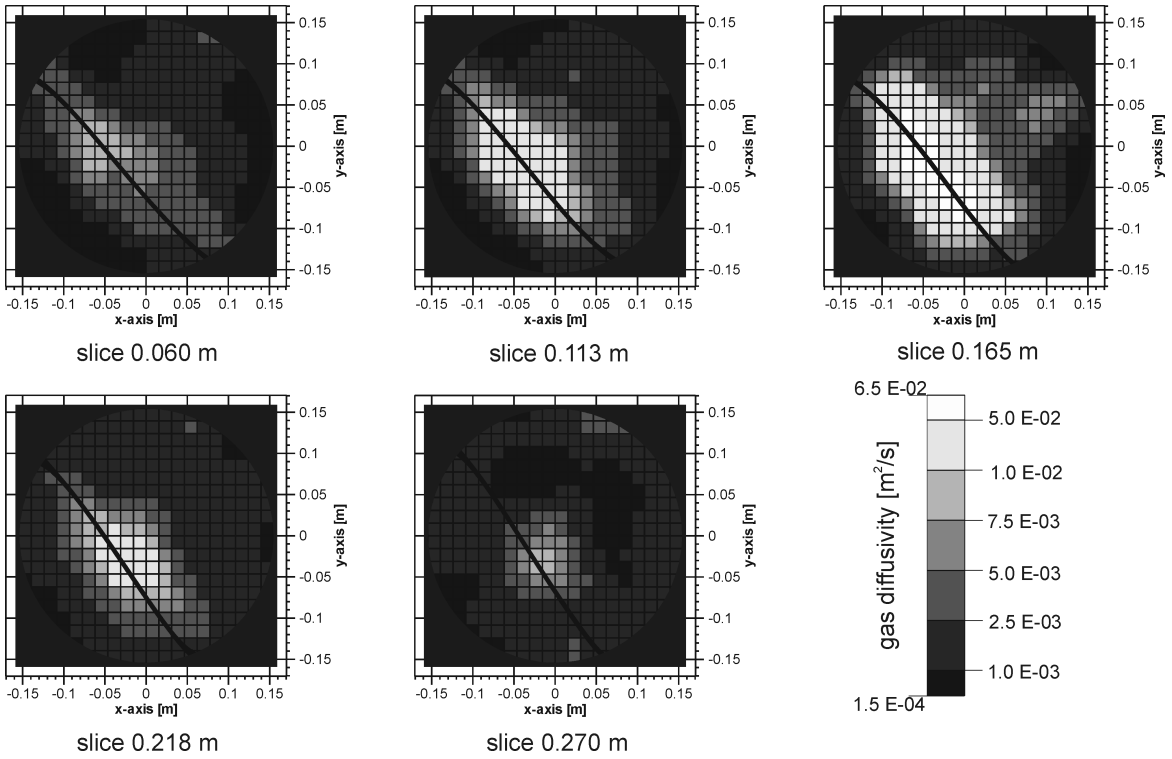

Figure 4.13 Inversion results for the travel time associated with 1 % of the maximum flow rate, using the method of staggered grids [BRAUCHLER ET AL., 2003,a]. See color version of this figure in the Appendix (Fig. A-3).

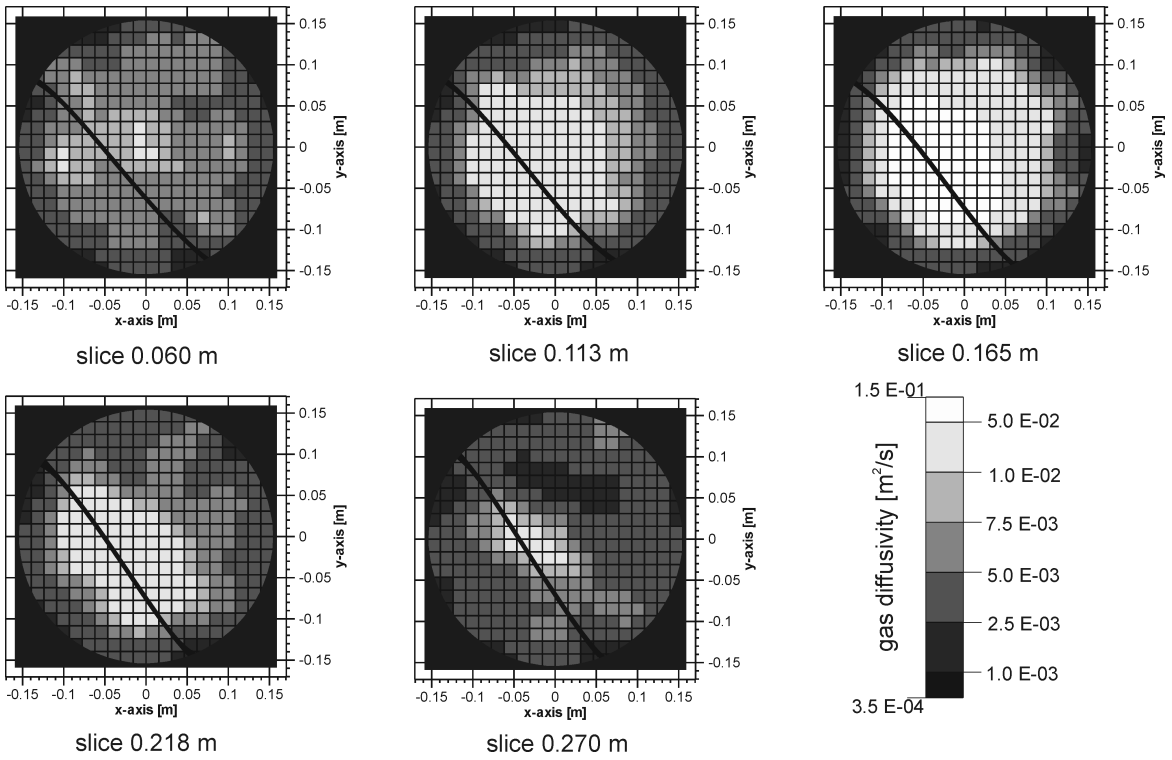

Figure 4.14 Inversion results for the travel time associated with 40 % of the maximum flow rate, using the method of staggered grids [BRAUCHLER ET AL., 2003,a]. See color version of this figure in the Appendix (Fig A-4).

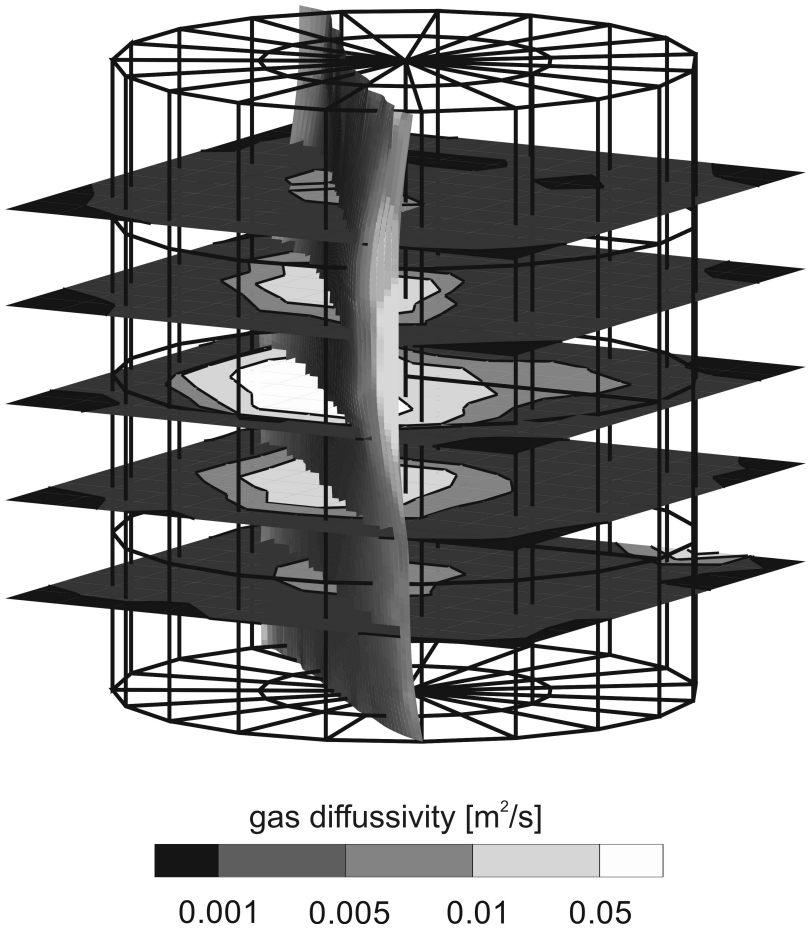

Figure 4.15 Illustration of the three-dimensional diffusivity distribution using the travel time for inversion associated with 8.2 % of the maximum of the flow rate [BRAUCHLER ET AL., 2003b].

inversions and consequently the high diffusivity zone features more smearing effects. By comparing the slice at z = 0.270 m of the three inversions it is remarkable that the high diffusivity zone is imaged much better in Figures 4.12 and 4.14. An explanation might be that the mapped fracture is partly filled and thus the later travel times are more capable to reconstruct this part of the fracture. In Figure 4.15 the five slices imaged in Figure 4.12 are arranged three-dimensionally. The Figure shows again that the highest diffusivity values coincide with the potential position of the fracture.

4.5 Summary and Conclusions

The inversion approach proposed in chapter 3 was applied to data from a set of crosswell pressure tests (487 measurements) conducted to a gas saturated fractured sandstone cylinder. Three different inversions were performed in order to reconstruct the three-dimensional diffusivity distribution. Although the travel times used for the inversions differ by more than one order of magnitude it is possible to use the same scale for imaging the diffusivity tomograms. This indicates that the derived conversion factor is working well also for strongly heterogeneous media, although the derivation was done for homogenous assumption. The interpretation of the three-

dimensional diffusivity distribution is shown to become more comprehensive as the tomograms adapted from the inversions of different travel times reveal different details of the same investigated system. The inversions based on early travel times are mainly related to preferential flow features while the inversions based on late travel times reflect an integral behavior. The very good agreement between the reconstructed diffusivity distribution and the potential position of the fracture shows obviously that it is possible to use algorithms for the inversion of hydraulic signals, which were originally developed for seismic travel time tomography. The used algorithm can handle the much higher travel time contrasts of hydraulic signals by the inversion without becoming unstable. Furthermore it is possible to invert the proposed data set in 110 seconds on a 1 GHz Pentium CPU. Beyond this, the method of staggered grids is applied. Thereby, the grid is shifted three times and afterwards the three realizations are staggered in order to obtain more precise images with reduced dilution and smearing effects. The images are found to be highly reliable and robust. It is planned to transfer the proposed approach to the field as it can be applied without any restrictions to real aquifers keeping in mind that pneumatic and hydraulic short-term tests are based on the same flow equations.

5 Application of the Hydraulic Travel Time Approach to Synthetic Data Sets

5.1 Introduction

The main focus of this chapter is to evaluate the efficiency of hydraulic travel time tomography. Therefore, a detailed systematic study of an inversion based on several travel times characterizing the recorded transient pressure pulse is presented. The data base comprises simulation results of multi-level slug tests conducted in a tomographical array between two boreholes. The forward modeling is conducted with the Finite Element Heat and Mass Transfer Code (FEHM) from Los Alamos National Laboratory. The goal of the investigations is to determine the information content of the inversion results based on different travel times and the information content of particular travel times, respectively.

The comparison of the inversion results, based on different travel times, with the forward model allows the verification and appraisal of the quality of the inversion. Hence, it is possible to determine which travel time is most suited to reconstruct a certain subsurface structure. This allows to adapt the inversion strategy to available a priori information of the investigated area. In order to objectively conduct an appraisal of the reconstructed permeability distributions, travel time contour plots derived from the forward model and trajectories derived from the inversion are used.

Beyond this, the influence of the wellbore storage on the travel times is investigated. In order to determine and reduce the influence of the wellbore storage a conversion factor is derived. The reconstruction results are found to be highly reliable and robust and the received insights allow to appraise the information content of the inversion results based on different travel times.

5.2 Methodology

In the following, a brief description of the conducted forward modeling is given. A detailed description of the used forward model technique would go beyond the scope of this thesis and interested readers are referred to the given references. The inversion of the synthetic data sets is conducted with the same technique as described in chapter 3.

5.2.1 Forward Modeling

In this work the mesh generator LaGrit (Unstructured Finite Element Grid Generation for Geological Applications) [GABLE ET AL., 1996; TREASE ET AL., 1996] a software tool from Los Alamos National Laboratory for generating, editing and optimizing multi-material unstructured finite element grids, is used. For the numerical simulation the FEHM-Finite Element Heat and Mass Transfer Code [ZYVOLOSKI ET AL., 1995], is chosen which

was also developed by the Los Alamos National Laboratory.

Figures 5.1 and 5.2 show the concept and design for the partially penetrating slug tests. The thickness of the aquifer is 60 m and the length is 200 m, whereby the slugged borehole is located in the centre of the model domain. The length of the injection interval is 0.5 m. The chosen value of 0.5 m is a compromise between the point source requirement of the inverse model and practical requirements for implementation under field conditions.

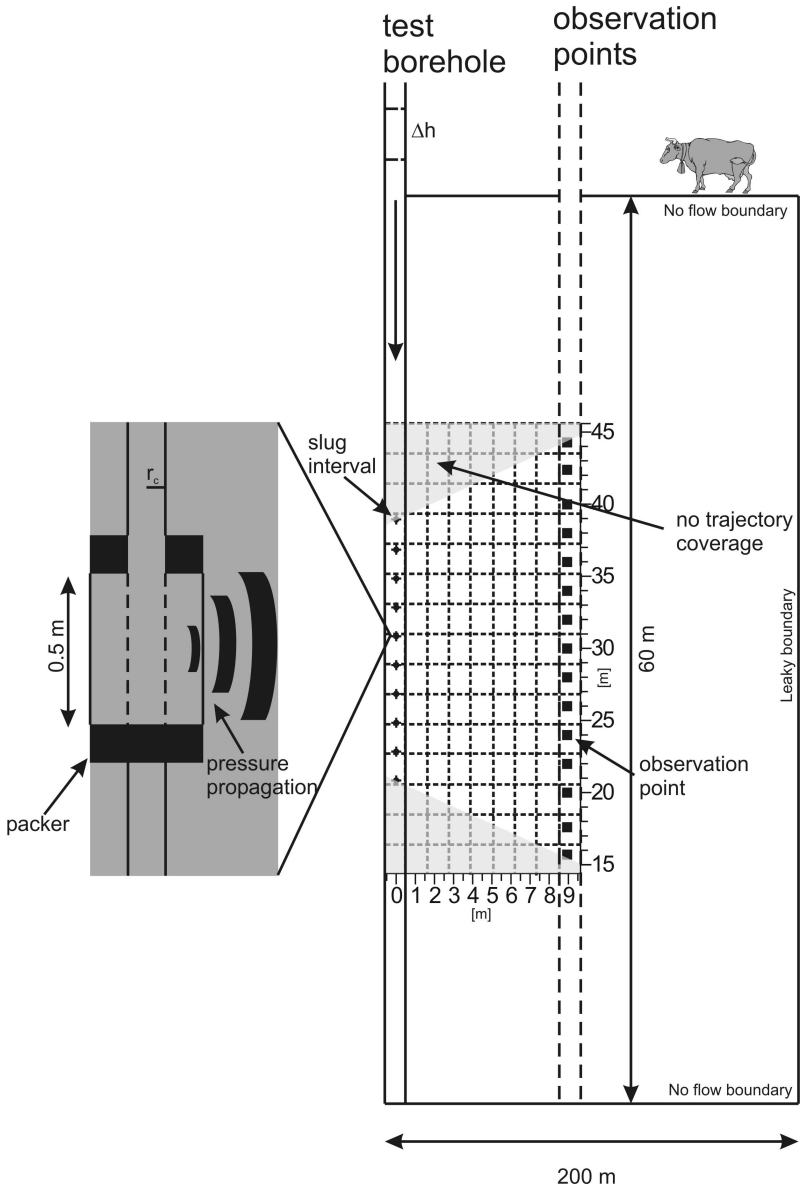

Figure 5.1 Concept of the forward model and inverse model of partially penetrating slug tests. Note the height of the aquifer is exaggerated.

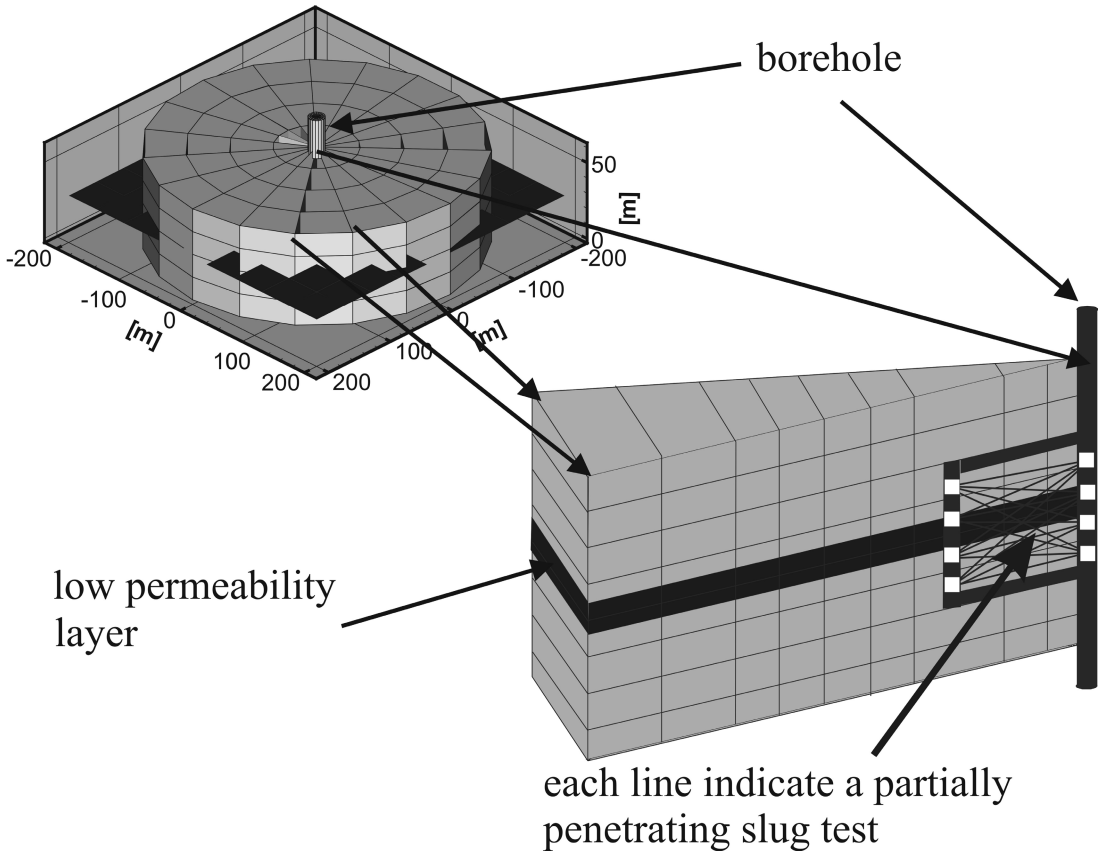

Figure 5.2 Design of the forward model. Note the used cells are not identical to the real mesh.

The model domain is axially symmetric and thereby the whole modeled aquifer structure is divided into 20 parts separated by 20 spokes (Figure 5.2). For an efficient computation just one part of the whole aquifer structure is chosen, enabling a two-dimensional forward modeling.

The radius of the borehole is 0.05 m and the injection interval in the borehole is made of 20 layers and two nodes in radial direction with built-in "packers" separating the injection interval from the open parts of the borehole. The porosity and the permeability of the borehole are set to high values ($0.999/10^{-8}m^2$, Table 5.1).

For the aquifer mesh hexahedral elements are used, with 26 nodes in the radial direction from 0.05 to 200 m applying a constant ratio spacing, with the first element size of less than 2 mm and a constant head boundary of about 80 m. In z-direction, perpendicular to the radial direction a constant ratio originating from the injection port upwards and downwards to upper and bottom boundaries is also used.

To build-up a complete model for the numerical simulation, the borehole and the aquifer mesh are merged together, and the initial head perturbation in the borehole is defined.

The borehole specific storage is included in the forward model in the following way:

The specific storage is defined as the percentage volume change per unit head:

$$S_c = \frac{\Delta V}{V} \cdot \frac{1}{\Delta h}$$

Eq. 5.1

The volume change ΔV in dependence of the head change Δh in the casing of the borehole can be expressed as follows

$$\Delta V = \pi r_c^2 \Delta h$$

Eq. 5.2

and the volume V is

$$V = \pi r_s^2 H$$

Eq. 5.3

where H is the injection length, r_s is the borehole radius and r_c is the casing radius. Therefore, Equation 5.1 can be expressed as follows

$$S_c = \frac{r_c^2}{r_s^2 H} .$$

Eq. 5.4

For the forward models proposed in section 5.2 the following two wellbore storages 0.002888 m^{-1} and 0.1444 m^{-1} are used, which yield to casing radii of 1.9 mm and 13.4 mm, respectively. The parameters used for the forward models are summarized in Table 5.1.

Each data set consists of 10 slugged intervals and 15 observation points, whereby the borehole distance is 9 m. That means each data set comprises 150 transient pressure curves. In Figure 5.1 the spatial position of the slugged intervals and the observation points are illustrated.

Table 5.1 Parameters used for the slug test simulation. Note, that the specific wellbore storage and the permeability of the aquifer vary in the different forward models proposed in section 5.2.

Initial head H_0	70 m
Aquifer thickness h_0	60 m
Specific aquifer storage S_S	2.888×10^{-6} m^{-1}
Specific wellbore storage S_C	0.002888 m^{-1} 0.1444 m^{-1}
Permeability of aquifer K_a (homogenous background)	10^{-12} m^2
Permeability of borehole K_b	10^{-8} m^2
Borehole radius r_s	0.05 m
Aquifer radius r_a	200 m
Aquifer porosity Φ_a	0.20
Time step T_s	10^{-7}-10^{-4} days

To demonstrate the validity of the forward calculations, the results are checked against the semianalytical solution by LIU AND BUTLER [1995] in the following called KGS-model.

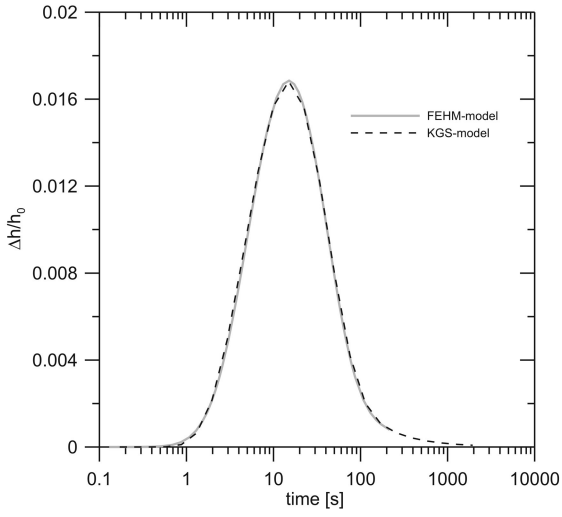

Figure 5.3 Comparison of the results of the KGS- and FEHM-model. For the models the input parameters given in Table 5.1 are used. The distance between injection and observation is 7.30 m.

The comparison of the forward model based on the FEHM-code with the semianalytical solution of the KGS-model are illustrated in Figure 5.3. The excellent agreement of the FEHM with KGS model results confirmed the validity of the forward calculations. The forward modeling was performed at the Texas A&M University, College Station; USA by Dr. J.-T. Cheng.

5.2.2 Inverse Modeling

The inversion is based on the technique which is described in chapter 3. For the diffusivity reconstructions, which are discussed in section 5.3, the travel times associated with 5 % (representing the early time of the signal) and 50 % (representing the intermediate time of the signal) of the maximum pressure change, i.e. of the pressure peak, are used. Additionally, the peak time (100 %) is inverted, enabling to verify the validity of the derived transformation factor (Figure 5.4). Note it is assumed that the initiation of a slug test can be described with a Dirac pulse.

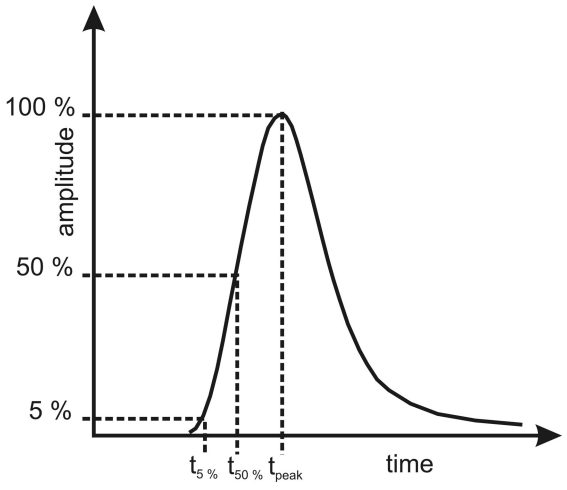

Figure 5.4 Illustration of the used travel times for the inversion proposed in section 5.3.

5.3 Results

In this section, the inversion results of synthetic data sets are presented. First, the influence of the wellbore storage on the travel time is investigated. In order to eliminate the travel time delay caused by wellbore storage a conversation factor is defined by using a homogenous reference model. Afterwards, the dependency of the inversion results from the inverted travel times is investigated, by means of two one-layer models, a two-layer model and finally, a two-layer model with a vertical offset (fault zone) (Figure 5.5). The permeability distribution is derived from the reconstructed diffusivity distribution by using the constant storage S_s coefficient known from the forward model.

5.3.1 Influence of Wellbore Storage

The wellbore storage affects the recorded signal of a slug interference test in two ways. For a given distance between the pulsed and the observation borehole, the wellbore storage causes a delay in the time at which the pressure is observed. Beyond this, the larger the wellbore storage using the same head change Δh, the larger is the response amplitude [PRATS AND SCOTT, 1975]. Under field conditions the influence of the wellbore storage on the travel time of the pressure signal is so high that the resulting time delay has to be corrected in order to interpret the data. For this reason, in the following two different wellbore storages are used. In order to represent field conditions the value 0.1444 m^{-1} for the wellbore storage is chosen. For the second forward model the value 0.002888 m^{-1} was chosen representing a data set which shows almost no influence of the wellbore storage. The second data set is used as a reference model. It is not possible to choose a smaller wellbore storage, as otherwise the amplitude of the recorded signal becomes too

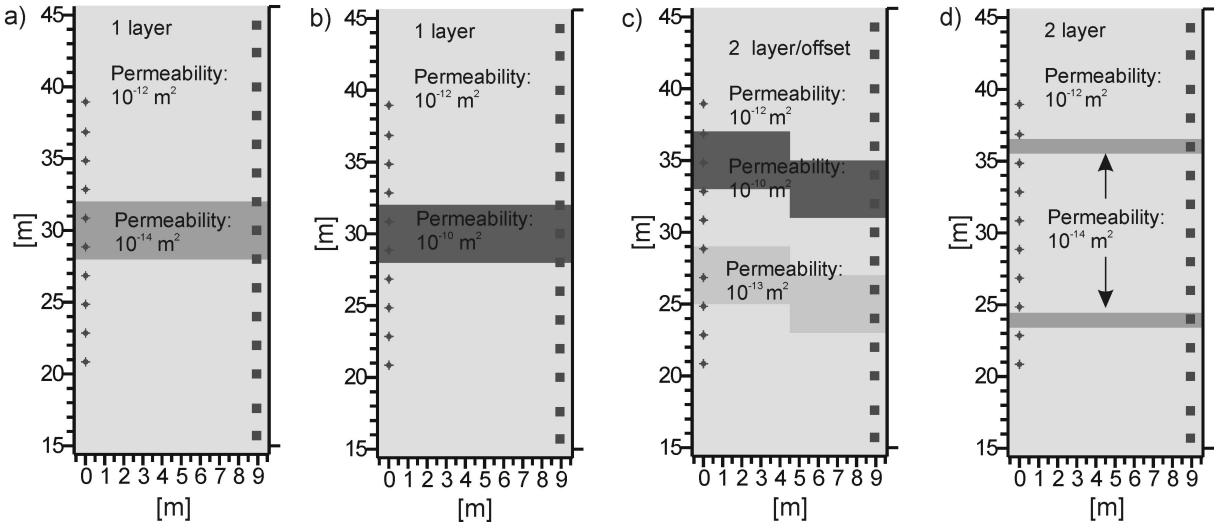

Figure 5.5 Outline of the forward models discussed in section 5.3.2 - 5.3.4. The crosses and the squares represent the spatial position of the slugged intervals (10) and the observation points (15), respectively.

small for a given Δh and it is not possible to reliably determine the peak time. In Figure 5.6 the travel times of two slug interference tests for the two different wellbore storages are illustrated. The input data sets are the same for both tests (Table 5.1) except that wellbore storage is varied as stated above.

In Figure 5.6a, b the travel times are plotted when 1 %, 5 %, 50 %, and 100 % (peak) of the maximum pressure is reached against the source-receiver-distance for two tests with different wellbore storages. The comparison of Figure 5.6a, b clearly indicates that the time delay is more pronounced for the simulated test with larger wellbore storages. The plots illustrated in Figure 5.6c, d are showing the ratio of the travel times for the two tests. The plots demonstrate that later travel times are more strongly affected by the time delay caused by the larger wellbore storage.

In Figure 5.7a, b the effects of the wellbore storage on the inversion results is illustrated by means of two tomograms based on the inversion of travel times when 5 % of the maximum is reached. For the simulation of the slug interference tests, a homogenous parameter distribution is used. The parameters are given in Table 5.1. The input parameters are the same for both simulated slug interference tests, except that wellbore storage is varied ($0.002888\ m^{-1}$ / $0.1444 m^{-1}$). The values of the permeability reconstruction based on the parameter set with the smaller wellbore storage agree very well with the permeability values used for the simulation of the slug tests, whereby the absolute variation of the reconstructed permeability values are smaller than approximately 20 %. It should be pointed out that uncertainties up to a deviation factor of 20 % are absolutely tolerable in context of water resources management. The reconstruction derived from the data set with the larger wellbore storage shows the same range with respect to the reconstructed permeability distribution, but the averaged absolute values are clearly lower. The described effects are much more pronounced for the reconstructions based on the peak time (Figure 5.7c, d).

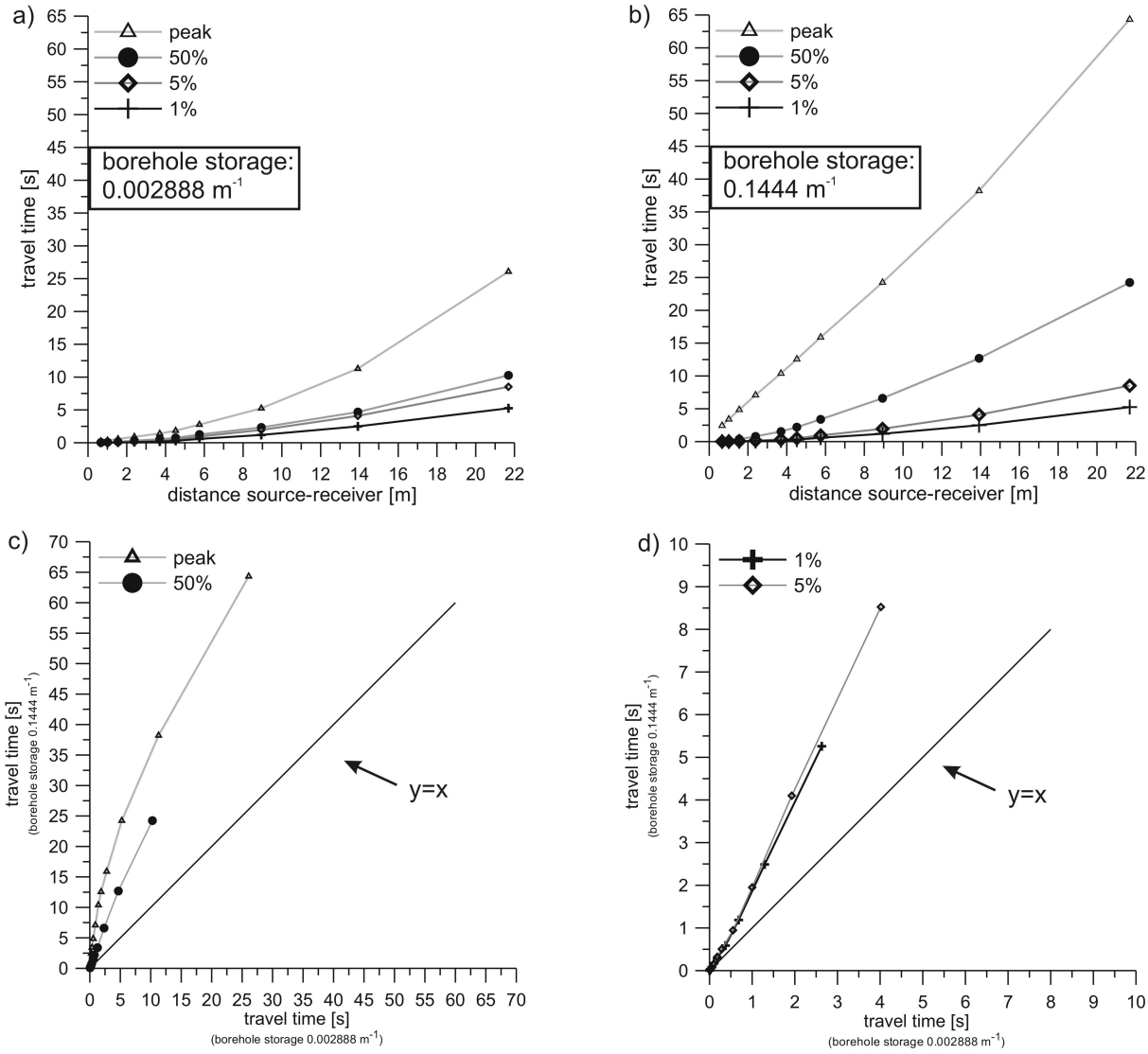

Figure 5.6 Comparison of travel times of slug interference tests simulated with two different wellbore storages. The travel times are plotted when 1 %, 5 %, 50 % and 100 % of the maximum pressure is reached.

In order to eliminate the effects of larger wellbore storages on the inversion results a homogenous reference model is used to correct the caused travel time delay. The main assumption is that the used wellbore storage for the reference model is small enough such that it is possible to neglect it. The tomogram illustrated in Figure 5.7a with a wellbore storage of 0.0002888 m^{-1} is used, as the reconstructed permeability values are most reliable. As the distance between injection interval and observation interval is influenced by the effects of the wellbore storage, each recorded transient pressure curve has to be corrected separately. The conversion factor using a homogenous model as a reference model is defined as follows:

$$C_j = \frac{t_j^{reference}}{t_j^{"true\ storage"}}$$

Eq. 5.5

whereby C_j is the conversion factor of the *j*th travel time, $t_j^{reference}$ is the *j*th travel time of the reference model and $t_j^{"true\ storage"}$ is the *j*th travel time of the model influenced by a ”significant” wellbore storage. By means of this conversion factor, all data sets

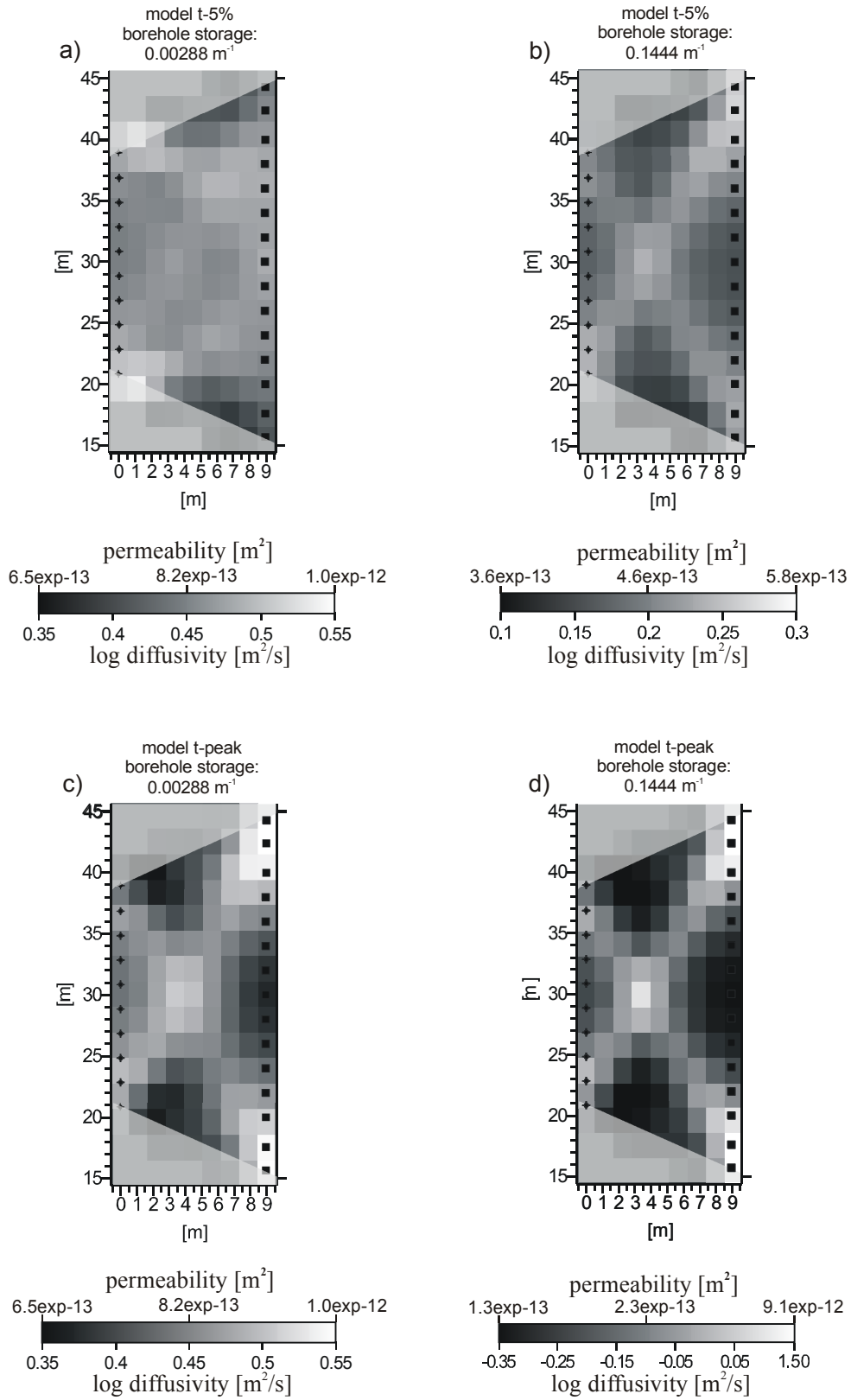

Figure 5.7 Inversion results for the travel times associated with 5 % and 100 % (peak time) of the maximum pressure change. The data base of the inversion comprises travel times obtained from simulated slug tests. For the forward model, a homogenous parameter distribution (Table 5.1) and two different wellbore storages are used.

illustrated in the following are corrected. Note that the conversion factor is just an approximation, since ray tracing techniques are used and consequently the length of travel paths of the pressure front are a function of the parameter distribution of the forward model (section 3.4). However, this procedure has the advantage that the reference model can be easily derived by using e.g. the semi-analytical solution of LIU AND BUTLER, [1995], since the needed input parameters such as spatial position of injection and observation ports and the wellbore storage are known.

5.3.2 One-Layer Model Including a Low Permeability Zone

In this section, a reconstruction of a forward model including one low permeability layer is shown. The spatial position of the slugged intervals and observation points, low permeability zone as well as the used permeability distribution are illustrated in Figure 5.5a. For the wellbore storage a value of 0.1444 m^{-1} was chosen and a head change of 5 m is used. The permeability reconstructions are based on the travel times when 5 %, 50 % and 100 % of the maximum pressure is reached. In the following, the tomograms are named "model t-5%", "model t-50%" and, "model t-peak."

All tomograms illustrated in Figure 5.8 show a dynamic range of the reconstructed permeability distribution of two orders of magnitude which agrees with the forward model. That indicates that the proposed conversion factor and inversion technique is working well for heterogeneous models. The homogenous background is reconstructed well in all three tomograms, but the transition zone between homogenous background and high permeability zone shows smearing effects, which are caused by the permeability difference of two orders of magnitude. Nevertheless, the comparison of the three tomograms demonstrates differences in quality between the reconstruction of the low permeability zone. It is evident that the inversion based on the travel time when 5 % of the maximum pressure change is reached, lead to the best results in regard to the identification of the spatial position of the low permeability zone.

With increasing travel time the reconstruction of the low permeability zone becomes more diffuse and especially the reconstruction based on the peak time shows almost no dynamic on the right part of the tomogram. But it has to be mentioned that the absolute value of the reconstructed low permeability zone on the left part based on the peak time are closest to the value used in the forward model.

For the explanation of the described observations, the travel time contour plots of the forward model and the run of the trajectories of the inverse model are used. In Figures 5.9 and 5.10, the travel time contour plots and the trajectories are shown for the slugged interval within the low permeability zone (z=29 m), and in Figures 5.11 and 5.12 the slugged interval is outside of the low permeability zone (z=35 m). The pattern of the travel time contour plots (Figure 5.9, z=29 m) of the forward models t-5% and t-50% follow the permeability distribution of the forward model. That means, the propagation in the low permeability zone is slower than in the homogeneous background. The travel time contour plot of t-peak shows a completely different distribution. The propagation of the pressure pulse seems to be not strongly affected by the low permeability zone. The isolines are arranged more or less concentrically and it is not possible to derive a low permeability zone from the imaged travel time contour plot.

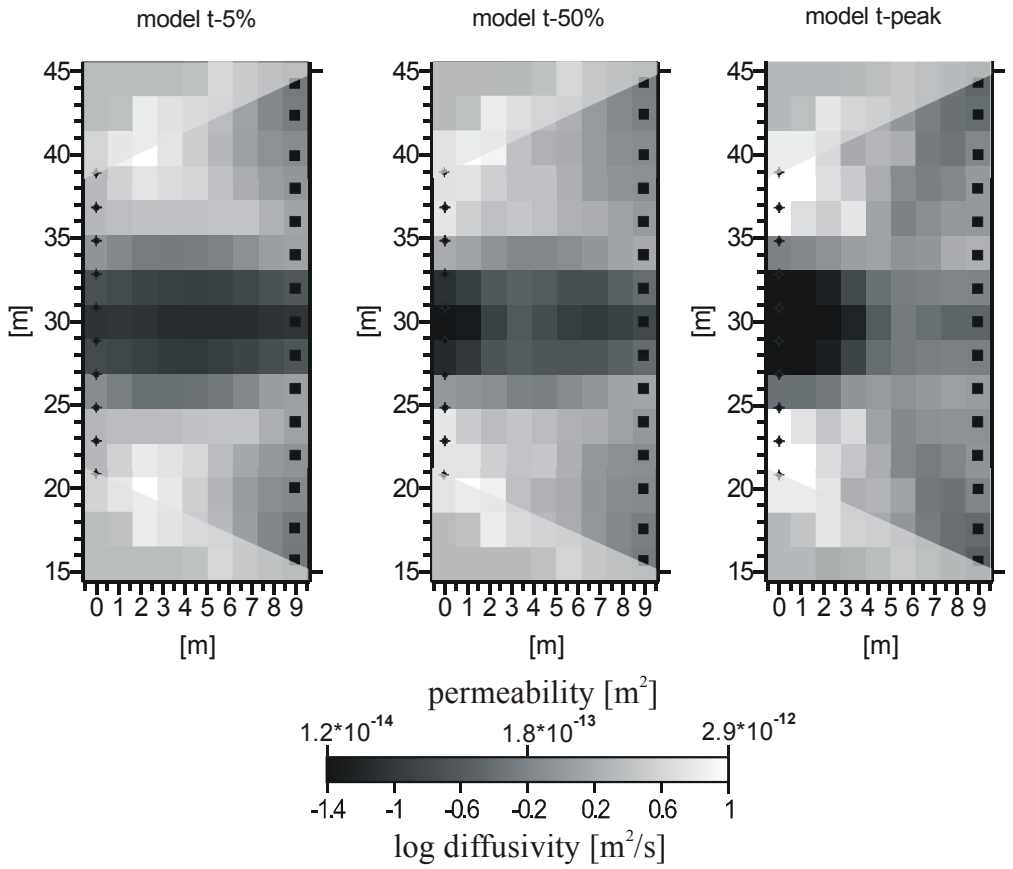

Figure 5.8 Inversion results for the travel times associated with 5 %, 50 % and 100 % (peak time) of the maximum pressure change. The data base of the inversion comprises travel times obtained from simulated slug tests. The permeability distribution used for the simulations is illustrated in Figure 5.5a. The specific aquifer storage is constant (Table 5.1). See color version of this figure in the Appendix (Fig. A-5).

In Figure 5.13 the pressure curves are illustrated in a distance of 1.5 m and 9 m at the spatial position z = 26 m, z = 30 m and z = 34 m (Figure 5.5a). The time is normalized to the square of the respective distances. The comparison of the two plots indicates that the sensitivity of the peak time is decreasing with distance. In a distance of 9 m, the peak time is almost the same for all three pressure curves. That means, the pressure distribution based on the peak time reflects the integral behavior, which explains the decreasing spatial resolution with increasing travel time. The travel time contour plots for the slugged interval outside the low permeability zone (z=35m, Figure 5.11) show more or less the same behavior and follow the permeability distribution of the forward model. But with increasing travel time, used for the inversion, the gradient of the contours becomes smaller in the region of the low permeability zone. This indicates the integral behavior of the later travel times and explains the increasing smearing effects of the reconstructions based on later travel times.

By comparing the trajectory plots (Figures 5.10 and 5.12) it is obvious that the trajectories "avoid" the low permeability zone with decreasing travel time. Since the trajectories of the t-peak model pass through the entire low permeability zone the absolute values on the left side of the tomogram are closest to the values of the forward model. On the right side of the tomogram the effect is prevailed by the integral behavior of the peak time.

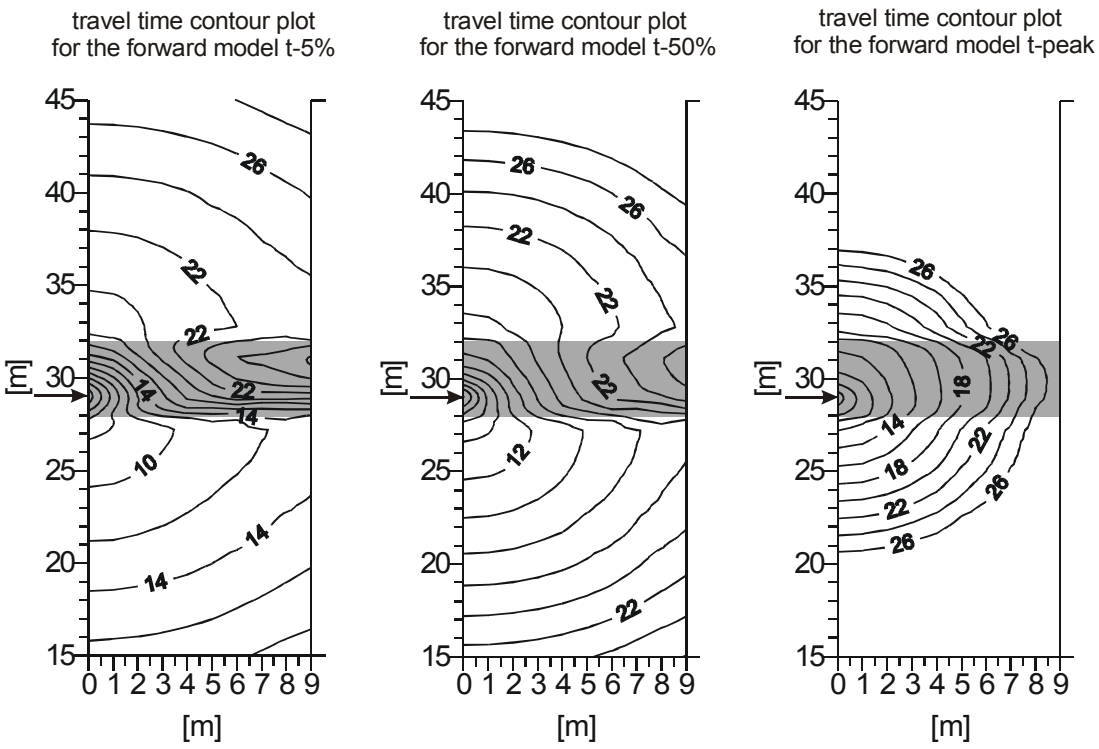

Figure 5.9 Travel time contour plot of the forward model for the travel times associated with 5%, 50%, and 100% (peak time) of the maximum pressure change. The used unit is seconds. A schematic sketch of the forward model and the used permeability distribution is imaged in Figure 5.5a. The arrows indicate the position of the slugged interval and the gray rectangle indicates the position of the low permeability layer.

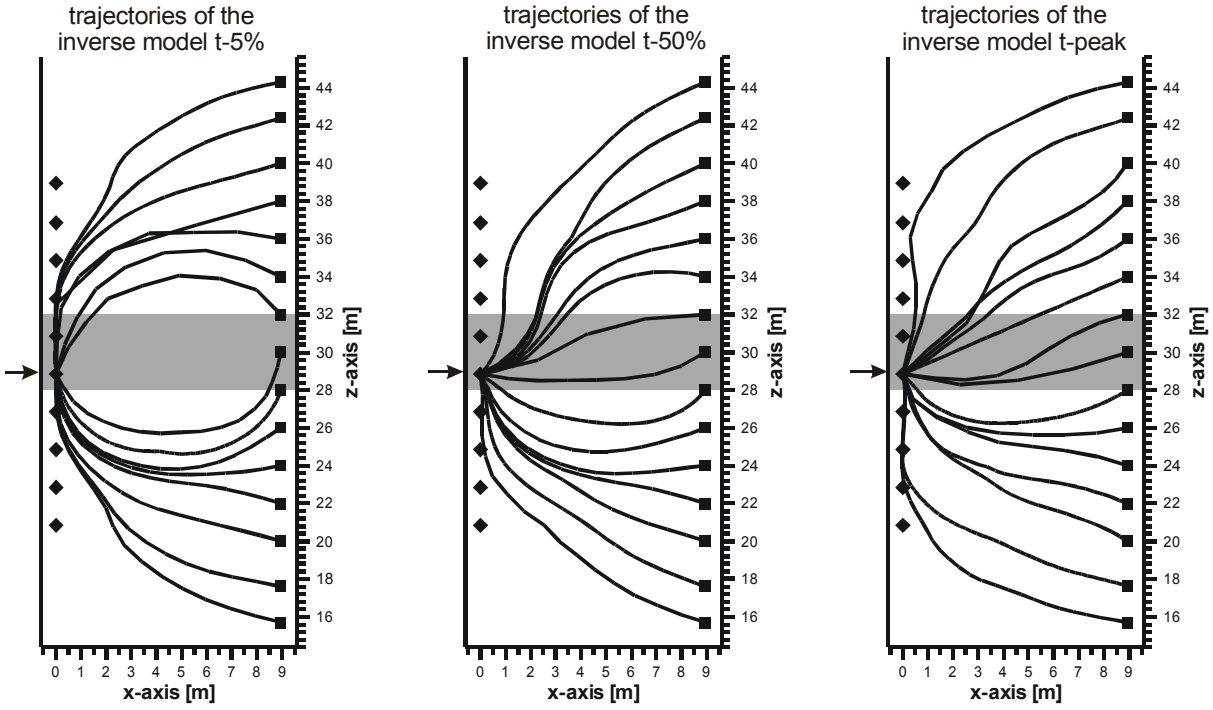

Figure 5.10 Trajectories of the reconstructions imaged in Figure 5.8 for the travel times associated with 5%, 50%, and 100% (peak time). The arrows indicate the position of the slugged interval and the gray rectangle indicates the position of the low permeability layer.

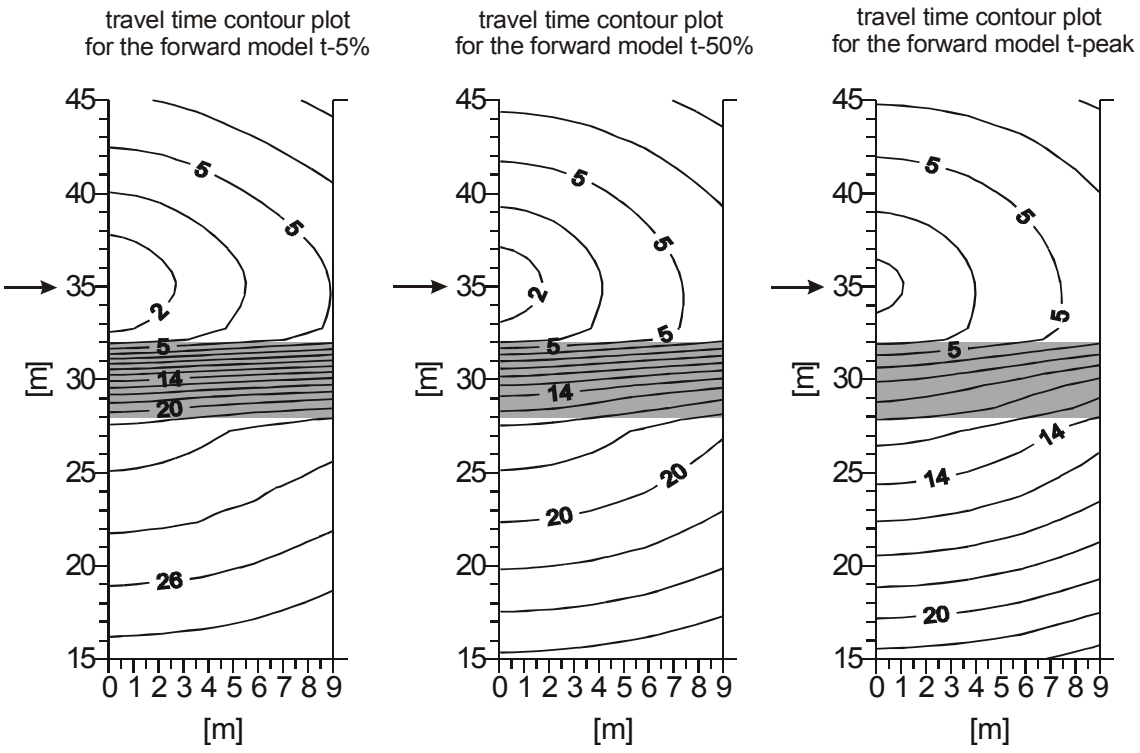

Figure 5.11 Travel time contour plot of the forward model for the travel times associated with 5%, 50%, and 100% (peak time) of the maximum pressure change. The used unit is seconds. A schematic sketch of the forward model and the used permeability distribution is imaged in Figure 5.5a. The arrows indicate the position of the slugged interval and the gray rectangle indicates the position of the low permeability layer.

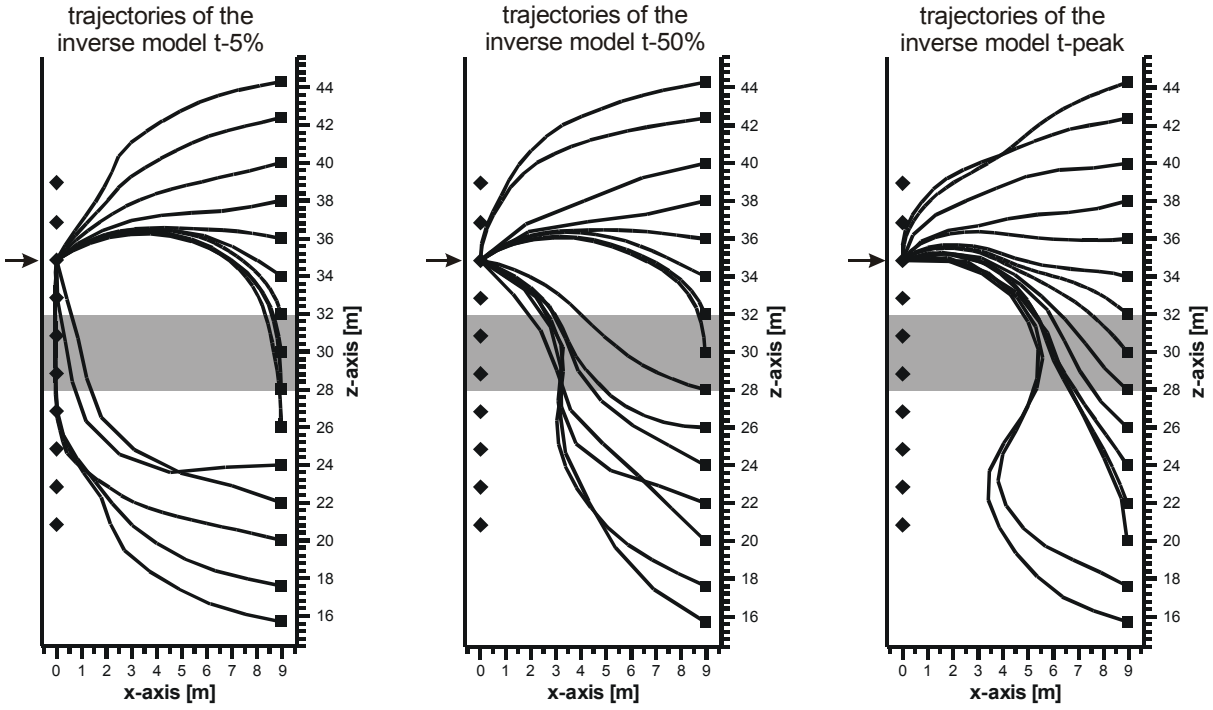

Figure 5.12 Trajectories of the reconstructions imaged in Figure 5.8 for the travel times associated with 5%, 50%, and 100% (peak time). The arrows indicate the position of the slugged interval and the gray rectangle indicates the position of the low permeability layer.

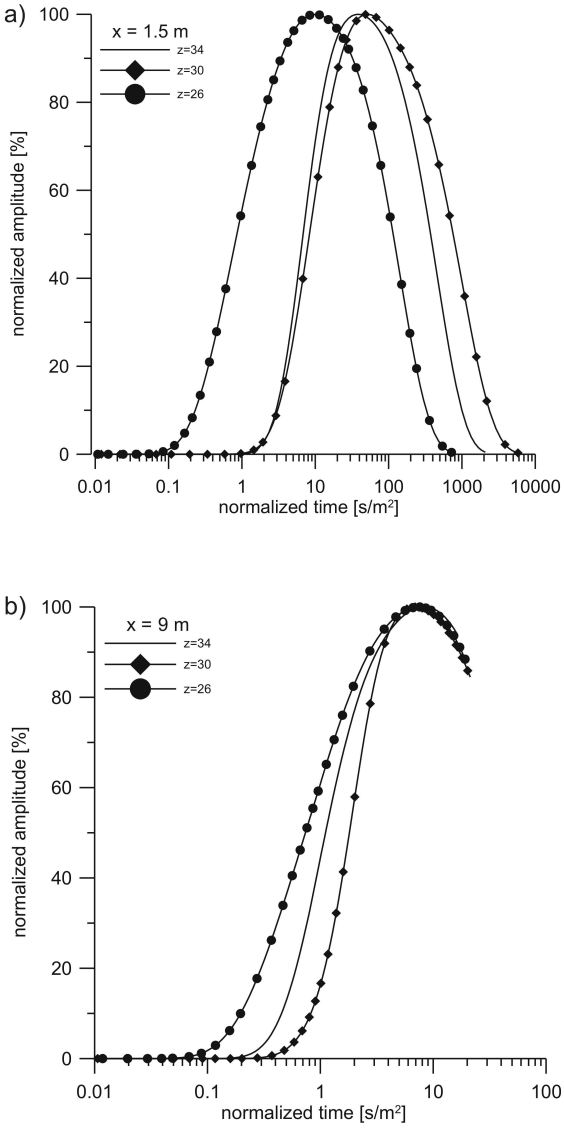

Figure 5.13 Illustration of pressure curves recorded in a distance of 1.5 m and 9 m at the spatial position z = 26 m, z = 30 m and z = 34 m. The used forward model is imaged in Figure 5.5a.

5.3.3 One Layer Model Including a High Permeability Zone

In this section the reconstructions of the forward model illustrated in Figure 5.5b are discussed. The used input parameters for the forward model are the same as for the forward model discussed in the section 5.3.2, but the low permeability layer is replaced with a high permeability layer. The effects on the inversion caused by the replacement of a low with a high permeability zone are illustrated by means of three permeability reconstructions based on the travel times when 5 %, 50 %, and 100 % of the maximum pressure is reached. All tomograms are illustrated in Figure 5.14. It is possible to image the different inversion results with the same color scale. This points out the reliability of the transformation factor derived in chapter 3. The inversions show a dynamic range of two orders of magnitude which agree with the forward model. Beyond this, the spatial position and the shape of the reconstructed high permeability zone agree also with the forward model.

In accordance with the reconstruction of the low permeability zone, the inversion based on the travel time when 5 % of the maximum pressure change is reached leads to the best results with regard to the identification of the spatial position of the high permeability zone. The gradient of the travel time contour plots illustrated in Figures 5.15 and 5.17 increase in the region of the high permeability zone with increasing travel time used for the inversion. This explains the more pronounced smearing effects of the models t-50% and t-peak in comparison to the model t-5%. In comparison with the reconstruction of the low permeability zone, the differences between inversion results are based on early and late travel times, respectively, are not so strongly pronounced.

In accordance with the reconstruction of the low permeability zone the tomogram based on the inversion of the peak time shows almost no dynamics on the right part. The travel time contour plot for the forward model t-peak imaged in Figure 5.17 is a good example for the influence of heterogeneity on travel time. The propagation on the right part is slower inside the high permeability zone than outside. Taking into account the distance from the slugged interval, the travel time contour plot is illustrating the integral behavior of the peak time which is already mentioned in section 5.3.3.

For all inversion models (model t-5%, model t-50%, model t-peak, Figure 5.14) the reconstructed permeability values in the center of the horizontal high permeability layers are too low. The reason for this might be that the calculated trajectories (Figures 5.16 and 5.18) are focused in the high permeability zone and thus the trajectories are crossing under small angles leading to limited lateral resolution.

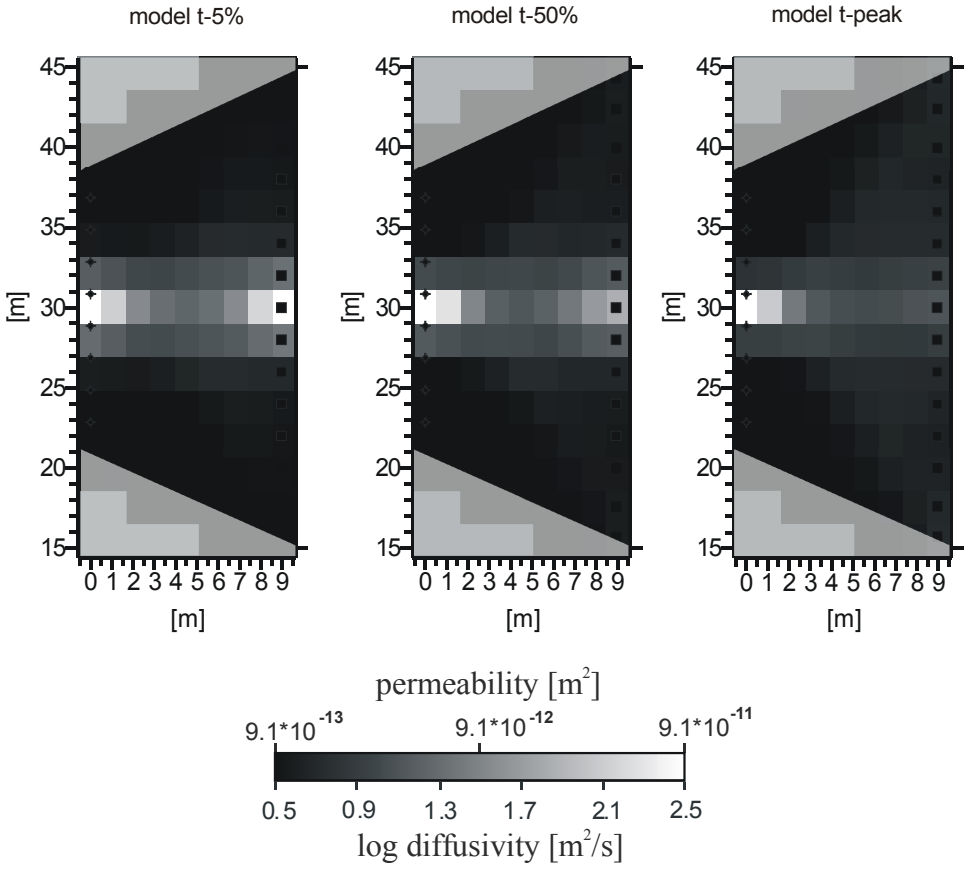

Figure 5.14 Inversion results for the travel times associated with 5%, 50%, and 100% (peak time) of the maximum pressure change. The data base of the inversion comprises travel times obtained from simulated slug tests. The used permeability distribution for the simulations is illustrated in Figure 5.5b. The specific aquifer storage is constant (Table 5.1). See color version of this figure in the Appendix (Fig. A-6).

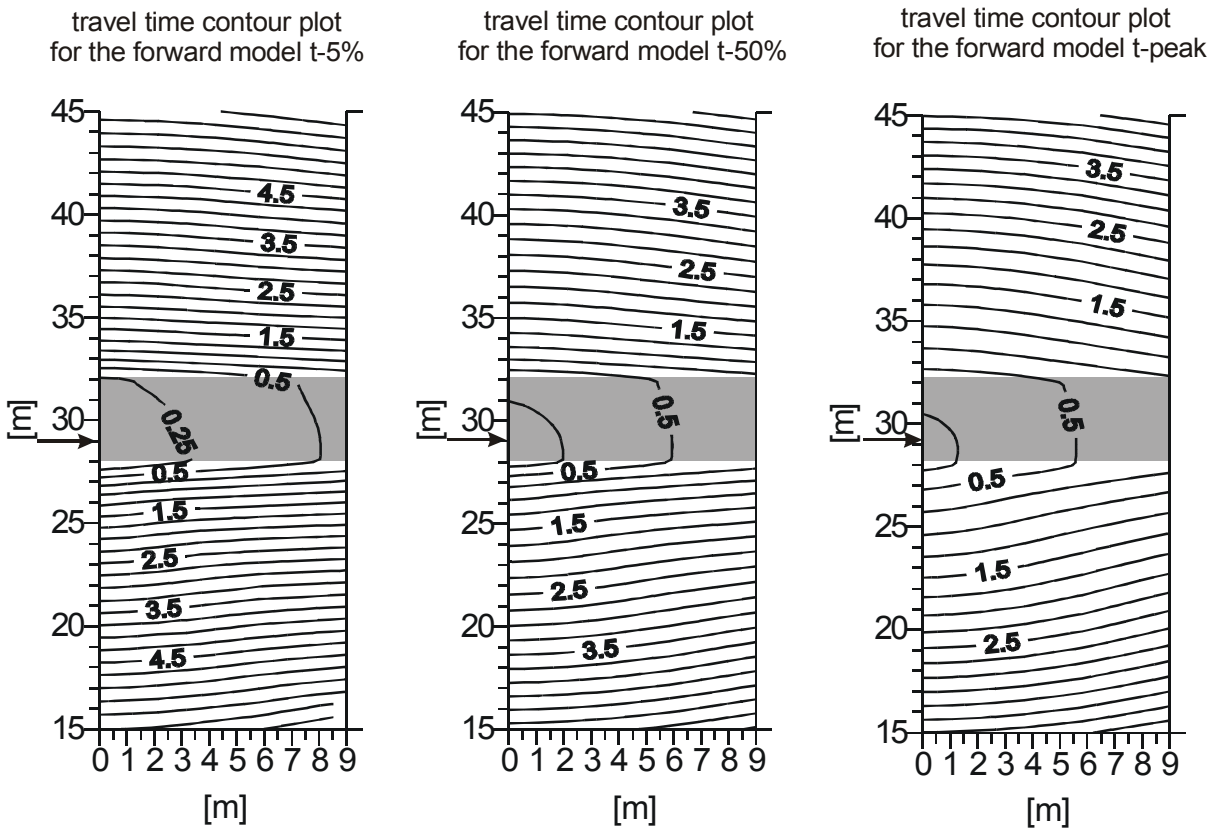

Figure 5.15 Travel time contour plot of the forward model for the travel times associated with 5 %, 50 %, and 100 % (peak time) of the maximum pressure change. The used unit is seconds. A schematic sketch of the forward model and the used permeability distribution is imaged in Figure 5.5b. The arrows indicate the position of the slugged interval and the gray rectangle indicates the position of the low permeability layer.

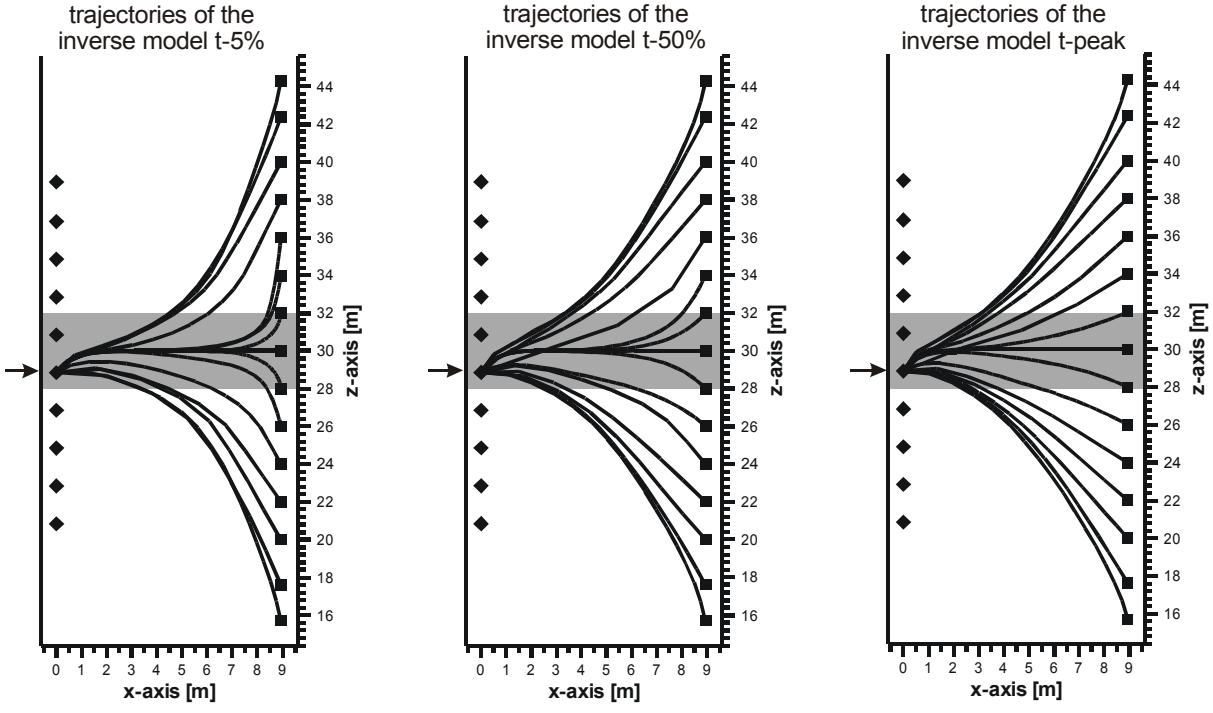

Figure 5.16 Trajectories of the reconstructions imaged in Figure 5.14 for the travel times associated with 5 %, 50 %, and 100 % (peak time). The arrows indicate the position of the slugged interval and the gray rectangle indicates the position of the low permeability layer.

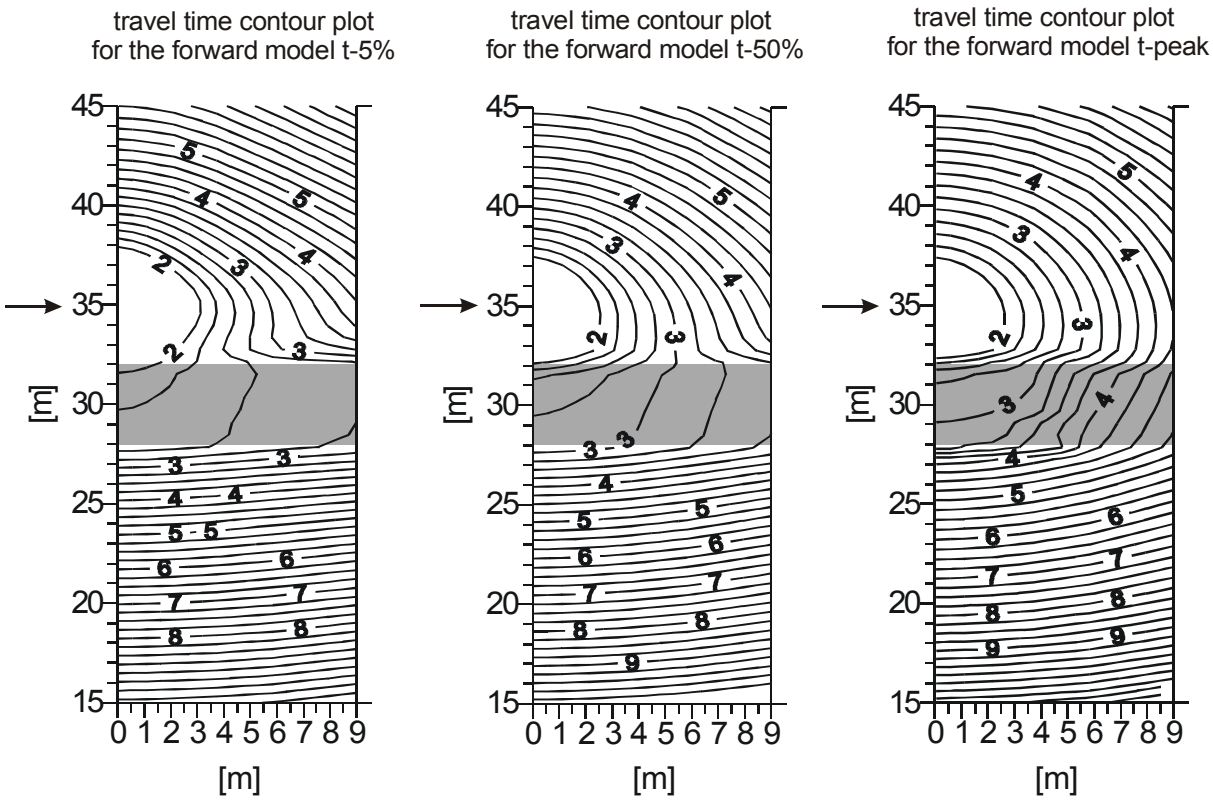

Figure 5.17 Travel time contour plot of the forward model for the travel times associated with 5 %, 50 %, and 100 % (peak time) of the maximum pressure change. The used unit is seconds. A schematic sketch of the forward model and the used permeability distribution is imaged in Figure 5.5b. The arrows indicate the position of the slugged interval and the gray rectangle indicates the position of the low permeability layer.

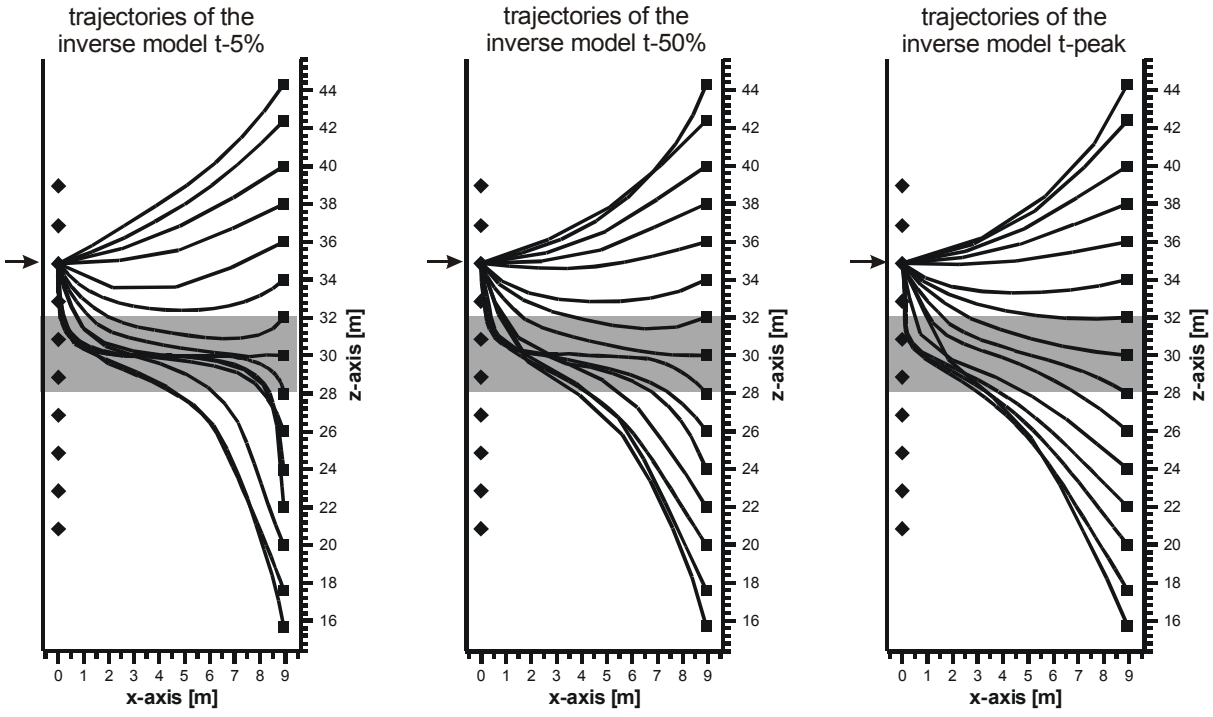

Figure 5.18 Trajectories of the reconstructions imaged in Figure 5.14 for the travel times associated with 5 %, 50 %, and 100 % (peak time). The arrows indicate the position of the slugged interval and the gray rectangle indicates the position of the low permeability layer.

5.3.4 Possibilities and Limitations of the Applied Approach

The possibilities and limitations of the applied inversion technique are discussed by means of the reconstruction of the two forward models illustrated in Figure 5.5c, d. For wellbore storage the same values as for the one-layer models are used (0.1444 m^{-1}).

First, the reconstruction of the forward model which comprises a low and a high permeability layer with a vertical offset, e.g a geological fault zone, is discussed. It has to be mentioned that a vertical offset is the most difficult structure to resolve as the offset is parallel to the boreholes and consequently the calculated trajectories are crossing the offset perpendicularly. Thus, the calculated trajectories in this part of the reconstruction are based on an averaged travel time between the homogenous background and the low and high permeability zone, respectively (Figure 5.19).

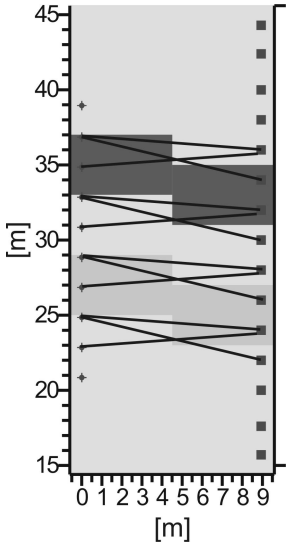

Figure 5.19 Schematic sketch of the calculated trajectories crossing the offset perpendicularly.

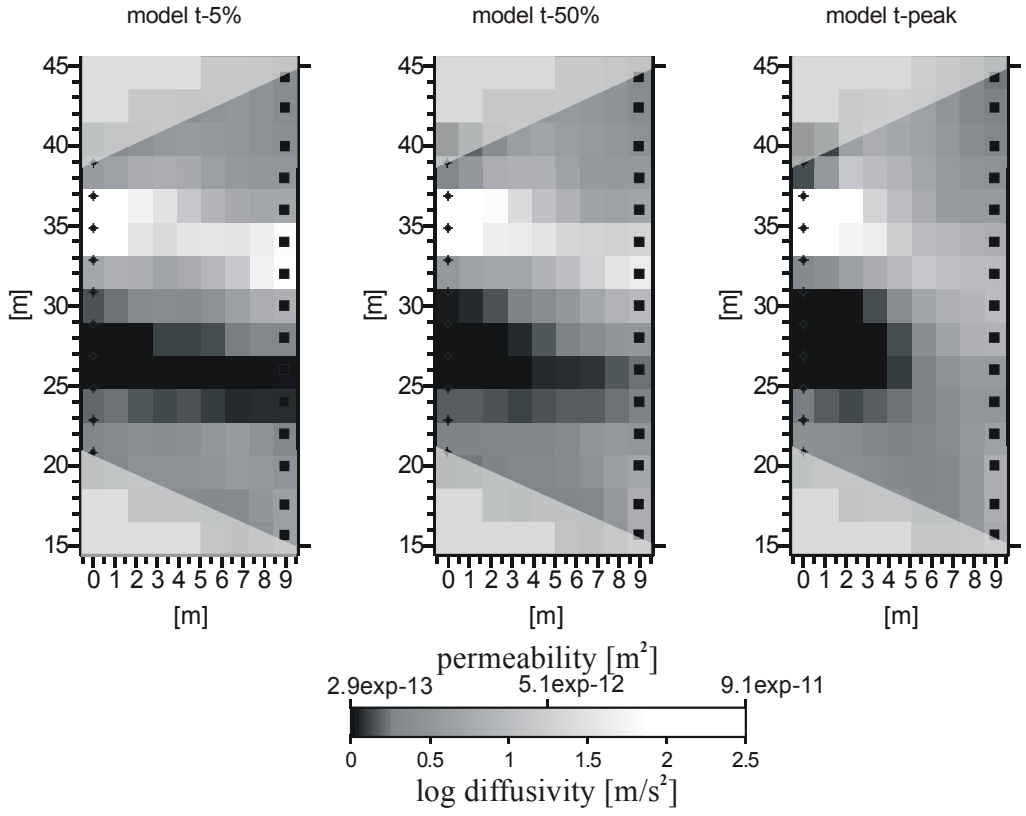

Figure 5.20 Inversion results for the travel times associated with 5 %, 50 %, and 100 % (peak time) of the maximum pressure change. The data base of the inversion comprises travel times obtained from simulated slug tests. The used permeability distribution for the simulations is illustrated in Figure 5.5c. The specific aquifer storage is constant (Table 5.1). See color version of this figure in the Appendix (Fig A-7).

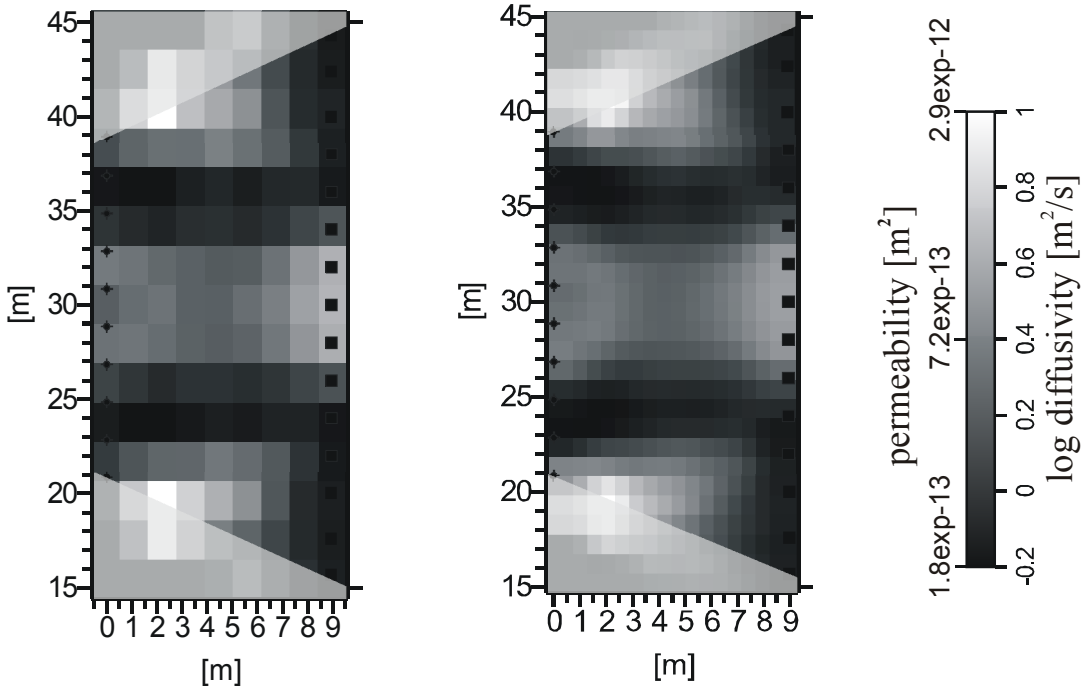

Figure 5.21 Inversion results for the travel times associated with 5 % of the maximum pressure change. Comparison of the inversion results by using conventional and a staggered grid. The data base of the inversion comprises travel times obtained from simulated slug tests. The used permeability distribution for the simulations is illustrated in Figure 5.5d. The specific aquifer storage is constant (Table 5.1). See color version of this figure in the Appendix (Fig A-8).

The structures and the permeability range is reconstructed sufficiently in the inverse model t-5% (Figure 5.20). The models t-50% and t-peak, which show increasing smearing effects, prohibit a reliable interpretation. The reasons of the decreasing spatial resolution with increasing travel time used for the inversion are already discussed in sections 5.3.2 and 5.3.3. Consequently, the following discussion focuses on model t-5%. As anticipated by VASCO ET AL. [2000], it is possible to reconstruct permeability distributions of 3 orders of magnitude by using the proposed inversion technique. In contrast to the reconstructed high permeability layer the reconstruction of the low permeability layer shows almost no transition zone to the homogenous background. One reason is that the permeability differences between low permeability zone and homogenous background is just one order of magnitude in comparison to the high permeability zone. Thus, if the permeability distribution covers four orders or more it can be anticipated that the transition zone and resulting smearing effects become so strong that the interpretation of the reconstruction will be limited.

Next, the reconstruction of the forward model comprising two low permeability layers with a thickness of 1 m are discussed (Figure 5.21). As the thickness of the used cells for the discretization is twice the thickness of the low permeability layers the interpretation of the reconstruction is limited. The insufficient cell size leads to the following effects:

- The dynamic range of the tomogram is too low.
- The spatial resolution of the tomogram is not satisfying.

In order to overcome this problem the method of staggered grid is applied (see section 4.4.1).

The comparison of the tomograms illustrated in Figure 5.21 indicates that the method of staggered grids leads to an improvement in resolution but the absolute values are still too low. In order to overcome this problem more receivers and sources are needed or a priori information enabling to refine the grid to a cell thickness of at least 1 m.

5.4 Further Discussion and Outlook

Chapters 4 and 5 have shown that the interpretation of the tomograms become more comprehensive as the reconstructions adapted from the inversions of different travel times reveal different details of the same investigated system. The investigations in chapter 5 allows to weight the reconstruction based on different travel times in dependence of the investigated geological medium. For the interpretation of low permeability zones it has to be taken into account that the inversions based on early travel time are more suited to resolve the spatial location of the structure while inversions based on late travel times are more suited to determine the absolute values. By the investigation of high permeability zones early travel times are most suited to conduct the inversion, but it has to be mentioned that in the center of the high permeability zone the reconstructed values are too low. The investigation of more complicated structures like fault zones or thin features, the potential run of the trajectories (position of sources and receivers) and the discretization have to be adapted to the investigated geological medium in order to get satisfying inversion results. Otherwise the limitation of the inversion have to be taken into account by the interpretation of the tomograms. The discussion demonstrates that a priori information about the investigated geological media helps to design the experiments, to conduct the inversions and to interpret the tomograms.

In order to eliminate the effects of larger wellbore storages on the travel time of a pressure pulse a homogenous reference model is used to correct the travel time delay. Based on this, a conversion factor is derived. Although the conversion factor is just an approximation for the heterogeneous case it is possible to minimize the influence of the wellbore storage and to reconstruct permeability distribution showing differences up to three orders of magnitude.

In future work it is planned to apply the proposed inversion technique to more complex structures like fracture networks in order to find out more details about the information content of the tomograms associated with different travel times. Beyond this, different kinds of a priori information or constraints, respectively, will be included in order to increase the nominal resolution. Particularly, the use of a priori information is essential for field applications.

6 Summary and Conclusions

The present thesis is motivated by the requirements to improve the knowledge about heterogeneous media in terms of flow and transport in fractured porous media. It is approved that the identification, spatial location determination and characterization of hydraulic significant features are the fundamental steps in understanding and predicting flow and transport in such media. Consequently, the objective of this work is to develop new investigation techniques enabling to resolve heterogeneities by the separation of the overall system into homogenous sections showing the same properties. Thereby, the main focus is on macroscopic heterogeneities, e.g the identification of hydraulically significant fractures in a homogenous matrix and the identification of significant differences in composition of the petrofabric of the matrix. Two approaches have been applied, both based on the evaluation of flow and/or transport experiments recorded in a tomographical array:

First, a multivariate statistical approach is demonstrated by analyzing 48 flow and transport experiments, which were conducted to a fissured cubic sandstone block on laboratory scale. This approach allows the identification of parameter zonation in terms of structure identification. The flow and transport experiments were conducted in a regular array using a gas flow and gas transport technique developed by MCDERMOTT [1999]. The objective of the approach was to identify groups of breakthrough curves reflecting different flow and transport properties of the investigated system. Due to the tomographic array of the injection and extraction points of the tracer, it is possible to determine the spatial distribution of the flow and transport properties.

The proposed methodology can be separated in two parts. The first part deals with the identification of uncorrelated variables sufficiently describing flow and transport experiments. Therefore, Hierarchical Cluster Analysis and Principal Component Analysis are used. The next step is to conduct the classification of the breakthrough curves by means of k-means Cluster Analysis using the uncorrelated variables determined in the first part.

The classification results are dominated by the textural composition of the matrix and it is evident that the fissure network has no significant influence. In order to demonstrate the validity of the proposed approach, the statistical results are verified by means of a geological surface mapping of the cubic sandstone block. The conformity between the statistical and the geological classification demonstrates that the presented multivariate statistical approach is a powerful tool for detecting natural groupings. Based on the classification results, a research group of the University of Stuttgart has developed a flow and transport model enabling to reproduce the recorded breakthrough curves.

The approach illustrates the usefulness of a priori investigations of the measured data sets

for a differentiation of significant characteristics that are inherent in the observed flow and transport data. Such a differentiation is appropriate for a reliable characterization of the investigated system,

- due to strong anisotropy and significant contrasts in the hydraulic conductivity in hard rocks, and
- since the measured data sets reflect the spatial variation of the distribution of the hydrogeological parameters.

Second, a hydraulic travel time tomography approach is demonstrated and applied to experimental and synthetic data sets. The starting point of the proposed approach is a line integral developed by VASCO ET AL. [2000] and KULKARNY ET AL. [2000] relating the square root of the drawdown peak arrival time of a transient pressure curve obtained for a Dirac source at the origin directly to the square root of the reciprocal value of diffusivity. In this thesis a further development of the travel time line integral is proposed. This advanced approach relates any recorded travel time corresponding to the arrival of a certain percentage of the maximum signal (e.g., 1 %, 10 %, 20 % of the maximum amplitude) to the peak time of a signal associated with a Dirac source. This relationship is derived for a Dirac source as well as for a Heaviside source. The advantage of simultaneously inverting several travel times is to exploit their different information content. For the inversion a least squares based inverse procedure is applied which is established since several years in seismic tomography.

The approach has been applied to data from a set of pneumatic short term tests conducted to a gas saturated fractured sandstone cylinder. For the purpose of reducing the duration of the experiments, pneumatic instead of hydraulic short term tests are performed. The experimental data set comprises 487 flow measurements, which were recorded at a gas saturated cylinder with a height of 34 cm and a radius of 31 cm. The experimental set-up is designed to produce a streamline pattern covering the whole cylinder, whereby the produced streamline pattern can be compared to the ray pattern of geophysical cross-hole tomography experiments.

The very good agreement between the reconstructed diffusivity distribution and the potential position of the fracture derived from the geological surface mapping of the sandstone cylinder shows obviously that it is possible to use algorithms for the inversion, which were originally developed for seismic travel time tomography. The used algorithm can handle the much higher travel time contrasts of hydraulic signals in comparison to seismic signals by the inversion without becoming unstable. Three different inversions were performed in order to reconstruct the three-dimensional diffusivity distribution. Although the travel times used for the inversions differ by more than one order of magnitude it was possible to use the same scale for imaging the diffusivity tomograms. The interpretation of the three-dimensional diffusivity distribution was shown to become more comprehensive as the tomograms adapted from the inversions of different travel times reveal different details of the same investigated system. The inversions based on early travel times are mainly related to preferential flow features while the inversions based on late travel times reflect an integral behavior.

Beyond this, the method of staggered grids is applied. Thereby, the grid is shifted three times and afterwards the three realizations are staggered in order to obtain more precise images with reduced dilution and smearing effects.

In order to get a better insight a detailed systematic study of the inversion based on several travel times characterizing the recorded transient pressure pulse is presented. The data base comprises the simulation of multi level slug tests conducted in a tomographical array between two boreholes. The forward modeling is conducted with the Mass Finite Element Heat and Mass Transfer Code (FEHM) from Los Alamos National Laboratory. The comparison of the inversion results, based on different travel times, with the forward model allows the verification and appraisal of the quality of the inversion. Hence, it is possible to suggest which travel time is most suited to reconstruct a certain subsurface structure. This allows to adapt the inversion strategy to the available a priori information of the investigated area.

The investigations allow to weight the reconstruction based on different travel times in dependence of the investigated geological medium. For the interpretation of low permeability zones it has to be taken into account that the inversions based on early travel times are more suited to resolve the spatial location of the structure while inversions based on late travel times are more suited to determine the absolute values. By the investigation of high permeability zones early travel times are most suited to resolve the spatial location of the structures as well as to determine the absolute permeability values. But it has to be mentioned that in the center of the high permeability zone the reconstructed values are too low. For the investigation of more complicated structures like fault zones or thin features, the experimental design (position of slugged intervals and observation intervals) and the discretization have to be adapted to the investigated geological medium by using a priori information such as geophysical data or borecore descriptions in order to get satisfied inversion results. Otherwise the limitation of the inversion has to be taken into account in the interpretation of the tomograms. The discussion demonstrates that a priori information about the investigated geological medium helps to design the experiments, to conduct the inversions and to interpret the tomograms.

In order to eliminate the effects of wellbore storages on travel times of a pressure pulse, a homogenous reference model is used to correct the travel time delay caused by storage effects. Based on the homogenous reference model a conversion factor is derived. Although the conversion factor is just an approximation for the heterogeneous case it is possible to minimize the influence of the wellbore storage and to reconstruct permeability distribution showing differences up to three orders of magnitude.

Furthermore both approaches, the multivariate statistical as well as the hydraulic travel time approach show clearly their capability to identify and characterize significant hydraulic features in fractured porous media. Additionally, the tomographical measurement array allows the spatial location determination. The approaches are applied to synthetic and experimental data sets but it is possible to apply the proposed methods without any restrictions to field data.

7 Outlook

7.1 Concept of the Diffusivity measurements on field scale length

Diffusivity is the quotient of hydraulic conductivity and storage. Diffusivity is a suitable parameter for the characterization of differences in the flow and migration paths because they accentuate the contrast between the fracture and the matrix dominated system. Usually, fractures have larger diffusivities due to their higher conductivity and the lower ability of storage consequently leading to shorter response times caused by a hydraulic stimulation. Therefore, diffusivity measurements are suited to investigate fractured and fractured porous aquifers. The measurements are conducted between two or more boreholes, whereby the distance between the boreholes can be several tens of meters. Thereby, the travel time between pumping well (source) and observation well (receiver) is determined. Using the travel time and distance between source and receiver, the effective diffusivity between the wells can be determined. A typical set-up of this kind of tests is summarized in Figure 7.1.

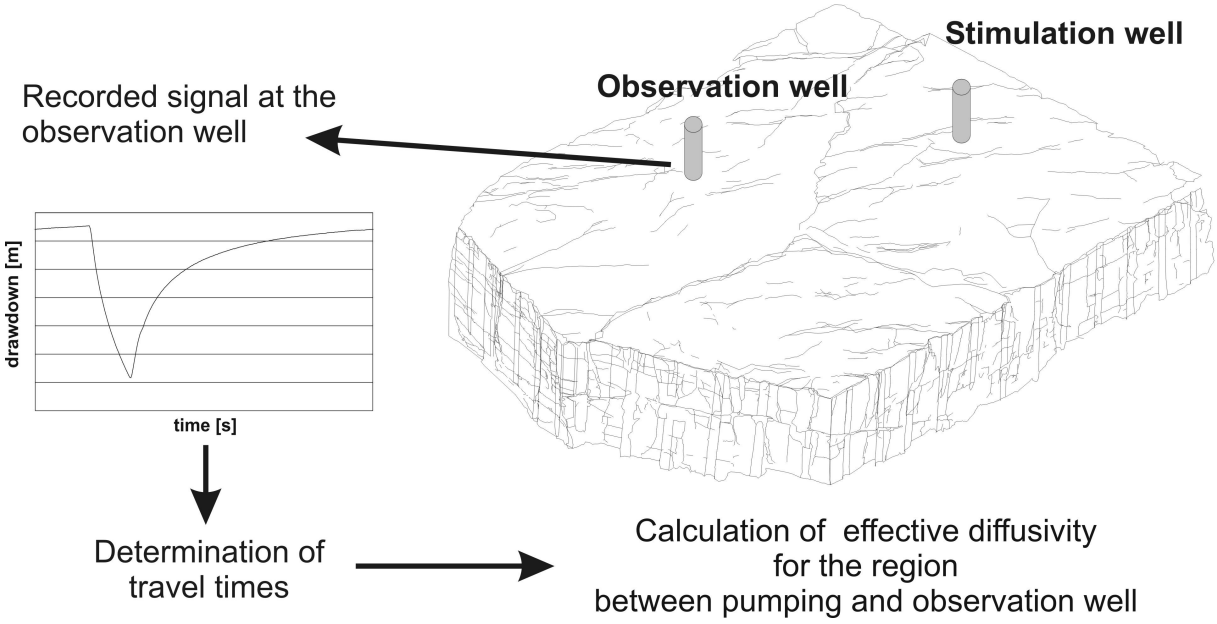

Figure 7.1 Illustration of the design and evaluation procedure of diffusivity measurements. Note that more than one observation well can be used to improve the significance of diffusivity measurements.

The main advantages of diffusivity measurements are discussed shortly in the following:

- The effective diffusivity is determined directly between one pumping well and one or more observation wells. The evaluation of steady state pumping tests in an anisotropic and heterogeneous medium is much more difficult as an exact assignment of the estimated parameters is still uncertain [LEVEN 2002].
- The design and the performance of diffusivity measurements are very variable. Hence, it is possible to adapt the type of stimulation signal to the geological medium. The diffusivity measurements can be conducted with a Dirac impulse, a Heaviside signal or a short term drawdown (boxcar signal) (Figure 7.2). The high variability allows to choose the most appropriate stimulation signal in order to avoid long pumping times and associated high costs. The most appropriate signal on field scale is the boxcar function, as the pumping time can be easily adapted to the permeability of the geological medium and the distance between pumping and observation well.
- As the diffusivity measurements are performed as a series of short term pumping tests it is possible to vary the position of the sources (pumps) and the receivers (pressure transducers) and to isolate them with packers (Figure 7.3) in a relatively small timeframe. This test design allows to produce a streamline pattern which can be compared with the crossed ray paths of a typical seismic tomography experiment. The travel times of the recorded transient pressure pulse can be inverted in order to produce a two- or three-dimensional diffusivity distribution of the investigated geological medium. The inversion technique is introduced in chapter 3

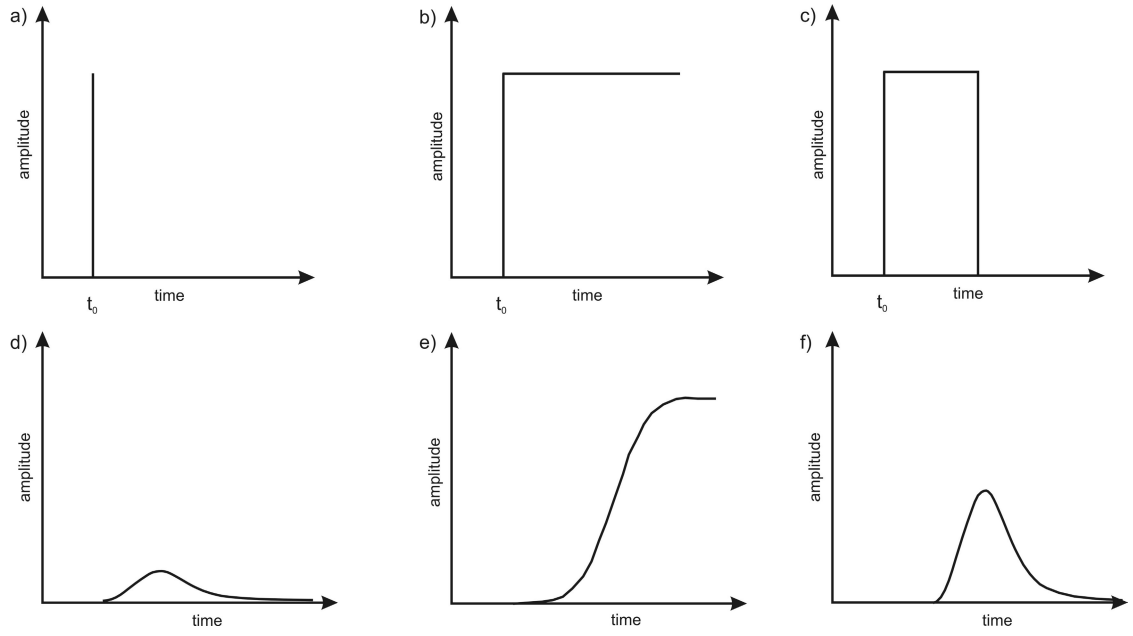

Figure 7.2 Different kinds of pumping signals. (a)-(c) and related observations. (a) & (d) Dirac signal / related observation, (b) & (e) Heaviside source / related observation, (c) & (f) Boxcar source / related observation.

and the application of the inversion technique to laboratory and synthetic data sets are described in chapters 4 and 5. The inversion technique is derived for a Heaviside and a Dirac source. In future work it is intended to derive such an inversion technique also for a boxcar source.

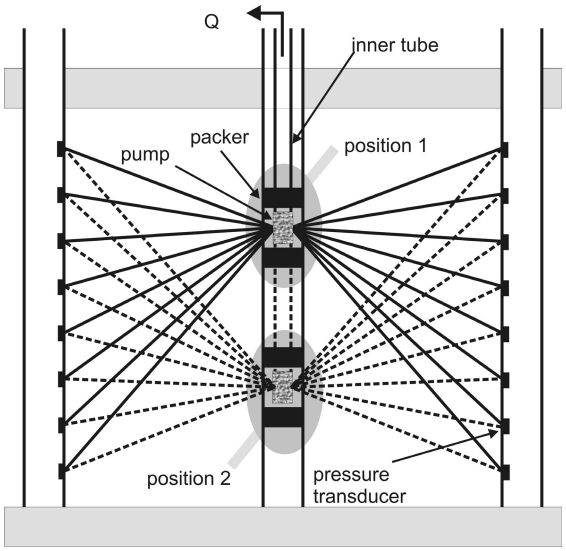

Figure 7.3 Schematic cross section of a hydraulic tomographic experiment. Two separate tests are illustrated, whereby the pump and the packers are moved from position 1 to position 2 after finishing the first test in order to perform the second. The solid lines represent the potential trajectories for the first test and the dotted lines represent the potential trajectories for the second test.

In the following the relationship is given between the length of the rectangular signal at the stimulation well, the arrival time of the maximum pressure change at the observation well, and the diffusivity between the two wells.

The radial symmetric diffusion equation in a homogenous medium describes the evolution of head *h* in dependence of time *t* and radial space coordinates r

$$\frac{S}{T}\frac{\partial h}{\partial t} = \frac{\partial^2 h}{\partial r^2} + \frac{1}{r}\frac{\partial h}{\partial r}$$

Eq. 7.1

where S denotes the storage coefficient and T the transmissivity. After the work by HÄFNER ET AL. [1992] the solution of the diffusion equation in an infinite domain for a Dirac source is

$$h(r,t) = -\frac{Q}{4\pi T} Ei\left[-\frac{r^2}{4T\cdot\frac{t}{S}}\right]$$

Eq. 7.2

with

$$-Ei(-x) = \int_x^{\infty} \frac{e^{-u}}{u}\partial u$$

Eq. 7.3

where Q is the flow rate, T is the transmissivity, and $h(r,t)$ is the hydraulic head depending on space (distance) and time. Using the principle of superposition, the solution for a boxcar source can be expressed as follows

$$h(r,t) = -\frac{Q}{4\pi T}\left[Ei\frac{r^2}{4T\frac{t}{S}} - Ei\frac{r^2}{4T\frac{t-t_2}{S}}\right].$$

Eq. 7.4

t-t_2 indicates the length of the rectangular signal. The time of the maximum pressure change can be determined by means of the first derivative of Equation 7.4.

$$\frac{\partial h}{\partial t} = \exp\left[-\frac{r^2 S}{4Tt}\cdot\frac{1}{t}\right] - \exp\left[-\frac{r^2 S}{4T(t-t_2)}\cdot\frac{1}{t-t_2}\right].$$

Eq. 7.5

Introducing $X = \frac{Sr^2}{4T}$ the first derivative becomes zero when

$$X = -\ln\left(1-\frac{t_2}{t_{peak}}\right)\cdot\frac{t-t_2}{1-\frac{t-t_2}{t_{peak}}}.$$

Eq. 7.6

Consequently, the time of the maximum pressure change can be expressed as a function of the ratio of hydraulic properties T and S, the distance r, and the duration of the rectangular signal t_2.

Diffusivity measurements are an alternative to conventional pumping or slug tests, especially in fractured porous media, as it is possible to determine the position of preferential flow paths. The high variability of the test design allows to minimize pumping time and allocated costs. In future it is intended to develop an inversion approach for a boxcar source in order to determine the three-dimensional diffusivity distribution of fractured porous aquifers.

8 References

Anderberg, M. R., Cluster analysis for applications. Academic Press, Inc., New York, 359 pp., 1973.

Backhaus, K., Multivariate Analysemethoden, Berlin, Germany, 810 pp., 2003.

Baehr, A. L. and M. F. Hult, Evaluation of unsaturated zone air permeability through pneumatic tests, Water Resourc. Res. 27(10), 2605-2617, 1991.

Bengelsdorf, K., Fazies- und Reservoirgeologie in Stubensandstein von Pliezhausen Rübgarten, Diplomarbeit an der Geowissenschaftlichen Fakultät der Universität Tübingen, Tübingen, Germany, 61 pp., 1997.

Beyer, W. Zur Bestimmung der Wasserdurchlässigkeit von Sanden und Kiesen. Z. Wasserwirt.-Wassertech., 14, 165-168, 1964.

Birkhölzer, J., Numerische Untersuchungen zur Mehrkontinuumsmodellierung von Stofftransportvorgängen in Kluftgrundwasserleitern, Mitteilungen des Instituts für Wasserbau und Wasserwirtschaft der Rheinisch-Westfälischen Technischen Hochschule Aachen Bd. 93, 226 pp., 1994.

Bloomfield, J.P., and A. T. Williams, An empirical liquid permeability – gas permeability correlation for use in aquifer properties studies, Quarterly Journal of Engineering geology, 28, 143 – 150, 1995.

Bohling, G. C., Hydraulic tomography in two-dimensional, steady state groundwater flow, Eos Trans. AGU, 74(16), Spring Meet. Suppl., 141, 1993.

Bois S., M. La Porte, M. Lavergne and G. Thomas, Well to well seismic measurements, Geophysics, 3, 471-483, 1972.

Bosch, M., M. Zamora, and W. Utama, Lithology discrimination from physical rock properties, Geophysics, 67(2), 573 – 581, 2002.

Brauchler, R., R. Liedl, and P. Dietrich, A travel time based hydraulic tomographic approach, Water Resour. Res., 39(12), 1370, doi:10.1029/2003WR002262, 2003a.

Brauchler, R., R. Liedl, and P. Dietrich, Identification of the diffusivity distribution by using a new hydraulic tomographic approach derived from travel time tomography, IAHR Conference, Groundwater in Fractured Rocks, Prague, 2 pp, 2003.

Brauchler R., C. Leven, P. Dietrich: A multivariate statistical approach for evaluating results of flow and transport experiments in an unsaturated fissured sandstone block. In: P. Dietrich, et al. [ed.], Flow and transport in fractured porous media, Springer, Berlin, Germany ISBN 3-540-23270-2, to be published in 2005.

Butler Jr., J. J., C. D. McElwee and G. C. Bohling, Pumping tests in networks of multilevel sampling wells: Motivation and methodology, Water Resources Research, 35(11), 3553-3560, 1999.

Clifton, P. M. and S. P. Neumann, Effects of kriging and inverse modeling on conditional simulation of the Avra Valley aquifer in southern Arizona, Water Resourc. Res. 18. 1215-1234, 1982.

Dagan, G., Stochastic modeling of groundwater flow by unconditional and conditional probabilities, 2, The solute transport, Water Resourc. Res. 18, 835-848, 1982.

Datta-Gupta A. and M. J. King, Semianalytic approach to tracer flow modeling in heterogenous permeable media, Advances in Water Resources, 18(1), 9-24, 1995.

Datta-Gupta A., K. N. Kulkarni, S. Yoon and D. W. Vasco, Streamlines ray tracing and production tomography: generalization to compressible flow, Petroleum Geoscience, 7, S75-S86, 2001.

Davis J. L. and A. P. Annan, Ground penetrating Radar for high-resolution mapping of soil and rock stratigraphy, Geophysical Prospecting, 37(5), 531-551, 1989.

Dietrich, P., R. Helmig, H. Hötzl, J. Köngeter, M. Sauter, and G. Teutsch, Flow and Transport in Fractured Porous Media, Springer, Berlin, Germany, ISBN 3-540-23270-2, to be published in 2005.

Dietrich P., T. Fechner and G. Teutsch, Einsatz tomographischer Verfahren zur Erkundung von Aquiferparametern- Z. Dt. Geol. Ges., 146(1), 161-166, 1995.

Dietrich, P., T. Fechner, J. Whittaker, and G. Teutsch, An integrated hydrogeophysical approach to subsurface characterization, in Groundwater Quality: Remediation and Protection, edited by K. Herbert and M. Kovar, IAHS Publ., 250, 513-519, 1998.

Dietrich P., T. Fechner and J. Whittaker, Anmerkungen zur Interpretation tomographischer Messungen. - Mitteilungen der Deutschen Geophysikalischen Gesellschaft, Sonderband II/1999: 13-21, 1999.

Dines K. A. and R. J. Lytle, Computerized Geophysical Tomography, Proc. IEEE, 67(7), 1065-1073, 1979.

Doherty, J., L. Brebber, and P. Whyte, Pest: Model Independent Parameter Estimation, Watermark Comput., Brisbane, Queensland, Australia, 1994.

Dumay, J., and F. Fournier, Multivariate statistical analyses applied to seismic facies recognition, Geophysics, 53(9) 18, 1151 - 1159, 1988.

Fechner, Th. and F. Meier, Seismische Tomographie im Nahbereich – Messungen auf dem Naturmessfeld Horkheimer Insel, Diplomarbeit, 56 pp., TU Bergakademie Freiberg, Freiberg, Germany, 1992.

Fechner, Th., and P. Dietrich, Lithological inversion of tomographic data, paper presented at 3rd Annual Meeting, Eur. Sect., Environ. And Eng. Geophys. Soc., Aarhus, Denmark, 1997.

Gable, C. W., H. E. Trease, and T. A. Cherry, Geological applications of automatic grid generation tools for finite elements applied to porous flow modeling, in Numerical Grid Generation in Computational Fluid Dynamics and Related Fields, edited by B. K. Soni, J. F. Thompson, H. Hausser, and P. R. Eiseman, Engineering Research Center, Mississippi State University Press, 1996.

Gable, C. W., T. A. Cherry, H. E. Trease, and G. A. Zyvoloski, Geomesh User's Manual, Los Alamos National Laboratories, Los Alamos, NM, 1996.

Gersztenkorn, A., Bednar, J., and Lines, L., Robust iterative inversion for the one-dimensional acoustic wave equation, Geophysics, 51, 357 – 368, 1986.

Gelbke Ch., Felslabor Grimsel – Seismische Durchschallungs-Tomographie, NAGRA NTB, 88-106, 1988.

Gilbert P., Iterative methods for three-dimensional reconstruction of an object from projections. J. theor. Biol. 36, 105-117, 1972.

Gill, D., A. Shomrony, and H. Fligelman, Numerical zonation of log suites and logfacies recognition by multivariate clustering, AAPG Bull., 77(10), 1781 –1791, 1993.

Gottlieb J. and P. Dietrich, Identification of the permeability distribution in soil by hydraulic tomography.- Inverse Problems, 11: 353-360, 1995.

Güler, C., G. D. Thyne, J. E. McCray, and A.K. Turner, Evaluation of graphical multivariate statistical methods for classification of water chemistry data, Hydrogeol. J., 10(4), 455 – 474, 2002.

Häfner F., D. Sames and H.-D. Voigt, Wärme und Stofftransport Mathematische Methoden, Springer Verlag, Berlin, 626 pp., 1992.

Hammah, R. E., and J. H. Curran, Fuzzy cluster algorithm for the automatic identification of joint sets, Int. J. Rock Mech. Min. Sci., 35(7), 889 – 905, 1998.

Harter, T. and T.-C. J. Yeh, Conditional stochastic analysis of solute transport in heterogeneous, variably saturated soils, Water Resourc. Res. 32(6), 1597-1609, 1996.

Hartigan, J. A., Clustering algorithms. John Wiley & Sons., Inc., New York, 315 pp., 1975.

Heling, D., Zur Petrologie des Stubensandsteins. Doktorarbeit an der Geowissenschaftlichen Fakultät der Universität Tübingen, Tübingen, Germany, 1963.

Hornung J. and T. Aigner, Reservoir and aquifer characterization of fluvial architectural elements: Stubensandstein, Upper Triassic, southwest Germany, Sedimentary Geology, 129, 215-280, 1999.

Huang, K., Y.W Tsang, and G.S. Bodvardson, Simultaneous inversion of air-injection tests in fractured unsaturated tuff at Yucca Mountain. Water Resourc. Res. 35(8), 2375-2386, 1999.

Hubbard S. S., J. E. Peterson, J. Roberts and F. Wobber, Estimation of permeable pathways and water content using tomographic radar data. The Leading Edge, 16 (11),1623-1628, 1997.

Illman, W. A., S. P. Neumann, Type curve interpretation of a cross-hole pneumatic injection test in unsaturated fractured tuff. Water Resourc. Res. 37(3), 583-603, 2001.

Jackson M. J. and D. R. Tweeton, MIGRATOM – Geophysical Tomography Using Wavefront Migration and Fuzzy Constraints. United States Department of the Interior, Bureau of Mines, Report of Investigations 9497, 35 pp, 1994.

Jackson M. J. and D. R. Tweeton, 3DTOM: Three-dimensional Geophysical Tomography, United States Department of the Interior, Bureau of Mines, Report of Investigation 9617, 84 pp, 1996.

Jansen D., Identifikation des Mehrkontinuum-Modells zur Simulation des Stofftransportes in multiporösen Festgesteinsaquiferen, Technische Hochschule Aachen / Lehrstuhl und Institut für Wasserbau und Wasserwirtschaft: Mitteilungen; 118, Eigenverlag, Aachen, Germany, 1999.

Jaritz, R., Quantifizierung der Heterogenität einer Sandsteinmatrix am Beispiel des Stubensandsteines. Tübinger Geowiss. Arb., Reihe C, 48, Cent. for Appl. Geosci., Tübingen, Germany, 106 pp, 1998.

Jöreskog, K. G., J. E. Klovan,. and, R. A Reyment, Geological Factor Analysis. Elsevier, Amsterdam, 178 pp, 1976.

Karasaki, K., B. Freifeld, A. Cohen, K. Grossenbacher, P. Cook, and D. Vasco, A multidisciplinary fractured rock characterization study at Raymond field site, Raymond, CA. Journal of Hydrology 236, 17-34, 2000.

Kaiser, H. F., The varimax criterion for analytical rotation in factor analysis. Psychometrika, 35, 187-200, 1958.

Kitanidis, P. K., The minimum structure solution to the inverse problem, Water Resourc. Res. 33(10), 2263-2272, 1997.

Koehler, F., and Tanner, M., The use of conjugate-gradient algorithms in the computation of predictive deconvolution operators, Geophysics, 50, 2752 – 2758, 1985.

Kohn R. and M. Vogelius, Determining conductivity by boundary measurements, Commun. Pure Applied Math. 37, 113-123, 1984.

Kulkarni, K. N., A. Datta-Gupta and D. W. Vasco, A Streamline Approach to Integrating Transient Pressure Data into High Resolution Reservoir Models, SPE Journal, 6(3), 2001.

Leven C., Effects of Heterogeneous Parameter Distributions on Hydraulic Test- Analysis and Assessment, Tübinger Geowiss. Arb., C 65, Cent. for Appl. Geosci., Tübingen, Germany, 88 pp, 2002.

Leven C., R. Brauchler, M. Sauter, G. Teutsch, P. Dietrich: Flow and transport experiments conducted to fractured porous laboratory blocks. In: P. Dietrich, et al. [ed.], Flow and transport in fractured porous media, Springer, Berlin, Germany to be published in 2004.

Liu, W. Z., and J. J. Jr. Butler, The KGS model for slug tests in partially penetrating wells (version 3.0), Kans. Geol. Surv. Comput. Ser. Rep. 95-1, 1995.

Long, J.C.S., and D. M. Billaux, From field data to fracture network modeling: An example incorporating spatial structure. Water Resourc. Res. 23(7), 1201-1216, 1987.

Malmgrem, B. A. and B. U. Haq, Assessment of quantitative techniques in Paleobiogeography. *Marine Micropaleontology*, 7, 213-236, 1982.

Mauch, S.,. Bestimmung der Matrixdiffusionskoeffizienten und hydraulischer Leitfähigkeit verschiedener Sandsteine Süddeutschlands, Diplomarbeit an der Geowissenschaftlichen Fakultät der Universität Tübingen, Tübingen, Germany, 1993.

M^{c}Dermott, C. I., New Experimental and Modelling Techniques to Investigate the Fractured Porous System, Tübinger Geowiss. Arb., Reihe C, 52, Cent. for Appl. Geosci., Tübingen, Germany, 166 pp, 1999.

McQueen, J., Some methods for classification and analysis of multivariate observations. 5th Berkeley Symposium on Mathematics, Statistics and Probalility,1, 281-298, 1967.

Meng, S. X., and J. B Maynard, Use of statistical analysis to formulate conceptual models of geochemical behavior: Water chemical data from the Botucatu aquifer in Sao Paulo state, Brazil. Journal of Hydrology, 250, 78-79, 2001.

Menke W., The Resolving Power of Cross-borehole Tomography, Geophysical. Research. Letters., v. 11, 105-108, 1984.

Menke W., Geophysical Data Analysis: Discrete Inverse Theory, Academic Press, INC, International Geophysics Series 45, 289 pp, 1989.

Mersereau, R. M. and A. V. Oppenheim, Digital reconstruction of multidimensional signals from their projections, Proc. IEEE, 62 (10), 1319-1338, 1974.

Nekut, A. G., Electromagnetic ray-trace tomography, Geophysics, 59(3), 371 – 377, 1994.

Prat, M. and J. B. Scott, Effect of Wellbore Storage on Pulse-Test Pressure Response, J. Pet. Tech. 707 – 709, 1975.

Rasmussen, T. C., D. D. Evans, P. J. Sheets, and J. H. Blanford, Permeability of Apache Leap Tuff: Borehole and Core Measurements Using Water and Air, Water Resourc. Res. 29, 1997 - 2006, 1993.

Schad, H., Variability of hydraulic parameters in non-uniform porous media: Experiments and stochastic modelling at different scales, Tübinger Geowiss. Arb., Reihe C, 35, Cent. for Appl. Geosci., Tübingen, Germany, 245 pp, 1996.

Scudder, H. J., Introduction to computer aided tomography, Proc. IEEE, 66, 1978.

Süß, M., Analysis of the influence of structures and boundaries on flow and transport processes in fractured porous media, University of Stuttgart, Germany, to be published in 2004.

Systat Version 9, copyright© SPSS Inc.

Trease, H. E., D, George, C. W. Gable, J. Fowler, A. Kuprat, and A. Khamyaseh, The X3D grid generation system, in 5th International Conference on Numerical Grid Generation in Computational Fluid Dynamics and Related Fields, edited by B. K. Soni et al., pp. 239 – 244, Eng. Res. Cent., Miss. State Univ. Press, Mississippi State, 1996.

Tronicke J., K. Holliger, W. Barrash, and M. D. Knoll, Multivariate analysis of cross-hole georadar velocity and attenuation tomograms for aquifer zonation, Water Resourc. Res. 40, W01519, doi: 10.1029/2003WR002031, 2004.

Um J. and C. Thurber, A fast algorithm for two –point seismic ray tracing. Bulletin of the Seismological Society of America, 77(3), 972-986, 1987.

Vasco D. W., S. Yoon and A. Datta-Gupta, Integrating dynamic data into high resolution reservoir models using streamline based analytic sensitivity coefficients, SPEJ Soc. Pet. Eng. J., 1-11, 1999.

Vasco D. W. and A. Datta-Gupta, Asymptotic solutions for solute transport: A formalism for tracer tomography, Water Resources Research 35(1), 1-16, 1999.

Vasco D. W., H. Keers and K. Karasaki, Estimation of reservoir properties using transient pressure data: An asymptotic approach, Water Resources Research, 36(12), 3447-3465, 2000.

Vesnaver A. and G. Böhm, Staggered or adapted grids for seismic tomography, Leading Edge 19 (9), 944-950, 2000.

Vesselinov, V. V., S. P. Neumann, and W. A. Illmann, Three-dimensional numerical inversion of pneumatic cross-hole tests in unsaturated fractured tuff, 1. Methodology, Water Resourc. Res. 37(12), 3001-3017, 2001a.

Vesselinov, V. V., S. P. Neumann, and W. A. Illmann, Three-dimensional numerical inversion of pneumatic cross-hole tests in unsaturated fractured tuff, 2. Equivalent parameters, high-resolution stochastic imaging and scale effects, Water Resourc. Res. 37(12), 3019-3041, 2001b.

Virieux J., C. Flores-Luna and D. Gibert, Asymptotic theory for diffusive electromagnetic imaging Geophys. J. Int., 119, 857-868, 1994.

Wang R., and S. Treitel, The determination of digital Wiener filters by means of gradient methods, Geophysics, 38, 310 – 326, 1973.

Wang Y., T. Luo, and Z. Ma., Geostatistical and geochemical analysis of surface water leakage into groundwater on a regional scale: A case study in the Liulin karst system, northwestern China, 2001.

Yeh, T.-C. J. and J. Zhang, A geostatistical inverse method for variably saturated flow in the vadose zone, *Water Resourc. Res.* 32(9), 2757-2766, 1996.

Yeh T.-C. Jim and S. Liu, Hydraulic tomography: Development of a new aquifer test method, Water Resources Research 36 (8), 2095-2105, 2000.

Yorkey T. J. and J. G. Webster, Tompkins W. J., Comparing reconstruction algorithms for electrical impedance tomography. IEEE Trans. On Biomedical Eng. BME-34, 843-852, 1987.

Zyvoloski, G. A., B. A. Robinson, Z. V. Dash, and L. L. Trease, Models and methods summary for the FEHM application, Los Alamos National Laboratories, Los Alamos, NM, 1995.

Appendix

Color version of the imaged tomograms in chapters 4 and 5

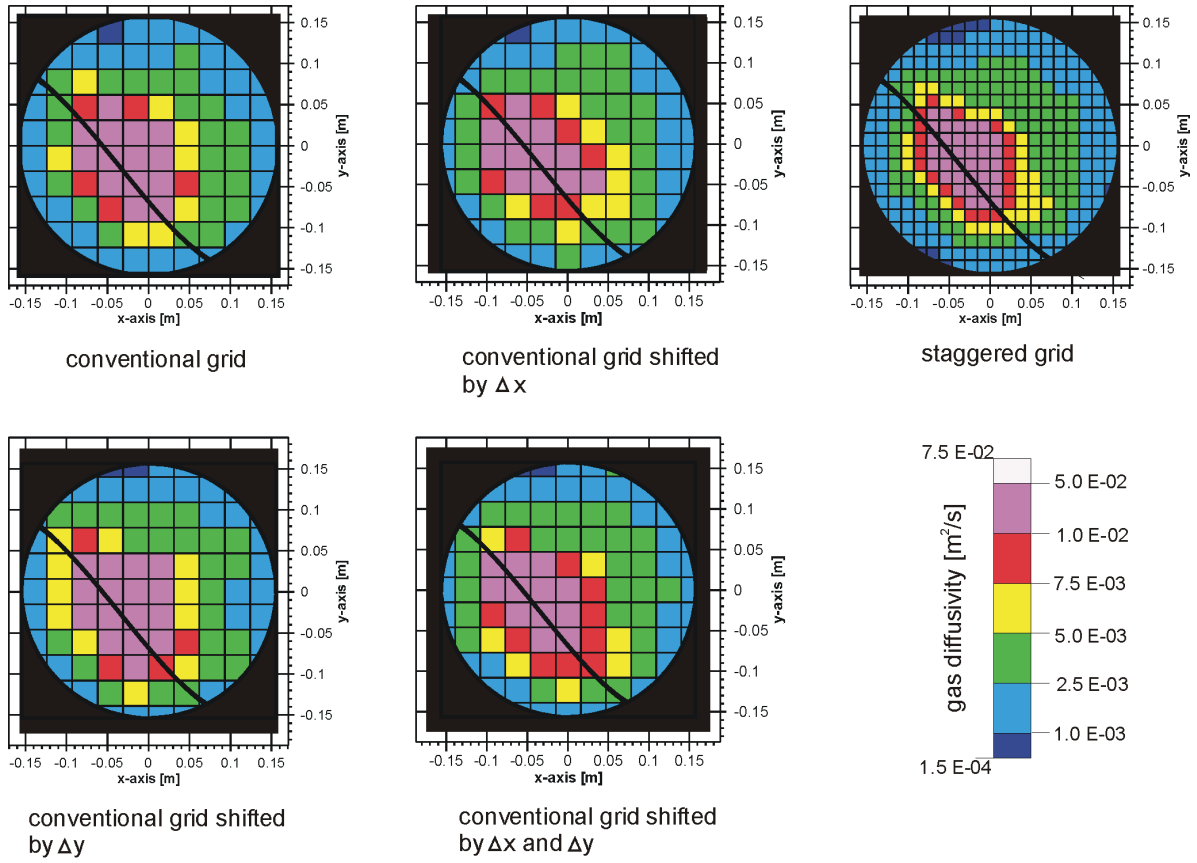

Figure A-1 Inversion results for the travel time associated with 8.2 % of the maximum flow rate. Comparison of the inversion results of a horizontal slice at z = 11.3 cm by using a staggered and four conventional grids [BRAUCHLER ET AL., 2003a]. Color version of Figure 4.11.

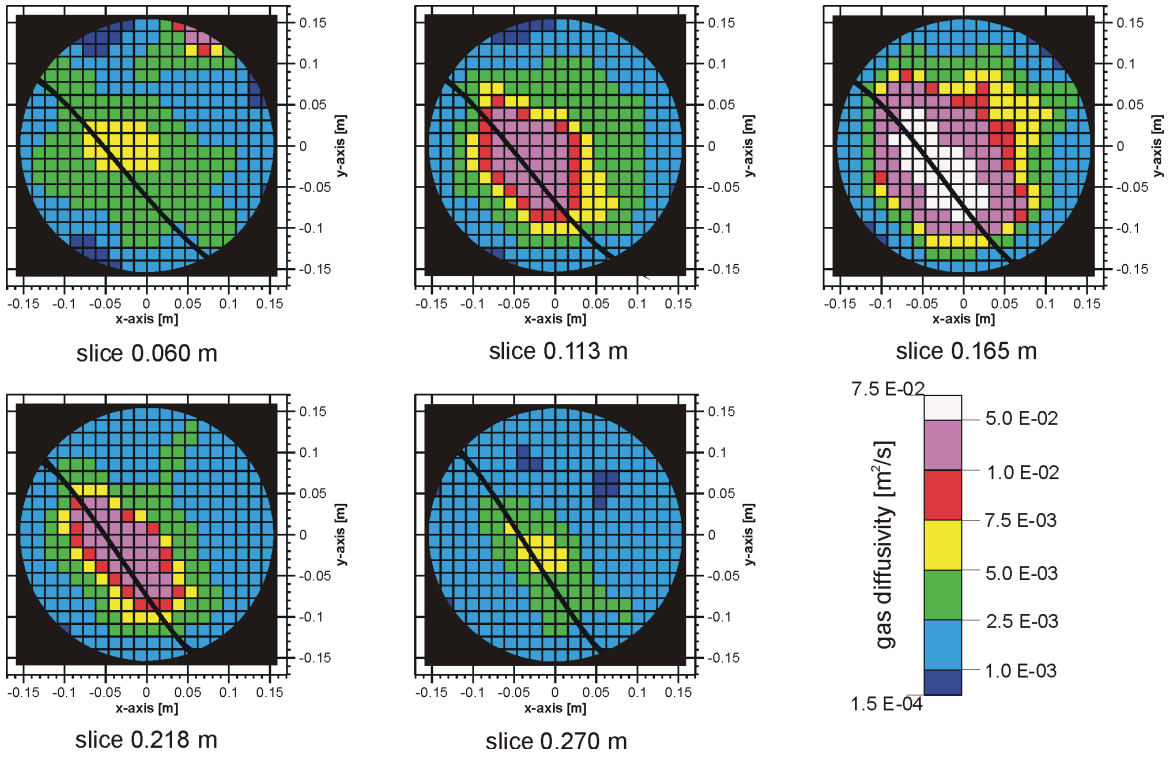

Figure A-2 Inversion results for the travel time associated with 8.2 % of the maximum flow rate, using the method of staggered grids [BRAUCHLER ET AL., 2003,a]. Color version of Figure 4.12.

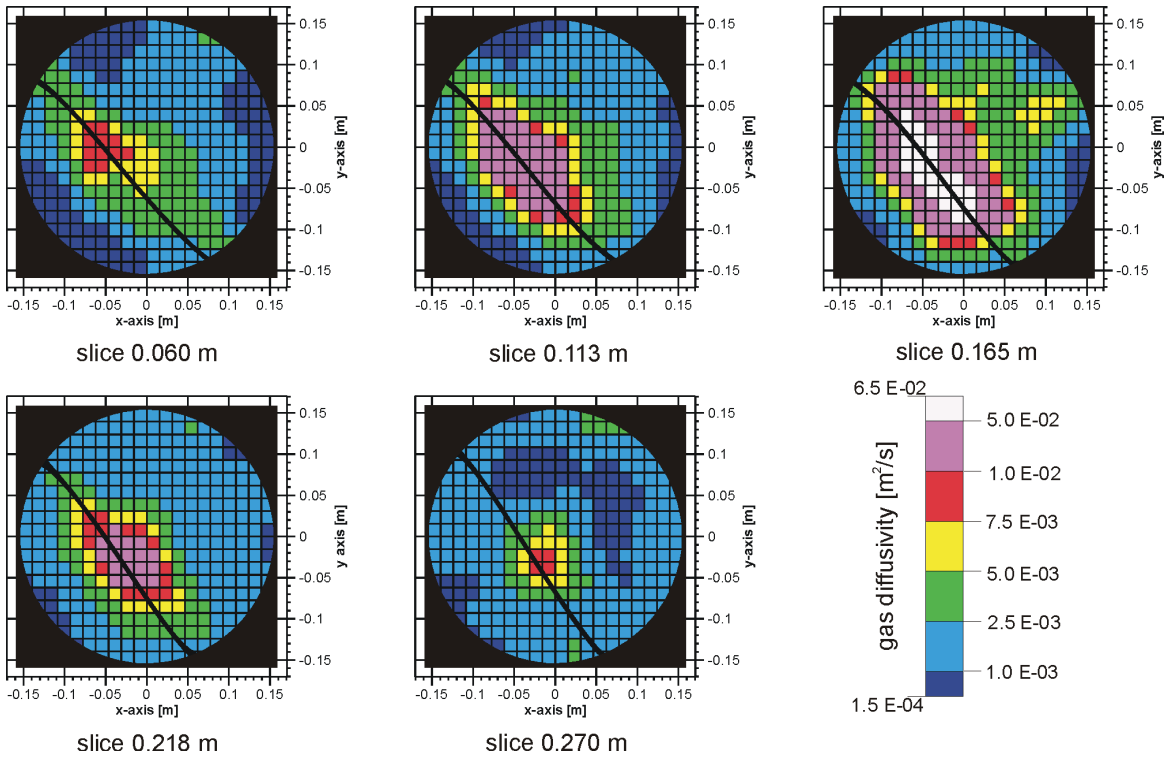

Figure A-3 Inversion results for the travel time associated with 1 % of the maximum flow rate, using the method of staggered grids [BRAUCHLER ET AL., 2003,a]. Color version of Figure 4.13.

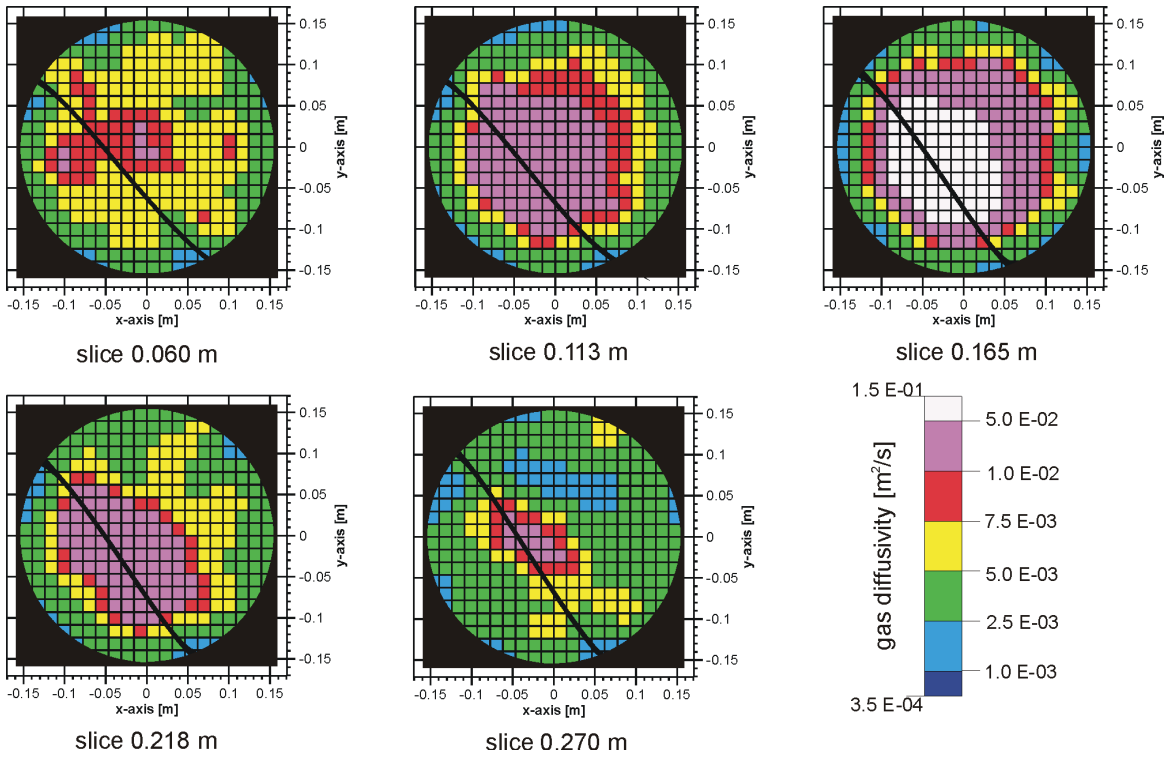

Figure A-4 Inversion results for the travel time associated with 40 % of the maximum flow rate, using the method of staggered grids [BRAUCHLER ET AL., 2003,a]. Color version of Figure 4.14.

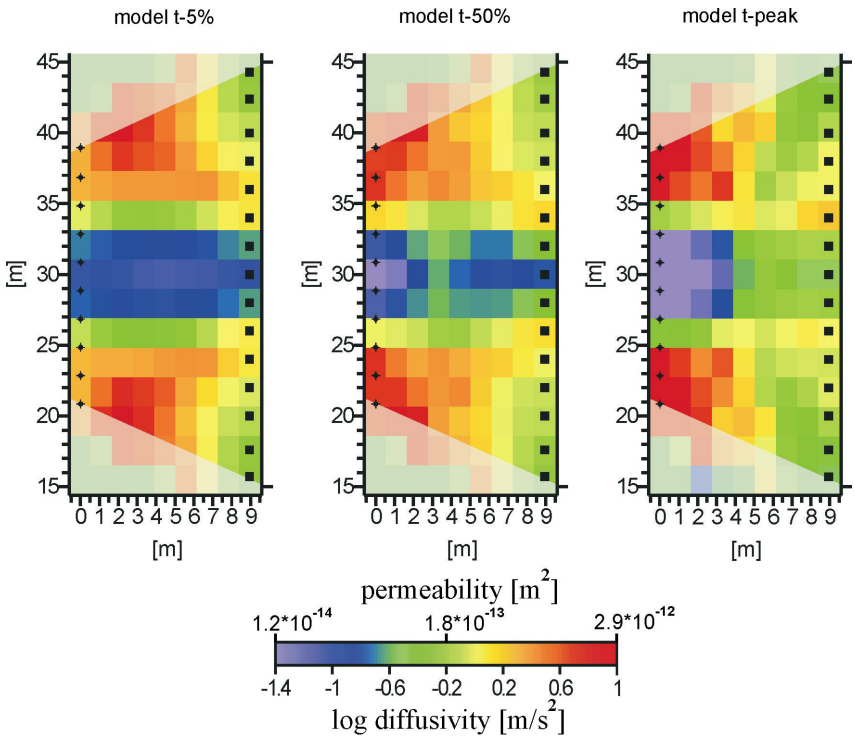

Figure A-5 Inversion results for the travel times associated with 5%, 50% and 100% (peak time) of the maximum pressure change. The data base of the inversion comprises travel times obtained from simulated slug tests. The permeability distribution used for the simulations is illustrated in Figure 5.5a. The specific aquifer storage is constant (Table 5.1). Color version of Figure 5.8.

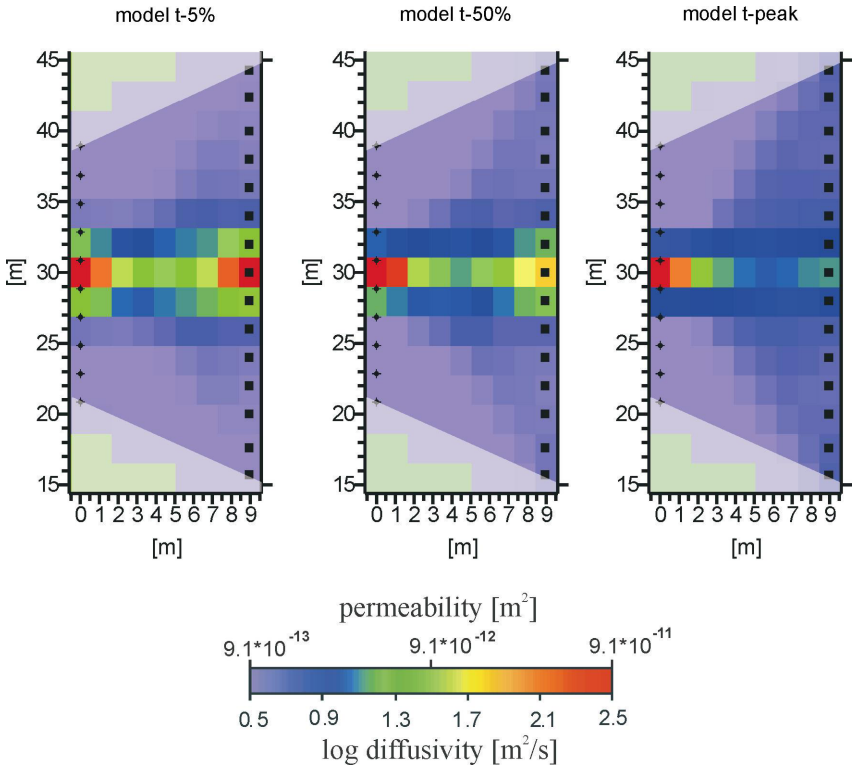

Figure A-6 Inversion results for the travel times associated with 5%, 50%, and 100% (peak time) of the maximum pressure change. The data base of the inversion comprises travel times obtained from simulated slug tests. The used permeability distribution for the simulations is illustrated in Figure 5.5b. The specific aquifer storage is constant (Table 5.1). Color version of Figure 5.14.

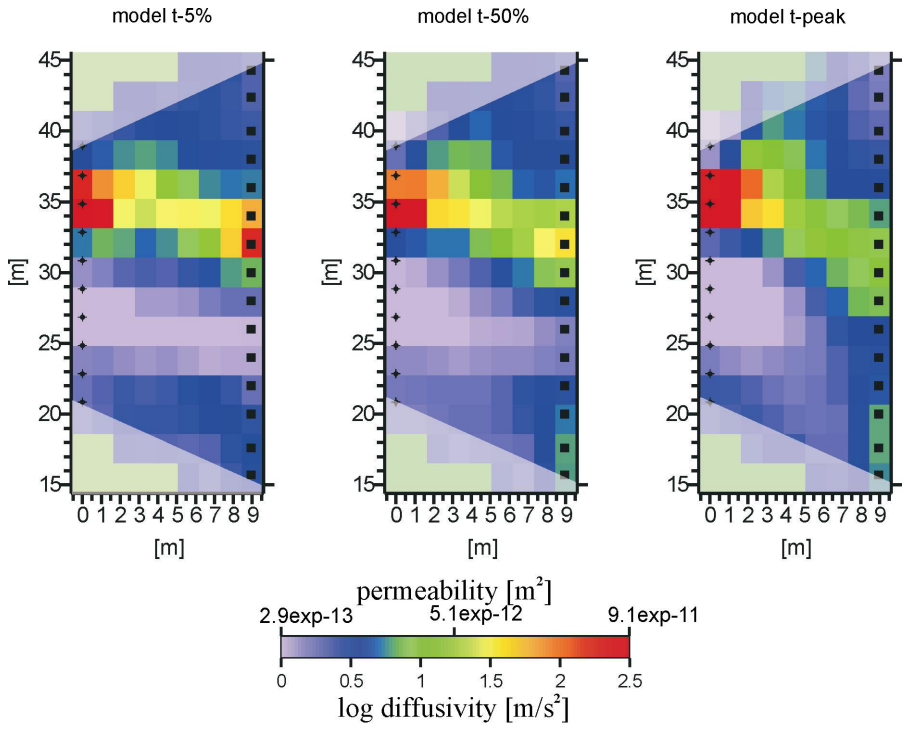

Figure A-7 Inversion results for the travel times associated with 5%, 50%, and 100% (peak time) of the maximum pressure change. The data base of the inversion comprises travel times obtained from simulated slug tests. The used permeability distribution for the simulations is illustrated in Figure 5.5c. The specific aquifer storage is constant (Table 5.1). Color version of Figure 5.20.

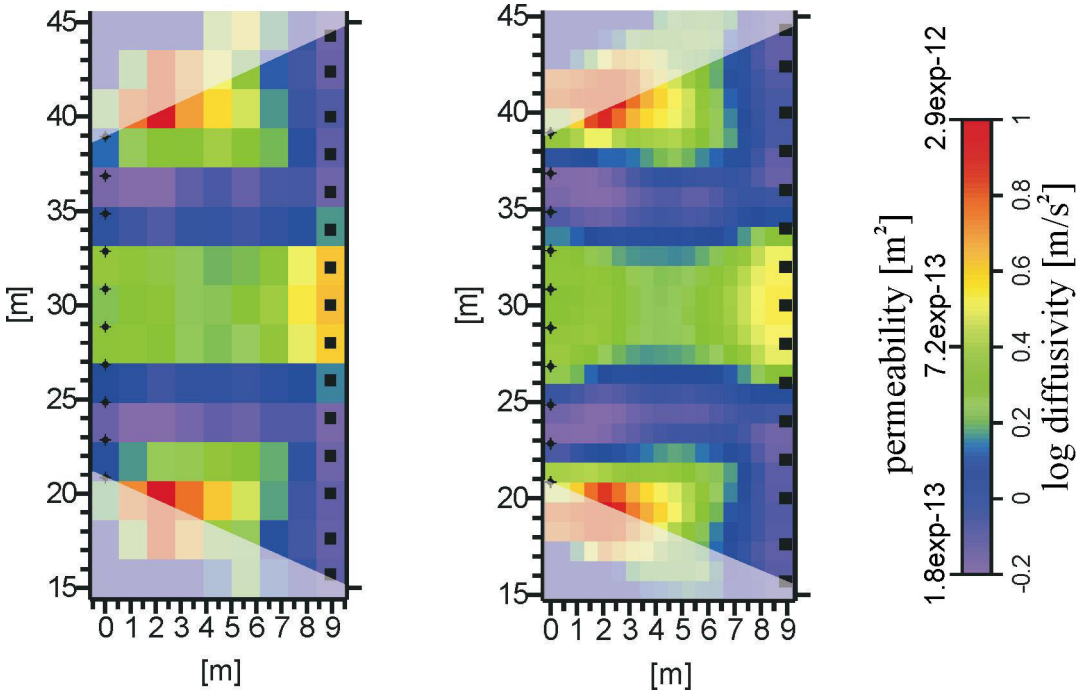

Figure A-8 Inversion results for the travel times associated with 5% of the maximum pressure change. Comparison of the inversion results by using a conventional and a staggered grid. The data base of the inversion comprises travel times obtained from simulated slug tests. The used permeability distribution for the simulations is illustrated in Figure 5.5d. The specific aquifer storage is constant (Table 5.1). Color version of Figure 5.21.

In der Reihe C Hydro-, Ingenieur- und Umweltgeologie der Tübinger Geowissenschaftlichen Arbeiten (TGA) sind bisher erschienen:

Nr. 1: Grathwohl, Peter (1989): Verteilung unpolarer organischer Verbindungen in der wasserungesättigten Bodenzone am Beispiel der leichtflüchtigen aliphatischen Chlorkohlenwasserstoffe. 102 S.

Nr. 2: Eisele, Gerhard (1989): Labor- und Felduntersuchungen zur Ausbreitung und Verteilung leichtflüchtiger chlorierter Kohlenwasserstoffe (LCKW) im Übergangsbereich wasserungesättigte/wassergesättigte Zone. 84 S.

Nr. 3: Ehmann, Michael (1989): Auswirkungen atmogener Stoffeinträge auf Boden- und Grundwässer sowie Stoffbilanzierungen in drei bewaldeten Einzugsgebieten im Oberen Buntsandstein (Nordschwarzwald). 134 S.

Nr. 4: Irouschek, Thomas (1990): Hydrogeologie und Stoffumsatz im Buntsandstein des Nordschwarzwaldes. 144 S.

Nr. 5: Sanns, Matthias (1990): Experimentelle Untersuchungen zum Ausbreitungsverhalten von leichtflüchtigen Chlorkohlenwasserstoffen (LCKW) in der wassergesättigten Zone. 122 S. **(Vergriffen!)**

Nr. 6: Seeger, Thomas (1990): Abfluß- und Stofffrachtseparation im Buntsandstein des Nordschwarzwaldes. 154 S.

Nr. 7: Einsele, Gerhard & Pfeffer, Karl-Heinz (Hrsg.) (1990): Untersuchungen über die Auswirkungen des Reaktorunfalls von Tschernobyl auf Böden, Klärschlamm und Sickerwasser im Raum von Oberschwaben und Tübingen. 151 S.

Nr. 8: Douveas, Nikon G. (1990): Verwitterungstiefe und Untergrundabdichtung beim Talsperrenbau in dem verkarsteten Nord-Pindos-Flysch (Projekt Pigai-Aoos, NW-Griechenland). 165 S.

Nr. 9: Schlöser, Heike (1991): Quantifizierung der Silikatverwitterung in karbonatfreien Deckschichten des Mittleren Buntsandsteins im Nordschwarzwald. 93 S.

Nr. 10: Köhler, Wulf-Rainer (1992): Beschaffenheit ausgewählter, nicht direkt anthropogen beeinflußter oberflächennaher und tiefer Grundwasservorkommen in Baden-Württemberg. 144 S.

Nr. 11: Bundschuh, Jochen (1991): Der Aquifer als thermodynamisch offenes System. – Untersuchungen zum Wärmetransport in oberflächennahen Grundwasserleitern unter besonderer Berücksichtigung von Quellwassertemperaturen (Modellversuche und Geländebeispiele). 100 S. **(Vergriffen!)**

Nr. 12: Herbert, Mike (1992): Sorptions- und Desorptionsverhalten von ausgewählten polyzyklischen aromatischen Kohlenwasserstoffen (PAK) im Grundwasserbereich. 111 S.

Nr. 13: Sauter, Martin (1993): Quantification and forecasting of regional groundwater flow and transport in a karst aquifer (Gallusquelle, Malm, SW-Germany. 150 S.

Nr. 14: Bauer, Michael (1993): Wasserhaushalt, aktueller und holozäner Lösungsabtrag im Wutachgebiet (Südschwarzwald). 130 S.

Nr. 15: Einsele, Gerhard & Ricken, Werner (Hrsg.) (1993): Eintiefungsgeschichte und Stoffaustrag im Wutachgebiet (SW-Deutschland). 215 S.

Nr. 16: Jordan, Ulrich (1993): Die holozänen Massenverlagerungen des Wutachgebietes (Südschwarzwald). 132 S. **(Vergriffen!)**

Nr. 17: Krejci, Dieter (1994): Grundwasserchemismus im Umfeld der Sonderabfalldeponie Billigheim und Strategie zur Erkennung eines Deponiesickerwassereinflusses. 121 S.

Nr. 18: Hekel, Uwe (1994): Hydrogeologische Erkundung toniger Festgesteine am Beispiel des Opalinustons (Unteres Aalenium). 170 S. **(Vergriffen!)**

Nr. 19: Schüth, Christoph (1994): Sorptionskinetik und Transportverhalten von polyzyklischen aromatischen Kohlenwasserstoffen (PAK) im Grundwasser - Laborversuche. 80 S.

Nr. 20: Schlöser, Helmut (1994): Lösungsgleichgewichte im Mineralwasser des überdeckten Muschelkalks in Mittel-Württemberg. 76 S.

Nr. 21: Pyka, Wilhelm (1994): Freisetzung von Teerinhaltsstoffen aus residualer Teerphase in das Grundwasser: Laboruntersuchungen zur Lösungsrate und Lösungsvermittlung. 76 S.

Nr. 22: Biehler, Daniel (1995): Kluftgrundwässer im kristallinen Grundgebirge des Schwarzwaldes – Ergebnisse von Untersuchungen in Stollen. 103 S.

Nr. 23: Schmid, Thomas (1995): Wasserhaushalt und Stoffumsatz in Grünlandgebieten im württembergischen Allgäu. 145+ 92 S.

Nr. 24: Kretzschmar, Thomas (1995): Hydrochemische, petrographische und thermodynamische Untersuchungen zur Genese tiefer Buntsandsteinwässer in Baden-Württemberg. 142 S. **(Vergriffen!)**

Nr. 25: Hebestreit, Christoph (1995): Zur jungpleistozänen und holozänen Entwicklung der Wutach (SW-Deutschland). 88 S.

Nr. 26: Hinderer, Matthias (1995): Simulation langfristiger Trends der Boden- und Grundwasserversauerung im Buntsandstein-Schwarzwald auf der Grundlage langjähriger Stoffbilanzen. 175 S.

Nr. 27: Körner, Johannes (1996): Abflußbildung, Interflow und Stoffbilanz im Schönbuch Waldgebiet. 206 S.

Nr. 28: Gewald, Thomas (1996): Der Einfluß der Desorptionskinetik bei der Freisetzung von Trichlorethen (TCE) aus verschiedenen Aquifersanden. 67 S.

Nr. 29: Schanz, Ulrich (1996): Geophysikalische Untersuchungen im Nahbereich eines Karstsystems (westliche Schwäbische Alb). 114 S.

Nr. 30: Renner, Sven (1996): Wärmetransport in Einzelklüften und Kluftaquiferen – Untersuchungen und Modellrechnungen am Beispiel eines Karstaquifers. 89 S.

Nr. 31: Mohrlok, Ulf (1996): Parameter-Identifikation in Doppel-Kontinuum-Modellen am Beispiel von Karstaquiferen. 125 S.

Nr. 32: Merkel, Peter (1996): Desorption and Release of Polycyclic Aromatic Hydrocarbons (PAHs) from Contaminated Aquifer Materials. 76 S.

Nr. 33: Schiedek, Thomas (1996): Auftreten und Verhalten von ausgewählten Phthalaten in Wasser und Boden. 112 S.

Nr. 34: Herbert, Mike & Teutsch, Georg (Hrsg.) (1997): Aquifersysteme Südwestdeutschlands - Eine Vorlesungsreihe an der Eberhard-Karls-Universität Tübingen. 162 S.

Nr. 35: Schad, Hermann (1997): Variability of Hydraulic Parameters in Non-Uniform Porous Media: Experiments and Stochastic Modelling at Different Scales. 233 S.

Nr. 36: Herbert, Mike & Kovar, Karel (Eds.) (1998): GROUNDWATER QUALITY 1998: Remediation and Protection - Posters -.- Proceedings of the GQ'98 conference, Tübingen, Sept. 21-25, 1998, Poster Papers. 146 S.

Nr. 37: Klein, Rainer (1998): Mechanische Bodenbearbeitungsverfahren zur Verbesserung der Sanierungseffizienz bei In-situ-Maßnahmen. 106 S.

Nr. 38: Schollenberger, Uli (1998): Beschaffenheit und Dynamik des Kiesgrundwassers im Neckartal bei Tübingen. 74 S.

Nr. 39: Rügner, Hermann (1998): Einfluß der Aquiferlithologie des Neckartals auf die Sorption und Sorptionskinetik organischer Schadstoffe. 78 S.

Nr. 40: Fechner, Thomas (1998): Seismische Tomographie zur Beschreibung heterogener Grundwasserleiter. 113 S.

Nr. 41: Kleineidam, Sybille (1998): Der Einfluß von Sedimentologie und Sedimentpetrographie auf den Transport gelöster organischer Schadstoffe im Grundwasser. 82 S.

Nr. 42: Hückinghaus, Dirk (1998): Simulation der Aquifergenese und des Wärmetransports in Karstaquiferen. 124 S.

Nr. 43: Klingbeil, Ralf (1998): Outcrop Analogue Studies – Implications for Groundwater Flow and Contaminant Transport in Heterogeneous Glaciofluvial Quaternary Deposits. 111 S.

Nr. 44: Loyek, Diana (1998): Die Löslichkeit und Lösungskinetik von polyzyklischen aromatischen Kohlenwasserstoffen (PAK) aus der Teerphase. 81 S.

Nr. 45: Weiß, Hansjörg (1998): Säulenversuche zur Gefahrenbeurteilung für das Grundwasser an PAK-kontaminierten Standorten. 111 S.

Nr. 46: Jianping Yan (1998): Numerical Modeling of Topographically-closed Lakes: Impact of Climate on Lake Level, Hydrochemistry and Chemical Sedimentation. 144 S.

Nr. 47: Finkel, Michael (1999): Quantitative Beschreibung des Transports von polyzyklischen aromatischen Kohlenwasserstoffen (PAK) und Tensiden in porösen Medien. 98 S.

Nr. 48: Jaritz, Renate (1999): Quantifizierung der Heterogenität einer Sandsteinmatrix (Mittlerer Keuper, Württemberg). 106 S.

Nr. 49: Danzer, Jörg (1999): Surfactant Transport and Coupled Transport of Polycyclic Aromatic Hydrocarbons (PAHs) and Surfactants in Natural Aquifer Material - Laboratory Experiments. 75 S.

Nr. 50: Dietrich, Peter (1999): Konzeption und Auswertung gleichstromgeoelektrischer Tracerversuche unter Verwendung von Sensitivitätskoeffizienten. 130 S.

Nr. 51: Baraka-Lokmane, Salima (1999): Determination of Hydraulic Conductivities from Discrete Geometrical Characterisation of Fractured Sandstone Cores. 119 S.

Nr. 52: M^{c}Dermott, Christopher I. (1999): New Experimental and Modelling Techniques to Investigate the Fractured System. 170 S.

Nr. 53: Zamfirescu, Daniela (2000): Release and Fate of Specific Organic Contaminants at a Former Gasworks Site. 96 S.

Nr. 54: Herfort, Martin (2000): Reactive Transport of Organic Compounds Within a Heterogeneous Porous Aquifer. 76 S.

Nr. 55: Klenk, Ingo (2000): Transport of Volatile Organic Compounds (VOC's) From Soilgas to Groundwater. 70 S.

Nr. 56: Martin, Holger (2000): Entwicklung von Passivsammlern zum zeitlich integrierenden Depositions- und Grundwassermonitoring: Adsorberkartuschen und Keramikdosimeter. 84 S.

Nr. 57: Diallo, Mamadou Sanou (2000): Acoustic Waves Attenuation and Velocity Dispersion in Fluid-Filled Porous Media: Theoretical and Experimental Investigations. 101 S.

Nr. 58: Lörcher, Gerhard (2000): Verarbeitung und Auswertung hyperspektraler Fernerkundungsdaten für die Charakterisierung hydrothermaler Systeme (Goldfield/Cuprite, Yellowstone National Park). 158 S.

Nr. 59: Heinz, Jürgen (2001): Sedimentary Geology of Glacial and Periglacial Gravel Bodies (SW-Germany): Dynamic Stratigraphy and Aquifer Sedimentology. 102 S.

Nr. 60: Birk, Steffen (2002): Characterisation of Karst Systems by Simulating Aquifer Genesis and Spring Responses: Model Development and Application to Gypsum Karst. 122 S.

Nr. 61: Halm, Dietrich & Grathwohl, Peter (Eds.) (2002): Proceedings of the 1st International Workshop on Groundwater Risk Assessment at Contaminated Sites (GRACOS). 280 S.

Nr. 62: Bauer, Sebastian (2002): Simulation of the genesis of karst aquifers in carbonate rocks. 143 S.

Nr. 63: Rahman, Mokhlesur (2002): Sorption and Transport Behaviour of Hydrophobic Organic Compounds in Soils and Sediments of Bangladesh and their Impact on Groundwater Pollution – Laboratory Investigations and Model Simulations. 73 S.

Nr. 64: Peter, Anita (2002): Assessing natural attenuation at field scale by stochastic reactive transport modelling. 101 S.

Nr. 65: Leven-Pfister, Carsten (2002): Effects of Heterogeneous Parameter Distributions on Hydraulic Tests - Analysis and Assessment. 94 S.

Nr. 66: Schwarz, Rainer (2002): Grundwasser-Gefährdungsabschätzungen durch Emissions- und Immissionsmessungen an Deponien und Altlasten. 100 S.

Nr. 67: Abel, Thekla (2003): Untersuchungen zur Genese des Malmkarsts der Mittleren Schwäbischen Alb im Quartär und jüngeren Tertiär. 187 S.

Nr. 68: Prokop, Gundula & Bittens, Martin & Cofalka, Piotr & Roehl, Karl Ernst & Schamann, Martin & Younger, Paul (Eds.) (2003): Summary Report on the 1st IMAGE-TRAIN Advanced Study Course “Innovative Groundwater Management Technologies”. 119 S.

Nr. 69: Halm, Dietrich & Grathwohl, Peter (Eds.) (2003): Proceedings of the 2nd International Workshop on Groundwater Risk Assessment at Contaminated Sites (GRACOS) and Integrated Soil and Water Protection (SOWA). 260 S.

Nr. 70: Bayer, Peter (2004): Modelling, economic assessment and optimisation of in-situ groundwater remediation systems. 78 S.

Nr. 71: Kraft, Siegfried (2004): Untersuchungen zum Langzeiteinsatz der in-situ Aktivkohlefiltration zur Entfernung von organischen Schadstoffen aus Grundwasser. 64 S.

Nr. 72: Bold, Steffen (2004): Process-based prediction of the long-term risk of groundwater pollution by organic non-volatile contaminants. 76 S.

Nr. 73: Maier, Ulrich (2004): Modelling of Natural Attenuation in Soil and Groundwater. 81 S.

Nr. 74: Susset, Bernd (2004): Materialuntersuchungen und Modellierungen zur Unterscheidung Gleichgewicht / Ungleichgewicht in Säulenversuchen für die Sickerwasserprognose organischer Schadstoffe. 100 S.

Nr. 75: Madlener, Iris (2004): Quantifizierung und Modellierung des PAK-Desorptionsverhaltens aus feinkörnigem Material mittels Säulenversuchen (DIN V 19736) und Hochdruck-Temperatur-Elution (ASE).

Nr. 76: Henzler, Rainer (2004): Quantifizierung und Modellierung der PAK-Elution aus verfestigten und unverfestigten Abfallmaterialien.

Nr. 77: Valley, Stephan (2004): Natural Attenuation of Volatile Organic Compounds (VOC) in Groundwater: A Method for the Determination of Compound-Specific Stable Carbon Isotope Ratios at Low Concentration Levels. 67 S.

Nr. 78: Röttgen, Klaus Peter (2004): Kritische Analyse des Aufwandes zur Erkundung von Kontaminationen in niedersächsischen Grundwassergeringleitern.

Nr. 79: Gocht, Tilman (2005): Die vier Griechischen Elemente: Massenbilanzierung von polyzyklischen aromatischen Kohlenwasserstoffen (PAK) in Kleineinzugsgebieten des ländlichen Raumes. **– Im Druck.**

Nr. 80: Halm, Dietrich & Grathwohl, Peter (Eds.) (2004): Proceedings of the 2nd International Workshop on Integrated Soil and Water Protection (SOWA). 161 S.

Nr. 81: Prokop, Gundula, Bittens, Martin, Moraczewska-Maikut, Katarzyna, Roehl, Karl Ernst, Schamann, Martin & Younger, Paul (Eds.) (2004): Summary Report on the 3rd IMAGE-TRAIN Advanced Study Course "Quantitative Risk Assessment". 66 S.

Nr. 82: Hoffmann, Ruth (2004): Optimierungsansätze zur Datenerfassung und Interpretation von Multielektrodenmessungen.

Nr. 83: Kostic, Boris (2004): 3D sedimentary architecture of Quaternary gravel bodies (SW-Germany): implications for hydrogeology and raw materials geology. 103 S.

Nr. 84: Bayer-Raich, Marti (2004): Integral pumping tests for the characterization of groundwater contamination. 112 S.

Nr. 85: Piepenbrink, Matthias (2005): **– Im Druck.**

Nr. 86: Becht, Andreas (2004): Geophysical methods for the characterization of gravel aquifers: case studies and evaluation experiments.

Nr. 87:Brauchler, Ralf (2005): Characterization of Fractured Porous Media Using Multivariate Statistics and Hydraulic Travel Time Tomography. 72 S.

Nr. 88: Stefan Gödeke (2004): Evaluierung und Modellierung des Natural Attenuation Potentials am Industriestandort Zeitz. 139 S.